# Probing the Higgs sector at the FCC-ee

Author:

**Nico Härringer**

Laboratoire Leprince-Ringuet (LLR), Palaiseau, FR

Supervisor:

**Roberto Salerno**

Laboratoire Leprince-Ringuet (LLR), Palaiseau, FR

A thesis submitted in fulfillment of the requirements for the degree of
Master of Science in Physics ETH Zurich – Institut Polytechnique de Paris
Major in High Energy Physics

**Date of defense:** 22 July 2022

CERN-THESIS-2022-143
22/07/2022

*Probing the Higgs sector at the FCC-ee*

Author:
Nico Härringer (Laboratoire Leprince-Ringuet (LLR), Palaiseau, FR)

Supervisor:
Roberto Salerno (Laboratoire Leprince-Ringuet (LLR), Palaiseau, FR)

# Abstract

This thesis examined three observables relevant to the Standard Model Higgs sector, which are the Higgs boson mass, its production cross section and the trilinear self-coupling, and estimated the performance of the measurement of these parameters at the FCC-ee. Compared to the previous analysis we introduced more Higgs boson production channels at $\sqrt{s} = 240, 365$ GeV, used improved Monte Carlo samples (including initial and final state radiation) and a new orthogonal categorization of events. The Higgs boson mass was constrained to be within 5.6 MeV around the nominal value of 125 GeV at 68% CL using inclusive leptonic Higgsstrahlung channels at both energies. We used inclusive Higgsstrahlung (leptonic and hadronic) and exclusive vector boson fusion channels in a combined analysis to extract the sensitivity on the respective cross sections as well as on the trilinear self-coupling. The signal strength modifiers used to estimate the precision on the Higgsstrahlung and vector boson fusion production cross sections were measured with sub-percent and percent precision under the assumption that the decay of the Higgs boson follows the Standard Model expectation. In a similar manner, we extracted the Higgs boson trilinear self-coupling $\kappa_\lambda$ using one-loop corrections of the leading order Feynman diagrams of Higgsstrahlung and vector boson fusion. Assuming all parameters but $\kappa_\lambda$ are set to the Standard Model expectation, $\delta\kappa_\lambda$ can be constraint within $[-0.29, 0.31]$ at 68% CL. This precision reach is compromised once multiple parameters of interest are left floating in the fit.

# Acknowledgements

I would like to thank Roberto Salerno for the supervision of this thesis. In the brief time in his group I learned a lot about doing research in high energy physics. Roberto sparked an interest in doing precision Higgs boson physics and introduced me in the world of $e^+e^-$ machines. I am grateful that I could do my M2 internship here at LLR. I also want to thank Alessandra Cappati and Elena Vernazza for being such great office colleagues. Thank you, Alessandra, for all your help and nice discussions especially when it comes to ROOT or C++. I learned a lot from that. A special thanks goes to Roy Lemmon and Swathi Sasikumar for very useful discussions and their feedback during the internship and the thesis writing. I thank the whole CMS group at LLR for the pleasant and very welcoming environment! I really enjoyed spending time with all of you also outside the office and wish you all the best! Finally, I also want to thank my family and my girlfriend for supporting me throughout my time in Paris.

Last but not least, I want to say thank you to all the lecturers and professors from the ETH Zurich - IP Paris High Energy Physics Joint Master for offering this unique program. Over the last two years I met a lot of new people from different backgrounds and countries and also the final year in Paris had been a very enriching experience.

# Contents

# 1 Introduction

The discovery of the Higgs boson in 2012 by the LHC at CERN [1, 2] was a key point in understanding how electroweak symmetry breaking (EWSB) occurs in the Standard Model (SM) [3]. From the current measurements [4] it became apparent that the SM describes nature very well.

However, there are indications that the SM is not the final theory and it could rather be embedded in a more general one. Not only does the SM fail to include gravity, there is also no fundamental reason for charge quantization [5]. Starting from the gauge group of the SM $SU(3)_c \times SU(2)_L \times U(1)_Y$, unquantized charges could in principle be found by adding a right-handed neutrino $\nu_R$ to the theory [6]. When we interpret the $U(1)_Y$ group as the subgroup of a non-abelian group, charge quantization emerges naturally after a respective symmetry breaking of the unknown non-abelian group.

Another important aspect is the validity of the Higgs sector. Many beyond the SM (BSM) theories introduce more Higgs particles [7, 8] in order to break their higher symmetries down to the SM. The effects of these higher symmetries are inherited by the SM, in particular various couplings get modified as well due to the larger Higgs sector. This circumstance can be described using an effective field theory (EFT) parametrization [9, 10] if the energy scale which is considered is much lower than the higher symmetry breaking scale. Thus, understanding the structure and possible deviations of the Higgs sector is important when the SM is to be tested to its limits.

Searches of this kind often involve ratios of the measured observables versus their predicted (SM) values. For example, BSM searches [11, 12] are commonly conducted by means of using ratios. One advantage of this method is the cancellation of most systematic errors, while another advantage is, that if considering a well known denominator (e.g. using a precision calculation of a cross section $\sigma_{\text{SM}}$), the deviation from the expected value can be measured very accurately. Depending on the nature of the observable, some environments are better suited than others. Concerning the trilinear Higgs boson self-coupling constant, it is best measured using clean electroweak processes with low pileup, since otherwise the large background coming from underlying events would degrade the precision of the measurement.

High sensitivity on the trilinear self-coupling can be reached using various approaches. For example, the next major upgrade of the LHC - the High Luminosity LHC (HL-LHC) - is expected to collect an integrated luminosity of up to 4'000 $\text{fb}^{-1}$ [13]. Not only will it increase the number of observed events, but also the sensitivity of the extracted self-coupling parameter [14]. Since the HL-LHC is a proton-proton (pp) collider, it suffers from a poorly defined initial state and considerable pileup, decreasing the expected sensitivity on the trilinear self-coupling. The protons utilized in the collisions are mixtures of quarks and gluons. This requires a precise knowledge of the underlying parton density functions (PDF). While the PDFs have been measured to a great extend using the LHC [15, 16], they still introduce large uncertainties which is reflected in the precision of the measurement at HL-LHC. Many of the aforementioned problems are of little concern for electron-positron colliders as they are using fundamental particles. The next chapter introduces the planned successor of the LHC, the Future Circular Collider.

## 1.1 Future Circular Collider

The LHC was inaugurated in 2008 and is planned to run until 2038 with the HL-LHC taking data starting in 2026. In 2020, the European Strategy for Particle Physics announced that the LHC successor is going to be a electron-positron collider similar to LEP [17]. The main difference between LEP and the Future Circular Collider (FCC) is the diameter of the ring (27 km (LEP) and 91 km (FCC)) which allows for higher collision energies [18, 19] than LEP. In its first phase which is projected to run between 2045 and 2060, the FCC is planned to be an electron-positron collider which in terms of center of mass energy focuses mainly on the Z pole around 91 GeV (four years), the WW production threshold at 160 GeV (two years), the Higgsstrahlung (ZH) production threshold at 240 GeV (three years) and finally the $tt$ production threshold at 365 GeV (five years). The termination of the FCC-ee is scheduled in the 2060s after which it will be retrofitted preferably into a hadron-hadron machine (FCC-hh). The FCC-hh is planned to run from 2070 onwards and will collide protons with $\sqrt{s}$ of up to 100 TeV [20].

In this work, two of the planned energy points of the FCC-ee are considered. The first energy point will be the ZH production threshold $\sqrt{s} = 240$ GeV. Current studies [19] expect an integrated luminosity of $\mathscr{L} = 5\ \text{ab}^{-1}$. The second energy point is the $tt$ production threshold with an expected integrated luminosity of $\mathscr{L} = 1.5\ \text{ab}^{-1}$. Over the course of the runtime of the FCC-ee from the two energy points $1.2 \times 10^6$ ZH and $7.5 \times 10^4$ WW-Fusion events are expected.

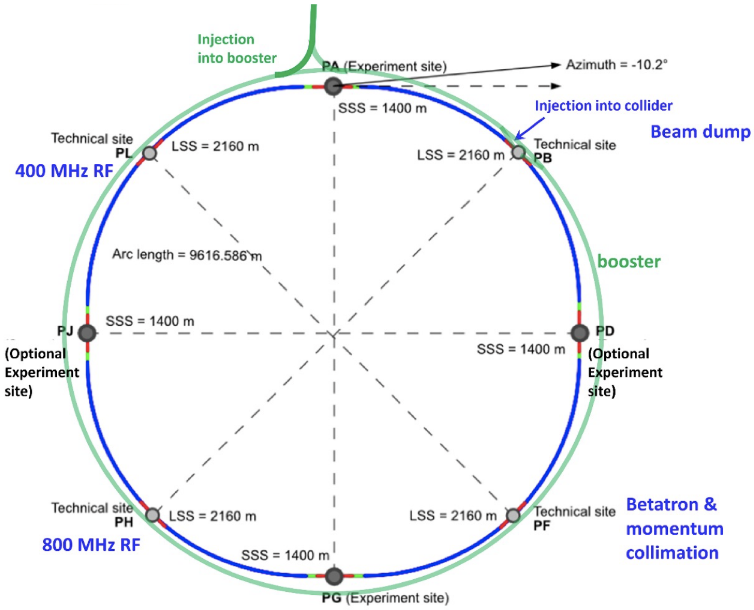


Figure 1: An overview of the FCC-ee and its projected interaction points (IP). [21]

Currently there are two different baselines for the layout of the FCC-ee under consideration [21]. The four IP baseline (see Fig. 1) features additional systematic robustness, a broader choice of detector technologies and a higher integrated luminosity per year compared to the two IP baseline option ($\mathscr{L} = 10.5\ \text{ab}^{-1}$ for the ZH threshold and $\mathscr{L} = 1.95\ \text{ab}^{-1}$ for the $tt$ threshold for the same runtime [21, 22]). The downside are the increased costs for civil engineering and developement. In this study, we assume the two IP baseline option and the integrated luminosities mentioned above are given as the sum of the collected luminosities per IP.

### Why lepton colliders?

One advantage of using a lepton collider is that the initial state is precisely known, which makes the collision very clean. Since at lepton colliders elementary particles are used in the collision, there are no PDFs involved and thus the collisions $\sqrt{s}$ is not severely different from the nominal $\sqrt{s}$.

The main degrading elements are effects of initial state radiation (ISR) and beam-beam effects (such as beamstrahlung) which decrease $\sqrt{s}$ and in case of beamstrahlung also the luminosity [23]. Furthermore, due to the synchrotron radiation and power limitations of the RF cavities, the luminosity is reduced very rapidly when $\sqrt{s}$ is increased.

**Innovative Detector for $e^+e^-$ Accelerators (IDEA) detector**

The Innovative Detector for $e^+e^-$ Accelerators (IDEA) detector [19] is one of the planned detector concepts for the FCC-ee (see Fig. 3). It is specifically designed to operate efficiently in the clean collision environment. To fully exploit the high statistics projected at the FCC, it has to feature precision tracking and a very good and reliable reconstruction of leptons and hadrons using a high granularity calorimeter. To safely extract the flavor of the produced jets, also a very precise vertex detector must be implemented as well. A considerable challenge is the environment the detector is facing. At FCC-ee very high luminosities are expected and preferably every event wants to be extracted. A limiting factor for this undertaking are the rates, the data acquisition systems (DAQ) are able to process. Another key issue is the radiation the very sensitive equipment is exposed to. For these reasons, the IDEA concept requires the fastest and radiation-hard DAQ systems.

**IDEA Vertex detector** A silicon vertex detector based on monolithic active pixel sensors (MAPS) [24] is foreseen for the IDEA vertex detector. This technology offers very fast and thin sensors with minimal multiple scattering and without the need of a separate readout chip, as it is integrated in the sensor itself. In total five highly efficient MAPS layers are planned to encompass the IP that feature a point resolution of approximately 3 $\mu$m. This offers precision determination of particle vertices with minimal mass in this part of the detector.

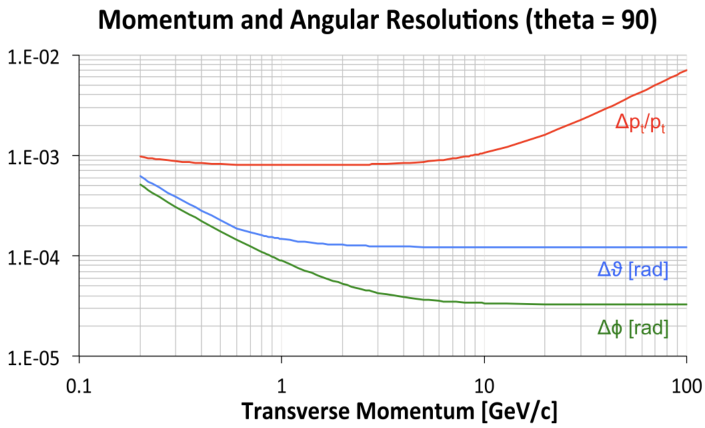


Figure 2: The momentum and angular resolutions for $\theta = 90°$ of the proposed drift chamber for IDEA. [19]

**Drift chamber** Since the tracks at FCC-ee have a lower transverse momentum ($p_T \leq 50$ GeV) than for example at the LHC, a very transparent tracker is required. Consequently, drift chambers are considered as trackers for the IDEA detector. That also offers a multitude of advantages such as continuous tracking which can be useful for many long-lived particle (LLP) searches. Another advantage is the excellent particle separation either via cluster counting or $dE/dx$ measurements. The chamber itself contains an extremely light gas (90% He - 10% isobutane) and tungsten wires [19] which are used to track charged particles. The total amount of material in the central part of the barrel is 1.6% of the radiation length $X_0$, most of which coming from the wires. The performance of the drift chamber in its baseline configuration is shown in Fig. 2.

**Dual-readout calorimeter** Implementing a dual-readout calorimeter makes measurements of the electromagnetic fraction of a particle shower possible on an event-by-event basis. This is achieved by measuring the hadronic and electromagnetic contribution simultaneously with Cherenkov and scintillating fibers. From that, the energy can be calculated very precisely ($\sigma_{em}/E = 13.0\%/\sqrt{E} + 0.2\%$ and $\sigma_{had}/E = 31.0\%/\sqrt{E} + 0.4\%$ extracted from simulations [19]). This high jet energy resolution is necessary to efficiently separate W and Z in a multijet environment.

**Solenoid** The baseline configuration of the IDEA detector features a 2 T superconducting solenoid coil. It has been specifically designed to be as light as possible to decrease the impact on a particles energy and it is located between the proposed tracker and the calorimeter.

**Preshower detector and muon stations** A preshower detector is planned between the solenoid coil and the calorimeter section to increase the performance of the cluster reconstruction. The muon stations are covering most parts of the magnet return yoke and are used to identify muons. Their use case can be extended to LLP searches as well. Both the preshower detector and the muon stations are based on micro-Resistive WELL technology [25].

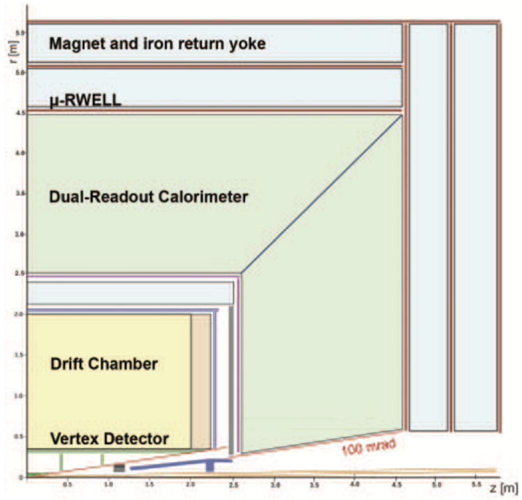


Figure 3: One quadrant of the proposed IDEA detector for FCC-ee. The detector is 11 m high and 13 m long. [26]

### Delphes simulation

The IDEA detector is implemented in a Delphes fast-simulation [27] in which the various components (Tracker, Calorimeter, Muon Chambers) of the detector are modelled with cylindrical shapes. The physical response of particles traversing the cylinders are then calculated based on the requirements of the detector [19, 26]. Finally, Delphes simulates the reconstruction of the particles taking into account the correct reconstruction efficiency based on said specifications.

## 1.2 Higgs boson physics at FCC-ee

One key pillar of the physics programme at the FCC-ee is the study of the Higgs boson. There are many possible Higgs boson studies [18] which can be conducted using the FCC. However, in this thesis we will focus in particular on the Higgs boson mass, the Higgs boson production cross section and on the Higgs boson self-coupling $\lambda_3$. The latter two are modified in the presence of new physics (NP) and the self-coupling can be accessed indirectly at the FCC-ee in both ZH and vector boson fusion (VBF) processes. VBF consists of $W$ boson fusion $e^+e^- \rightarrow \nu_e\bar{\nu}_e H$ and $Z$ boson fusion $e^+e^- \rightarrow e^+e^- H$ [28].

At $\sqrt{s} = 240$ GeV the dominant production process of a SM Higgs boson is Higgsstrahlung $e^+e^- \rightarrow ZH$ [29], while minor contributions come from VBF. The latter can be safely ignored because of its large t-channel suppression of the respective cross section on the order of $\ln(s/M_V^2)$ [28]. Consequently, the number of Higgs bosons coming from VBF will increase by approximately one order of magnitude as soon as the $\sqrt{s} = 365$ GeV energy point is considered. The lowest order Feynman diagrams of Higgsstrahlung and vector boson fusion are shown in Fig. 4.

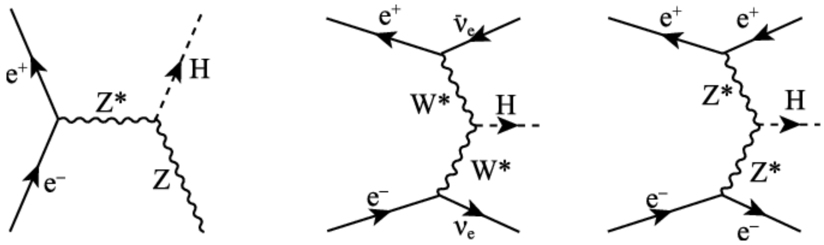

Figure 4: The production cross sections of a Higgs boson at $e^+e^-$ collisions with Higgsstrahlung (ZH) and vector boson fusion (VBF). [30]

The cross sections of various physics processes and the Higgs boson production can be found in Fig. 5.

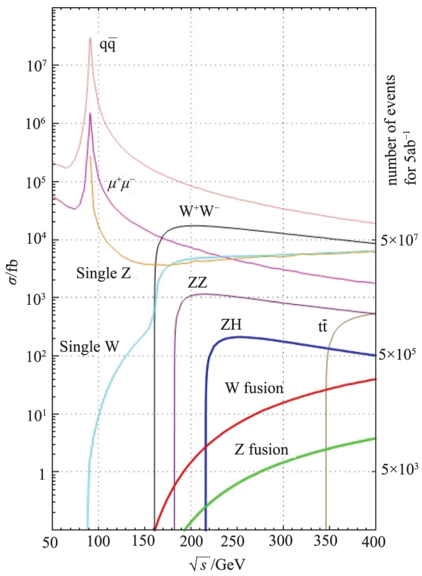

Figure 5: The production cross section and the number of events of ZH and other SM processes at $e^+e^-$ colliders with integrated luminosity of 5 ab$^{-1}$ [31].

In addition to the above mentioned channels, Higgs bosons radiating from top quarks $e^+e^- \to t\bar{t}H$ are also possible [32]. They are, however, not treated in this analysis, because Higgs bosons from this production channel are only produced in a statistically meaningful number at energies well above $\sqrt{s} = 365$ GeV.

In this thesis, we will study the Higgs boson mass, its production cross sections and the trilinear self-coupling. The goal is the precise estimation of said observables at the FCC-ee and its clean collisions. We will rely on the Monte Carlo (MC) samples produced by the FCC-ee Physics Performance working group [33]. Eighteen Higgs boson production channels are considered in the final analysis, including the hadronic ZH channels and their high production cross section. Moreover, the events are put in orthogonal categories with the purpose of increasing the overall significance.

### Background processes

At both energy points the dominant process is ZH. As the Z and the Higgs boson can decay leptonically and hadronically, a large variety of SM background processes contribute (see Fig. 5). The main background comes from fermion production $e^+e^- \to f\bar{f}$ ($f \neq t$ for $\sqrt{s} = 240$ GeV) as well as from ZZ and WW production. The former background can lead to the same final state as ZH or VBF through initial/final state radiation or due to a misreconstruction of the particles. Neutral vector boson production is included, because of the ambiguous decay of the Z and H. If one of the

Z is on-shell, fake ZH events are produced which are a priori indistinguishable from real ZH events. Furthermore, decay products from charged vector bosons are often jets, but also charged leptons and neutrinos. Thus, a good reconstruction efficiency and jet energy resolution is needed to separate the fake ZH events coming from WW and ZZ from each other.

# 2 Methods, Processes and Analysis

In this chapter, first the recoil mass is defined which is used to target the Higgs boson system in Higgsstrahlung model-independently. After introducing the categorization of events, the respective channels are discussed for 240 GeV and 365 GeV. Every inclusive channel is defined to be inclusive with respect to the Higgs boson decay (e.g. in inclusive ZH, the Higgs boson can decay into everything: $H \to X$) and every exclusive channel is defined to be exclusive with respect to the Higgs boson decay (e.g. in exclusive WW-Fusion, the Higgs boson decays into for example $H \to b\bar{b}$). Thus, from every inclusive ZH channel in which the Z decays leptonically, we can precisely determine the Higgs boson mass $m_H$ by tagging the respective leptons coming from the Z decay. Thereafter, we will discuss the extraction of the ZH and VBF signal strength modifiers and their uncertainty from all considered inclusive ZH and exclusive VBF production modes.

## 2.1 Recoil mass technique

The clean collision environment of lepton colliders such as the FCC-ee (see chapter 1.1) can be used together with ZH events to study the Higgs boson system model-independently. By measuring only the decay products of the Z, it is possible to infer the mass of the recoiling system by the virtue of energy-momentum conservation.

Assuming the center-of-mass (COM) energy $\sqrt{s}$ and the reconstructed particle energies and momenta are fully known, the initial state four-vector of the colliding particles is in the COM frame of the detector

$$\begin{aligned} p_{\text{initial}} &= p_{\text{e},1} + p_{\text{e},2} \\ &= \left( \left( \frac{\sqrt{s}}{2} + \frac{\sqrt{s}}{2} \right), 0, 0, (p_{\text{z},1} + p_{\text{z},2}) \right)^{\text{T}} \\ &= \left( \sqrt{s}, 0, 0, 0 \right)^{\text{T}}, \end{aligned} \tag{2.1}$$

where $p_{\text{z},1} = -p_{\text{z},2}$. From energy-momentum conservation, it is found that $p_{\text{initial}} \stackrel{!}{=} p_{\text{Z}} + p_{\text{H}}$. This can be rearranged to retrieve the recoil mass

$$\begin{aligned} M_{\text{Rec}}^2 &= p_H^2 \\ &= \left( E_{\text{ff}} - \sqrt{s} \right)^2 - |\vec{p_{\text{ff}}}|^2 \\ &= s - 2E_{\text{ff}}\sqrt{s} + M_{\text{ff}}^2, \end{aligned} \tag{2.2}$$

where $E_Z = E_{\text{ff}} \stackrel{!}{=} E_{\text{f},1} + E_{\text{f},2}$ and $\vec{p_Z} = \vec{p_{\text{ff}}} \stackrel{!}{=} \vec{p_{\text{f},1}} + \vec{p_{\text{f},2}}$ was used in case we fully reconstruct the decay of the Z boson ($Z \to f\bar{f}$). Moreover, the extracted recoil mass is precisely the Higgs boson mass $M_{\text{Rec}} \stackrel{!}{=} M_H$. No previous reconstruction of the Higgs boson system is necessary.

Special care must be taken, if hadronic ZH processes are considered. Since the decay products of the Z form jets which are reconstructed with much less accuracy than leptons, the statement $M_{\text{Rec}} = M_H$ is not fully true anymore.

## 2.2 Categorization and channel analysis

In this chapter, initially the Monte Carlo samples from the different generators used in the analysis are presented and discussed. After that, a categorization of events is introduced aiming to increase the sensitivity on the parameters of interest in question (discussed more in detail in chapters 3.1 and 3.4). The section concludes with the review of each channels selection cuts, unique properties and whether Boosted Decision Trees (BDTs) are necessary.

### 2.2.1 Monte Carlo samples

The signal samples as well as some background samples (see tables 18 and 19) were generated using the `WHIZARD 2.8.5` event generator [34, 35]. Their sample designation start with `wzp6`. The other samples were generated using `PYTHIA8` [36] and their respective sample designation starts with `p8`. The reason why different generators were considered is, because `WHIZARD` models the beam energy spread (BES) better than `PYTHIA8`. However, the `WHIZARD` samples do not contain parton shower ISR. The inclusion of the correct BES modelling is crucial if we want to do precision measurements of the self-coupling constants, as a very well determined initial state in terms of energy is required.

#### `WHIZARD` configurations

The `WHIZARD` samples were generated with a Gaussian BES symmetric with respect to both beams of either 0.165% for $\sqrt{s}$ = 240 GeV or 0.192% for $\sqrt{s}$ = 365 GeV, which is in accordance with the requirement of the CDR [19]. Moreover, ISR with respect to the original beam electrons is considered. The hadronization and the parton shower are handled with `PYTHIA6` [36]. For stability reasons the ISR from shower partons had to be switched off. Apart from that, the shower partons can produce final state radiation (FSR) and hadronize further. To calculate the final cross section, `WHIZARD` uses matrix elements at lowest order (LO), accounts however for the ISR by using respective approximations.

#### `PYTHIA8` configurations

The `PYTHIA8` samples also features BES. Due to the architecture of `PYTHIA8`, it has to be implemented as a spread of the longitudinal momentum $p_z$ of the beam particles and not as a spread in the energy directly. This leads to an inferior modelling of the true BES with respect to the `WHIZARD` samples and for this reason, the `PYTHIA8` samples are mainly used as flat background samples in our analysis. Finally, the partons are allowed to produce ISR and FSR. The cross section is calculated by `PYTHIA8` using LO matrix elements only and do not account for ISR.

### 2.2.2 240 GeV energy point

At the Higgsstrahlung energy point at $\sqrt{s}$ = 240 GeV, we considered the inclusive processes $Z(\to \mu^+\mu^-)H$, $Z(\to e^+e^-)H$ and $Z(\to q\bar{q})H$ and neglected VBF seeing that the corresponding cross section is very small (see Fig. 5). To shorten the notation $Z(\to \mu^+\mu^-)H$ and $Z(\to e^+e^-)H$ together are in the following chapters referred to as leptonic Higgsstrahlung (leptonic ZH) and $Z(\to q\bar{q})H$ is referred to as hadronic Higgsstrahlung (hadronic ZH). The hadronic ZH consists of six subcategories based on the reconstructed quark flavor of the $Z$ decay. In total, the events at 240 GeV are categorized in eight orthogonal categories. The individual steps of the categorization can be found in Appendix A.1. Rejected events were not considered any further and have been removed from the analysis.

For all ZH processes we used the recoil mass technique (see chapter 2.1) to extract the recoil mass distribution. The complete analysis made use of the existing FCCAnalyses framework [37].

**Used samples**

Depending on the examined decay channel of the $Z$, the respective `WHIZARD` signal sample was used. For all other processes such as charged and neutral vector boson production, s- and t-channel lepton production via a Z/$\gamma$ exchange, muon production via a di-gamma exchange (muonic $Z$ decays only) and quark production (hadronic ZH only) `PYTHIA8` samples were used. Further details of the samples (e.g. number of MC events, cross section, etc.) can be found in table 18.

The Bhabha sample contains the respective s- and t-channel diagrams and their interference, as well as cuts on the invariant mass ($M_{ee} \in [30, 150]$ GeV) and on the polar angle of the final state electrons ($\theta_{ee} \in [15°, 165°]$). For the di-gamma sample, only invariant di-muon masses above 60 GeV were considered. Furthermore, we assumed an integrated luminosity of $\mathscr{L} = 5$ ab$^{-1}$ for all channels at $\sqrt{s} = 240$ GeV corresponding to three years of data taking [19].

**Z($\rightarrow \mu^+\mu^-$)H**

The prime channel for studying Higgsstrahlung features precisely measurable Z decays due to excellent muon reconstruction. For this reason, also the reconstructed Higgs boson mass $m_H$ can be extracted very accurately. An event in this category must have two opposite sign (OS) muons in the final state. Events with two electrons are rejected due to the categorization requirement (see Appendix A.1). Apart from the number and the sign of the final state leptons other highly discriminating variables are used to eliminate the background.

| | Sample designation | Main process | MC events | Cross section |
|---|---|---|---|---|
| Signal | `wzp6_ee_mumuH_ecm240` | $e^+e^- \rightarrow Z(\mu^+\mu^-)H$ | 1'000'000 | 0.0067643 |
| Background | `p8_ee_WW_ecm240` | $e^+e^- \rightarrow W^+W^-$ | 10'000'000 | 16.4385 |
| | `p8_ee_ZZ_ecm240` | $e^+e^- \rightarrow ZZ$ | 10'000'000 | 1.35899 |
| | `wzp6_ee_mumu_ecm240` | $e^+e^- \rightarrow \mu^+\mu^-$ | 49'400'000 | 5.288 |
| | `wzp6_ee_tautau_ecm240` | $e^+e^- \rightarrow \tau^+\tau^-$ | 49'600'000 | 4.668 |
| | `wzp6_gaga_mumu_60_ecm240` | $\gamma\gamma \rightarrow \mu^+\mu^-$ | 30'000'000 | 1.5523 |

Table 1: Monte Carlo samples used for $Z(\rightarrow \mu^+\mu^-)H$ at $\sqrt{s} = 240$ GeV. The cross sections are in pb$^{-1}$.

**Selection cuts** To reduce the large background, several selection cuts were put in place on the samples of table 1. This analysis uses already optimized selection cuts [38] with variables which allow good separation between signal and background. Requiring one Z boson in the final state reduced the very abundant WW background by a large fraction. Furthermore, all events having a reconstructed invariant mass of the Z candidate between 86 and 96 GeV were kept. The Z($\rightarrow l\bar{l}$) background was further reduced by requiring that the Z candidates transverse momentum is between 20 and 70 GeV and that the reconstructed recoil mass is between 120 and 140 GeV.

Initial state radiation is efficiently cut down by selecting only events with an angle between the missing momentum vectors fulfilling $|\cos\theta_{\text{miss}}| < 0.98$. Consequently, in the selected recoil mass window only two di-gamma events are remaining.

**Results** Figure 6 shows a very concise peak around the SM Higgs boson mass of around 125 GeV. The combined background follows approximately a constant function, while the signal has a double Crystal Ball (dCB) shape. Since the background can be estimated very confidently, no further multivariate methods to isolate the signal shape have to be applied and it can be used to extract the Higgs boson mass.

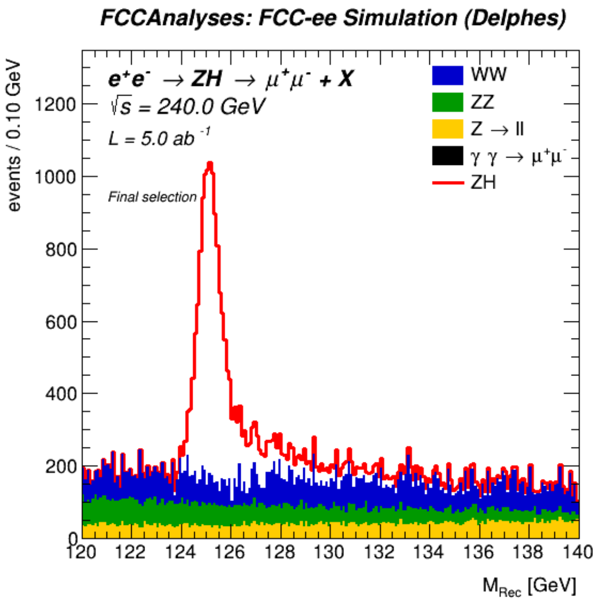


Figure 6: The recoil mass distribution from 120 to 140 GeV after applying the last selection cut described in table 2. The $Z \to ll$ channel is containing the `wzp6_ee_mumu_ecm240` and `wzp6_ee_tautau_ecm240` sample contributions together.

| | $Z(\mu^+\mu^-)$H | ZZ | WW | $Z \to \mu^+\mu^-$ | $\gamma\gamma \to \mu^+\mu^-$ |
|---|---|---|---|---|---|
| Number of events (Yield) | 21'284 | 358'861 | 949'463 | 18'115'143 | 1'309'126 |
| $Z(\mu\mu)H$ tag, $N_Z = 1$ | 100 % | 100 % | 100 % | 100 % | 100 % |
| + $M_{\mu\mu} \in [86, 96]$ GeV, $M_{\text{Rec}}$ sel. | 83.45 % | 66.35 % | 25.08 % | 0.93 % | 2.74 % |
| + $p_T^{\mu\mu} \in [20, 70]$ GeV | 74.17 % | 4.74 % | 1.58 % | 0.20 % | $4.12 \cdot 10^{-3}$ % |
| + $\lvert\cos(\theta_{\text{miss}})\rvert < 0.98$ | 70.10 % | 2.70 % | 1.58 % | 0.05 % | $1.53 \cdot 10^{-4}$ % |

Table 2: The selection cuts for $e^+e^- \to Z(\mu^+\mu^-)$H at $\sqrt{s} = 240$ GeV. The $M_{Rec}$ selection is considering events with $M_{Rec} \in [120, 140]$ GeV. Only the events passing the last selection cut are used in the final analysis. Furthermore, the column of $Z \to \mu^+\mu^-$ contains also muons from $\tau$ decays. The percentage values are rounded values and the yield is defined as $N_{MC}^{sel} \times \mathscr{L} \times \sigma$, where $N_{MC}^{sel}$ is the number of MC generator events passing the selection, $\mathscr{L} = 5$ ab$^{-1}$ is the integrated luminosity and $\sigma$ is the considered Higgs boson production cross section.

### Z($\to e^+e^-$)H

Contrary to the Z($\to \mu^+\mu^-$)H analysis, the di-gamma exchange is omitted in the electronic $Z$ decay (see table 3). Not only is there currently no centrally produced sample available, but also the selection is highly optimized (see Section 2.2.2), such that the di-gamma contribution can safely be neglected.

Since the electrons are more difficult to reconstruct than the muons due to resolution effects of the simulated IDEA detector, the resonance around the Higgs boson mass is wider than the corresponding recoil mass used in chapter 2.2.2. Corresponding to that, the height of the signal peak is reduced compared to the Z($\mu^+\mu^-$)H analysis.

**Selection cuts** Similar selection cuts were put in place to reduce the occurring background: A candidate event has to contain at least one Z with reconstructed invariant mass $m_Z^{\text{rec}} \in [86, 96]$ GeV and transverse momentum of $p_{T,Z}^{\text{rec}} \in [20, 70]$ GeV. Like in the Z($\to \mu^+\mu^-$)H case, further cuts are applied to the reconstructed recoil mass ($M_{Rec} \in [120, 140]$ GeV) and the angle between the vectors of missing momentum in the event ($\lvert\cos\theta_{\text{miss}}\rvert < 0.98$). The result of the cuts is shown in Fig. 7.

| | Sample designation | Main process | MC events | Cross section |
|---|---|---|---|---|
| Signal | `wzp6_ee_eeH_ecm240` | $e^+e^- \to Z(e^+e^-)H$ | 900'000 | 0.0071611 |
| Background | `p8_ee_WW_ecm240` | $e^+e^- \to W^+W^-$ | 10'000'000 | 16.4385 |
| | `p8_ee_ZZ_ecm240` | $e^+e^- \to ZZ$ | 10'000'000 | 1.35899 |
| | `wzp6_ee_Mee_30_150_ecm240` | $e^+e^- \to e^+e^-$ | 79'400'000 | 8.305 |
| | `wzp6_ee_tautau_ecm240` | $e^+e^- \to \tau^+\tau^-$ | 49'600'000 | 4.668 |

Table 3: Monte Carlo samples used for $Z(\to e^+e^-)H$ at $\sqrt{s} = 240$ GeV. The cross sections are in $\text{pb}^{-1}$.

| | $\text{Z}(e^+e^-)\text{H}$ | ZZ | WW | $Z \to l^+l^-$ |
|---|---|---|---|---|
| Number of events (Yield) | 17'296 | 281'345 | 745'609 | 27'171'720 |
| $\text{Z}(ee)\text{H}$ tag, $\text{N}_\text{Z} = 1$ | 100 % | 100 % | 100 % | 100 % |
| + $M_{ee} \in [86, 96]$ GeV, $M_\text{Rec}$ selection | 81.56 % | 66.65 % | 6.60 % | 1.02 % |
| + $p_T^{ee} \in [20, 70]$ GeV | 72.41 % | 4.84 % | 1.68 % | 0.24 % |
| + $\lvert\cos(\theta_\text{miss})\rvert < 0.98$ | 68.49 % | 2.83 % | 1.68 % | 0.04 % |

Table 4: The selection cuts for $e^+e^- \to \text{Z}(e^+e^-)\text{H}$ at $\sqrt{s} = 240$ GeV. The $M_{Rec}$ selection is considering events with $M_{Rec} \in [120, 140]$ GeV. Only the events passing the last selection cut are used in the final analysis. The percentage values are rounded values.

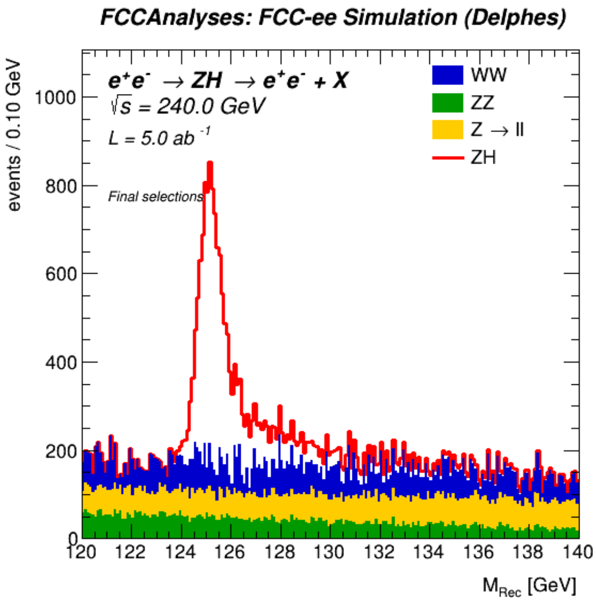


Figure 7: The recoil mass distribution from 120 to 140 GeV after applying the last selection cut described in table 4. Compared to Fig. 6 the height of the signal peak is reduced. The $Z \to ll$ channel is containing the `wzp6_ee_Mee_30_150_ecm240` and `wzp6_ee_tautau_ecm240` sample contributions together.

### $\mathbf{Z(\to q\bar{q})H}$

The $\text{Z}(\to q\bar{q})\text{H}$ channel has the highest cross section among all of the individual ZH subprocesses (see Fig. 5). Adding the respective channels to the analysis (i.e. $q \in \{u, d, s, c, b\}$) would tremendously increase its statistical significance and thus increase the final precision reach. One of the disadvantages of the inclusion of $\text{Z}(\to q\bar{q})\text{H}$ is the dependence of the result on the choice of the jet algorithm and its parameters. The tagging algorithm also influences the result in a more direct way [39]. To cluster the jets, the generalized anti-$k_T$ algorithm for $e^+e^-$ colliders implemented in FastJet 3.3.4 [40] was used with a predefined jet cone radius $\Delta R \leq 0.5$. All proto-jets with transverse momentum $p_{T,\mathrm{PJ}} > 5$ GeV were inclusively clustered and sorted with respect to their $p_{T,\mathrm{PJ}}$ and recombined according to their energy $E_{\mathrm{PJ}}$. The FCCAnalyses framework [37] allowed us to put in place specific mistag rates for the quark flavors and the chosen values for the complete analysis can be seen in table 5.

| | b tag | c tag | l tag | g tag |
|---|---|---|---|---|
| b tag | 0.80 | 0.08 | 0.01 | 0.01 |
| c tag | 0.10 | 0.60 | 0.01 | 0.03 |
| l tag | - | - | 0.80 | - |

Table 5: The assumed tagging efficiencies for the complete analysis. The rows signify the considered flavor which is desirably tagged and the columns represent the respective tagging or mistagging rates. The values for the tagging efficiencies were inspired in part by [39].

| | Sample designation | Main process | MC events | Cross section |
|---|---|---|---|---|
| Signal | `wzp6_ee_qqH_ecm240` | $e^+e^- \to Z(q\bar{q})H$ | 9'900'000 | 0.13635 |
| Background | `p8_ee_WW_ecm240` | $e^+e^- \to W^+W^-$ | 10'000'000 | 16.4385 |
| | `p8_ee_ZZ_ecm240` | $e^+e^- \to ZZ$ | 10'000'000 | 1.35899 |
| | `p8_ee_Zqq_ecm240` | $e^+e^- \to q\bar{q}$ | 10'000'000 | 52.6539 |

Table 6: Monte Carlo samples used for $Z(\to q\bar{q})H$ at $\sqrt{s} = 240$ GeV. The cross sections are in pb$^{-1}$.

**Selection cuts and flavor categorization** A large portion of the occurring background (see table 6) can be removed if the invariant mass of the reconstructed di-jet system is required to be within 86 and 96 GeV. To reject the ZZ and WW background, the reconstructed recoil mass is required to be in between 100 and 160 GeV. On top of that, the flavors of the jets of the di-jet system are extracted and they are required to be either $b$, $c$ or $l$ flavored. The $l$ flavor corresponds to light flavors $u$, $d$ and $s$. Since a simulated dataset was used, also the comparison with the Monte Carlo (MC) truth particle is included. From this, we could see that a large portion of the original signal Z($\to q\bar{q}$)H with same flavor $q \in \{b, c\}$ is leaking inside events where the di-jet system consists of e.g. a $b$ quark and a quark of a different flavor. This can be explained with the imperfect reconstruction of the jet with respect to the original MC particle due to the chosen mistag rates (see table 5) and due to jet clustering, since the flavor of the components of the jet are not extracted.

Thus, the different permutations of $b$-, $c$- and $l$-jets coming from the Z are promoted to orthogonal categories (see Appendix A.1) and through that, the full Z($\to q\bar{q}$)H is extracted. The jets are categorized in $bb$, $bj/jb$, $ij$, $cc$, $cj/jc$ and $bc/cb$, where $i, j$ stands for light jets ($u, d$ and $s$). For this purpose, it is important that the events in the individual categories are not being double counted as this might lead to wrong results. Orthogonality was ensured between all jet flavor channels as well as with the previous categories Z($\to \mu^+\mu^-$)H and Z($\to e^+e^-$)H.

As the total background (especially $Z \to q\bar{q}$) is overwhelming (see Fig. 8a), Adaptive Boosted Decision Trees (BDTs) were used for all hadronic Z decays at 240 and 365 GeV to lower this background to a minimal level. The BDTs were constructed using ROOT and its TMVA framework [41, 42]. The parameters for setting up the BDT were inspired from [43]. For each BDT, the composition of the training set depends on the preselected number of events of the considered Z jet flavors. The remaining parameters, as well as the input variables for discrimination are fixed globally for each channel and do not change between the energy points. In total, 800 trees were trained with a learning rate of $\beta_{\mathrm{Ada}} = 0.1$, each with a minimum node size of 1% and with a maximum depth of 3 to limit overtraining. Furthermore, the Gini index [44] was chosen as a measure of separation. After training

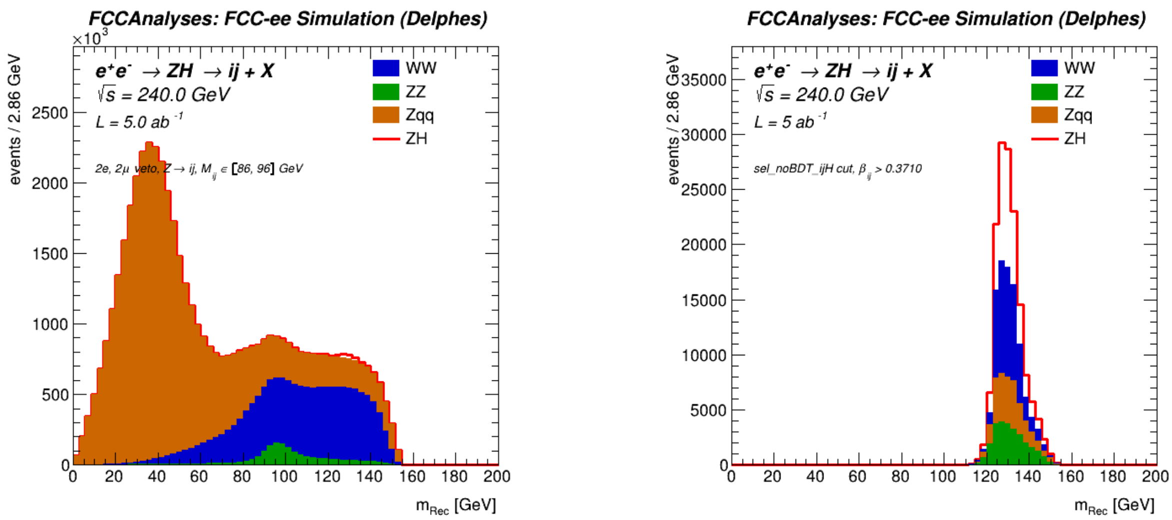


(a) (b)

Figure 8: (a): Recoil mass of ZH events where Z decays in light jets at 240 GeV. The $Z \to q\bar{q}$ background is overwhelming. (b): The recoil mass distribution of the same decay but after an additional BDT cut. The $Z \to q\bar{q}$ background is efficiently cut down.

and testing of the BDT, a final classifier for each category has been computed. For the selection cuts, only the classifiers from the respective category were used.

The performance of the final classifier is driven by the most discriminating variables of the BDT. Depending on the channels considered, the most discriminating variables differ. In case of the Z decays involving a $b$ flavor, the most discriminating variable is the number of $b$-jets in the final state. This can be explained with the high $b$ quark tagging efficiency seen in table 5. Since the $c$ tagging efficiency is slightly lower, it is not surprising that the most discriminating variable in the cases where the Z decays into at least one $c$ is not the number of $c$-jets in the final state. In these cases, it is the recoil mass $M_{\text{Rec}}$ $(cc)$ and the di-jet mass $M_{qq}$ $(cj/jc,\ ij)$. The di-jet mass $M_{qq}$ is the second most discriminating variable in every other category ($bb$, $bc/cb$ and $bj/jb$). It must be noted that the specific choice of the jet clustering algorithm and its parameters, as well as the tagging efficiency introduces some model dependence.

Considering the recoil mass distribution with respect to the di-jet mass distribution, one notices that for the background $Z \to q\bar{q}$, the mean di-jet mass of the reconstructed Z system prior the application of the BDT is shifted towards slightly smaller values instead of $M_{qq} \approx M_Z$. Because of initial state radiation, the collision energy is slightly reduced, leading to a smaller di-jet mass. The effect is eliminated by requiring cuts which aim to reduce unobserved ISR (very close to beam pipe and low $p_T$) such as $p_T \geq 20$ GeV together with $|\cos\theta_{\text{Miss}}| < 0.9$ [45].

The ISR eliminating cuts are preferred by the BDT, since the involved variables are one of the more discriminating ones and due to the choice of the Gini metric as decision metric (see Fig. 9). Indeed when looking at the post-BDT di-jet mass distributions a peak around $M_Z$ becomes apparent in every channel (see Appendix E.1).

### 2.2.3 365 GeV energy point

The total number of signal events can be increased, if events at the $tt$ threshold ($\sqrt{s} = 365$ GeV) are taken into account. Also, at $\sqrt{s} = 365$ GeV the VBF processes become non-negligible, and they have to be considered. We examined only exclusive VBF processes in which the Higgs boson decays to a pair of $b$ quarks, because of its higher branching ratio compared to other quarks or

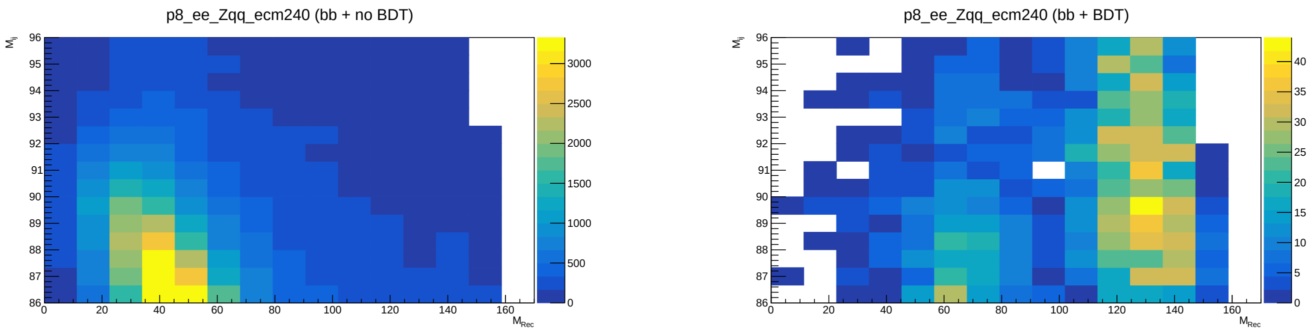


(a)

(b)

Figure 9: A 2D distribution with the recoil mass $M_{\text{Rec}} \in [0, 170]$ GeV on the x axis and the di-jet mass $M_{ij} \in [86, 96]$ GeV on the y axis. Both plots show the PYTHIA8 $Z \to q\bar{q}$ background sample where $q, \bar{q} = b$. (a): The situation before the BDT. Events cluster at a recoil mass of around 45 GeV and around a di-jet mass of around 87 GeV. (b): After the BDT, most events cluster between a recoil mass of 120 and 140 GeV and around a correct di-jet mass of 90 GeV.

leptons. One reason for this is the large WW background occurring in both neutral and charged VBF (see Appendix G) which can be confidently limited by considering a pair of $b$ quarks (or $c$ quarks if the $c$ tagging efficiency would be higher) coming from the same particle in the final state as already demonstrated in chapter 2.2.2. Otherwise this would pose a serious issue for the charged VBF $e^+e^- \to \nu_e\bar{\nu}_e H$ and the current baseline IDEA detector without any improvement in regards of jet tagging.

A similar categorization procedure as in the 240 GeV case is applied and since more channels through VBF are accessible, the flowchart was expanded accordingly (see Appendix A.2).

#### Used samples

The corresponding 365 GeV version of the 240 GeV MC samples are used for this analysis. Since additional VBF contributions appear due to the logarithmic rise of the cross section, the `WHIZARD` signal sample is used to account for charged VBF after the electron neutrinos are isolated using MC truth information. Moreover, due to the more prominent contribution of the neutral VBF at 365 GeV, the `wzp6_ee_eeH_ecm365` sample must be separated in ZH, VBF and the respective interfering part. When considering VBF, the ZH appears as a background and for this reason the respective `PYTHIA8` sample is used. In table 19, every sample used in the 365 GeV analysis is listed.

To avoid double counting, the ZH part of the signal sample is removed and taken into account by the background sample when either WW- or ZZ-Fusion is considered.

Like in the 240 GeV case, the Bhabha sample contains s- and t-channel diagrams as well as their interference and the same cuts mentioned in chapter 2.2.2. The same is true for the di-gamma sample. For the analysis, we assumed an integrated luminosity of $\mathscr{L} = 1.5\ \text{ab}^{-1}$ for all considered channels at $\sqrt{s} = 365$ GeV. This corresponds to the integrated luminosity collected after five data taking years.

#### $\mathbf{Z(\to \mu^+\mu^-)H}$

At 240 GeV, the Higgs boson mass could be precisely extracted due to the accurate measurement of the remnants of the Z boson. In case of the muonic decay of the Z, only the tracker can be used to estimate the transverse momentum of the muons. Recalling the performance of the proposed drift chamber (Fig. 2), it becomes evident that at $\sqrt{s} = 365$ GeV we can expect a much less precise measurement of the Higgs boson mass in the leptonic ZH processes.

| | Sample designation | Main process | MC events | Cross section |
|---|---|---|---|---|
| Signal | wzp6_ee_mumuH_ecm365 | $e^+e^- \to Z(\mu^+\mu^-)H$ | 200'000 | 0.004185 |
| Background | p8_ee_WW_ecm365 | $e^+e^- \to WW$ | 5'000'000 | 10.7165 |
| | p8_ee_ZZ_ecm365 | $e^+e^- \to ZZ$ | 5'000'000 | 0.6428 |
| | wzp6_ee_mumu_ecm365 | $e^+e^- \to \mu^+\mu^-$ | 9'900'000 | 2.287 |
| | wzp6_ee_tautau_ecm365 | $e^+e^- \to \tau^+\tau^-$ | 10'000'000 | 2.017 |
| | wzp6_gaga_mumu_60_ecm365 | $e^+e^- \to \gamma\gamma \to \mu^+\mu^-$ | 10'000'000 | 2.843 |

Table 7: Monte Carlo samples used for $Z(\to \mu^+\mu^-)H$ at $\sqrt{s} = 365$ GeV. The cross sections are in $\text{pb}^{-1}$.

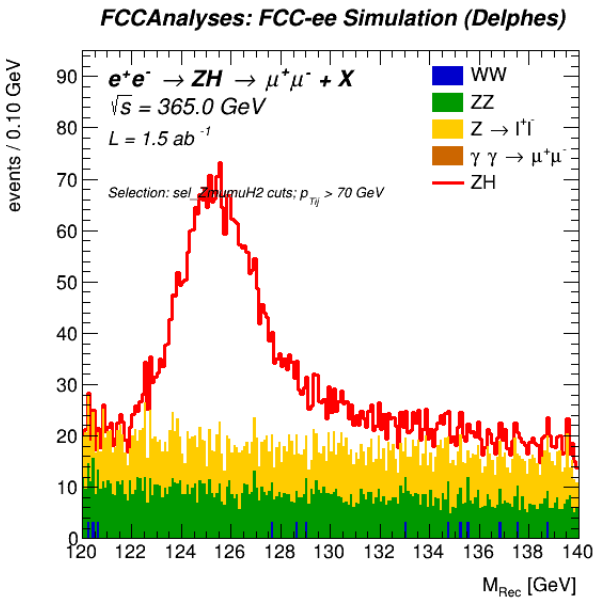


Figure 10: The recoil mass distribution from 120 to 140 GeV after applying the last selection cuts from table 8.

**Selection cuts** For the selection, similar cuts as in the 240 GeV case were used. We have to replace the selection on the transverse momentum of the di-lepton system with $p_T > 70$ GeV noting that the higher $\sqrt{s}$ produces more energetic Z candidates. This cuts down the background from $\gamma\gamma \to \mu^+\mu^-$ as well ($p_T \leq 20$ GeV), suppresses the WW background by roughly a factor of 2 and slightly reduces the ZZ background whilst leaving the signal almost untouched. The considered MC samples are listed in table 7.

| | Z($\mu^+\mu^-$)H | ZZ | WW | $Z \to l^+l^-$ | $\gamma\gamma \to \mu^+\mu^-$ |
|---|---|---|---|---|---|
| Number of events (Yield) | 4'877 | 53'655 | 184'776 | 2'225'401 | 693'722 |
| $Z(\mu\mu)H$ tag, $\text{N}_Z = 1$ | 100 % | 100 % | 100 % | 100 % | 100 % |
| + $M_{\mu\mu} \in [86, 96]$ GeV, $M_{\text{Rec}}$ selection | 56.90 % | 5.58 % | 0.04 % | 0.60 % | 0.24 % |
| + $p_T^{\mu\mu} > 70$ GeV | 52.82 % | 3.11 % | 0.02 % | 0.08 % | 0 % |

Table 8: The selection cuts for $e^+e^- \to Z(\mu^+\mu^-)H$ at $\sqrt{s} = 365$ GeV.

**Results** As expected from the degraded momentum resolution of the drift chamber, Figure 10 shows a smeared peak around the SM Higgs boson mass of around 125 GeV compared to Fig. 6.

The recoil mass distribution in Fig. 10 uses the dataset after applying the last selection cut in table 8. Like in the 240 GeV case, the background from all sources follows a very flat function while the signal shape can be modelled with a double Crystal Ball function.

### Z($\rightarrow e^+e^-$)H

The decay electrons of the Z in the electronic ZH are measured in the tracker (estimation of their $p_T$) and in the calorimeter (estimation of their energy), contrary to the tracker only measurement in case of the muonic ZH. Because of the higher COM energy, the VBF also contributes to this channel and acts as background (see table 9). The other SM background is the charged and neutral vector boson production and because an inclusive Higgs boson decay is considered, also Bhabha scattering and electrons from $\tau$ decays in case the decay products of the Higgs boson are misreconstructed or ISR/FSR is faking ZH events. Furthermore, we expect a less precise measurement of $m_H$ because of the worse performance of the drift chamber for the considered $p_T$ range.

| | Sample designation | Main process | MC events | Cross section |
|---|---|---|---|---|
| Signal | `wzp6_ee_eeH_ecm365` | $e^+e^- \rightarrow e^+e^-H$ | 400'000 | 0.00739 |
| | `p8_ee_ZH_ecm365` | $e^+e^- \rightarrow ZH$ | 5'000'000 | 0.1173 |
| Background | `p8_ee_WW_ecm365` | $e^+e^- \rightarrow WW$ | 5'000'000 | 10.7165 |
| | `p8_ee_ZZ_ecm365` | $e^+e^- \rightarrow ZZ$ | 5'000'000 | 0.6428 |
| | `wzp6_ee_Mee_30_150_ecm365` | $e^+e^- \rightarrow e^+e^-$ | 10'000'000 | 1.53 |
| | `wzp6_ee_tautau_ecm365` | $e^+e^- \rightarrow \tau^+\tau^-$ | 10'000'000 | 2.017 |

Table 9: Monte Carlo samples used for $e^+e^- \rightarrow Z(e^+e^-)H$ at $\sqrt{s} = 365$ GeV [33]. The cross sections are in pb$^{-1}$.

Realizing that the signal in this channel is ZH and the `WHIZARD` sample carries also contributions from VBF and the interference term, they have to be separated by using MC truth information. The `PYTHIA8` sample `p8_ee_ZH_ecm365` is then used to account for the events coming from the interference term, which are lost due to the separation. The selection was done on generator level partons of the `PYTHIA8` sample, retaining only MC events where the invariant mass of the MC Z system $m_Z^{\mathrm{MC}}$ is above 110 GeV. This value of the invariant mass was chosen such most of the VBF contribution was cut from the `WHIZARD` sample, yet keeping the number of events from the `PYTHIA8` sample at a minimum. This ensures, that the signal events mainly come from the `WHIZARD` sample.

**Selection cuts** In addition to the sample separation cut, additional selections were put in place to reduce the occurring background coming from SM sources: An candidate event has to contain at least one Z with reconstructed invariant mass $m_Z^{\mathrm{rec}} \in [86, 96]$ GeV. The reconstructed recoil mass had to fulfill $M_{Rec} \in [120, 140]$ GeV and the angle between the vectors of missing momentum in the event was chosen such that it satisfies $|\cos\theta_{\mathrm{miss}}| < 0.98$.

| | Z($e^+e^-$)H | ZZ | WW | $Z \rightarrow l^+l^-$ |
|---|---|---|---|---|
| Number of events (Yield) | 2'996 | 25'330 | 3'475 | 421'605 |
| Z($ee$)H tag, $\mathrm{N_Z} = 1$ | 100 % | 100 % | 100 % | 100 % |
| + $M_{ee} \in [86, 96]$ GeV, $M_{\mathrm{Rec}}$ selection | 68.49 % | 8.54 % | 1.84 % | 1.92 % |
| + $|\cos(\theta_{\mathrm{miss}})| < 0.98$ | 65.65 % | 5.22 % | 1.47 % | 0.11 % |

Table 10: The selection cuts for $e^+e^- \rightarrow$ Z($e^+e^-$)H at $\sqrt{s} = 365$ GeV. The $M_{Rec}$ selection is considering events with $M_{Rec} \in [120, 140]$ GeV. Only the events passing the last selection cut are used in the final analysis. The percentage values are rounded values.

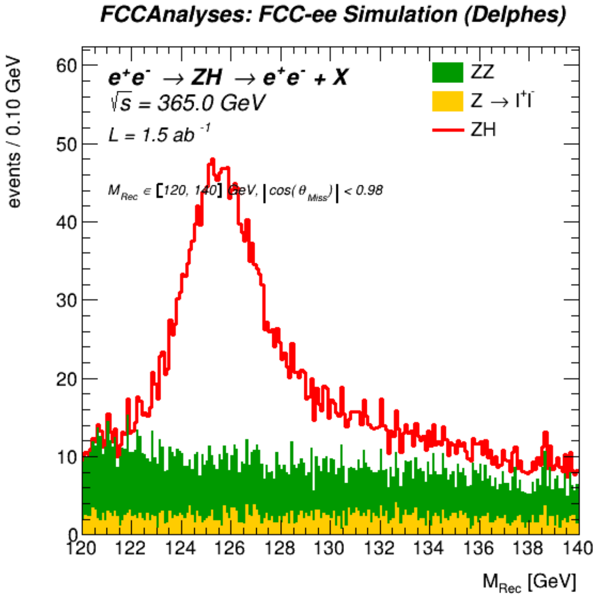


Figure 11: The recoil mass distribution from 120 to 140 GeV after applying the last selection cut described in table 10. The $Z \to ll$ channel is containing the `wzp6_ee_Mee_30_150_ecm365` and `wzp6_ee_tautau_ecm365` sample contributions together.

**Results** The final recoil mass distribution is shown in Fig. 11. As already mentioned in the previous section, the width of the signal distribution is wider compared to the 240 GeV channel because of resolution effects. The charged vector boson production channel WW has been omitted from the Figure, as it introduces unphysical spikes to the distribution due to the small number of MC events in the final selection. This does not degrade the meaningfulness of the analysis, since the number of WW events are small (51 events after final selection) and expected to be flat in the recoil mass distribution. The effect of the missing WW events are well within the bin-wise statistical uncertainty of the ZZ and $Z \to l^+l^-$ background events.

### Exclusive WW-Fusion

Until now, the recoil mass technique was used to get a hold on the Higgs system model-independently. This approach changes as soon as VBF is considered, since there is no Z the Higgs boson can recoil against. Charged VBF involves a pair of neutrinos in the final state accompanying the Higgs boson and thus, the missing mass $M_{\text{miss}}$ is used instead.

The main signal is VBF, which together with the ZH channel, completes the intermediate possibilities of a $\nu_e\nu_e$H final state. The `WHIZARD` signal sample is made of ZH, VBF and the interference between the former processes. Thus, the ZH events in the `WHIZARD` sample have to be eliminated in order to avoid double counting. This is done with the MC truth information from the sample, which is then used to identify the events whose electron neutrinos come from a $e\nu_eW$ vertex. If events contain two such neutrinos, then this is declared a charged VBF event. To remove as much as possible from the interference, an additional selection on the polar angular distribution of the Higgs boson is made [28]. Every MC sample involved in this analysis is listed in table 11.

**Selection cuts** The categorization of events requires, that the final state of any charged VBF event is either free of any charged lepton system or contains two electrons and two muons. Moreover, it has to contain at least two jets with an invariant mass $m_{qq}$ fulfilling $|m_{qq} - m_H| \geq 30$ GeV. For the exclusive $e^+e^- \to \nu_e\bar{\nu}_eH(\to b\bar{b})$, at least two $b$-jets are required to be in the final state. To make sure, that the considered $b$-jets are coming from a Higgs boson decay, additional cuts are applied:

| | Sample designation | Main process | MC events | Cross section |
|---|---|---|---|---|
| Signal | `wzp6_ee_nunuH_ecm365` | $e^+e^- \rightarrow \nu\bar{\nu}H$ | 1'000'000 | 0.05394 |
| Background | `p8_ee_WW_ecm365` | $e^+e^- \rightarrow WW$ | 5'000'000 | 10.7165 |
| | `p8_ee_ZZ_ecm365` | $e^+e^- \rightarrow ZZ$ | 5'000'000 | 0.6428 |
| | `p8_ee_ZH_ecm365` | $e^+e^- \rightarrow ZH$ | 5'000'000 | 0.1173 |

Table 11: Monte Carlo samples used for the charged VBF at $\sqrt{s} = 365$ GeV [33]. The cross sections are in $\text{pb}^{-1}$.

The absolute difference in pseudorapidity between the two $b$-jets must be smaller than 3 and the hadronic activity $H_T$ has to be larger than 20 GeV. Lastly, a MET cut (MET > 20 GeV) is applied to eliminate background with final states containing two electrons and two muons and no neutrinos or insufficiently reconstructed particles.

| | WW-Fusion | ZZ | WW | ZH |
|---|---|---|---|---|
| Number of events (Yield) | 690 | 406 | 6 | 616 |
| WW-Fusion tag, $\lvert\Delta\eta_{bb}\rvert < 3, H_T > 20$ GeV, MET > 20 GeV | 100 % | 100 % | 100 % | 100 % |
| + $\beta_{WW} >$ -0.0426 | 97.97 % | 12.81 % | 0 % | 31.01 % |

Table 12: The selection cuts for charged VBF at $\sqrt{s} = 365$ GeV. Only the events passing the last selection cut are used in the final analysis. The percentage values are rounded values.

From table 12 it becomes apparent, that even after the cuts ZZ and ZH backgrounds are still present. This is expected, recalling that the Z and the H can both decay into electron neutrinos and $b$ quarks. On the other hand, the WW contribution has been efficiency cut down due to the $b$-jet requirement. To further separate the ZZ and irreducible ZH background from the signal, an adaptive BDT was trained with 7'500 signal and 50'000 background events. The rest of the parameters (number of trees, learning rate, minimum node size and maximum depth of a tree) did not change with respect to the BDTs used in chapter 2.2.2. As input variables, discrete ones (number of jets and number of $b$-jets) as well as continuous ones related mainly to jets and missing energy were chosen. The most discriminating variable is the number of $b$-jets, which is due to the high branching fraction of the Higgs boson decaying in $b$ quarks and the superior tagging efficiency of the $b$-jets. Apart from that, the hadronic activity is the second most discriminating variable followed by the jet number and the missing transverse energy. The last three variables rank among the most discriminating ones because the final state is required to contain neutrinos (leads to MET) and $b$-jets (i.e. jets). So, the only visible energy is coming from the $b$-jets and possible hadronization which is measured by the hadronic activity.

Due to the irreducible nature of the ZH background, it cannot be completely removed (see Fig. 12b). The ZZ background has been cut down efficiently exploiting kinematic differences in the processes, while the WW contribution has been removed entirely.

#### Exclusive ZZ-Fusion

The exclusive $e^+e^- \rightarrow e^+e^-H(b\bar{b})$ give us the possibility to study the neutral VBF at $\sqrt{s} = 365$ GeV. Recalling that the respective cross section is smaller than the charged VBF and background coming from WW is too high, an exclusive approach was chosen in which we can use the invariant mass of the $e^+e^-$ recoiling against the Higgs system.

Contributing SM background processes (see table 13) are $WW$ and $ZZ$ production, as well as ZH in which the Z decays in a pair of electrons and the Higgs boson in a pair of $b$ quarks. The ZH process

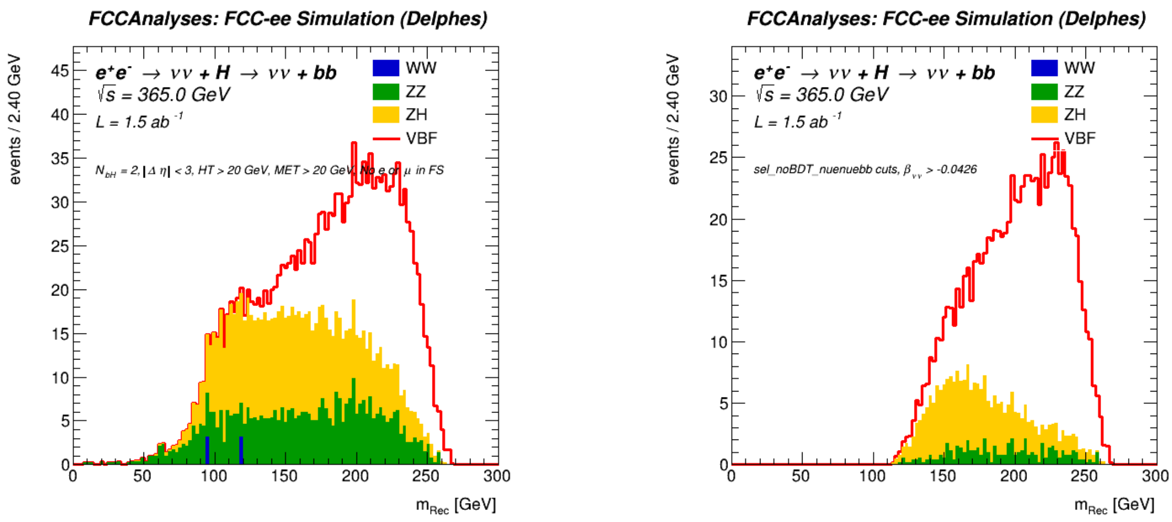


(a) (b)

Figure 12: (a): Missing mass of charged VBF events where H decays to two $b$-jets. Especially in the low mass region the ZH background is considerable. (b): The missing mass distribution of the same decay but after an additional BDT cut.

acts as an irreducible background of neutral VBF, similar to the charged VBF (see Section 2.2.3), while the $WW$ and $ZZ$ background can be reduced by exploiting kinematic differences. To suppress the ZH contributions from the `WHIZARD` sample, only generator level events with electronic invariant masses of $M_{e^+e^-} > 110$ GeV are considered. To avoid double counting, the cut was reversed for the `PYTHIA8` ZH sample.

| | Sample designation | Main process | MC events | Cross section |
|---|---|---|---|---|
| Signal | wzp6_ee_eeH_ecm365 | $e^+e^- \to e^+e^-H$ | 400'000 | 0.00739 |
| Background | p8_ee_WW_ecm365 | $e^+e^- \to WW$ | 5'000'000 | 10.7165 |
| | p8_ee_ZZ_ecm365 | $e^+e^- \to ZZ$ | 5'000'000 | 0.6428 |
| | p8_ee_ZH_ecm365 | $e^+e^- \to ZH$ | 5'000'000 | 0.1173 |

Table 13: Monte Carlo samples used for the neutral VBF at $\sqrt{s} = 365$ GeV [33]. The cross sections are in pb$^{-1}$.

**Selection cuts and results** In accordance with the categorization flowchart for $\sqrt{s} = 365$ GeV (see Appendix A.2), ZZ-Fusion events must contain two electrons and not two muons in the final state. Furthermore, the two electrons must not come from a Z decay ($|m_{ee} - m_Z| \geq 6$ GeV) and the final state must contain at least two $b$-jets. Apart from that, the cuts concerning the Higgs system are the same as in chapter 2.2.3. The selection on the missing transverse energy has been omitted since no neutrinos are expected to be present in the signal final state. The missing mass distribution without the BDT cut is shown in Fig. 13a.

| | ZZ-Fusion | ZZ | WW | ZH |
|---|---|---|---|---|
| Number of events (Yield) | 225 | 89 | 3 | 61 |
| ZZ-Fusion tag, $\|\Delta\eta_{bb}\| < 3, H_T > 20$ GeV | 100 % | 100 % | 100 % | 100 % |
| + $\beta_{bb} > -0.1034$ | 99.56 % | 13.48 % | 0 % | 3.28 % |

Table 14: The selection cuts for neutral VBF at $\sqrt{s} = 365$ GeV. Only the events passing the last selection cut are used in the final analysis. The percentage values are rounded values.

To eliminate further the ZZ and ZH background, an adaptive BDT was trained with 5'000 signal events and 50'000 background events. The choice of the hyperparameters is the same as in the charged VBF BDT. Among the input variables are again variables related to the Higgs system, such as the number of $b$-jets, but also variables related to the $e^+e^-$ system. The most discriminating variable is the invariant mass of the electrons, which in the case of ZH and ZZ clusters around the Z mass (WW events cluster around the W mass) whereas for VBF it assumes larger values. Followed by the number of $b$-jets, missing transverse energy (Z in ZH can decay in neutrinos) and the invariant mass of the $b$-jets (Z in ZZ can decay in electrons and the other in $b$ quarks). Utilizing variables related to the hadronic Higgs decay and the electrons (both visible systems) increases the separation power of the BDT. Consequently, the overall background from all sources gets reduced to only a few events in each channel (see Fig. 13b and table 14).

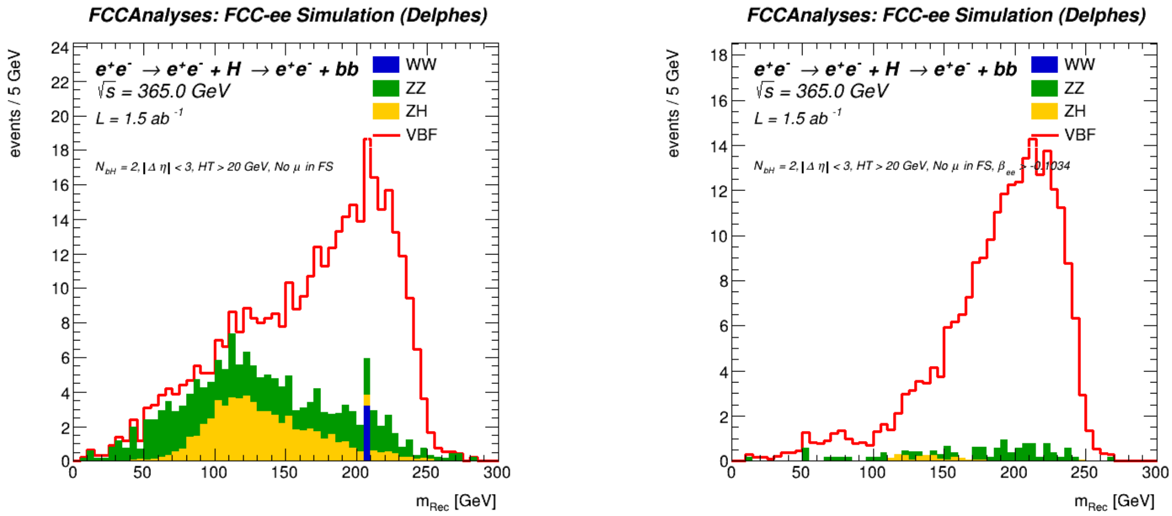


(a) (b)

Figure 13: (a): Recoil mass of neutral VBF events where H decays to two $b$-jets. In the low mass region, the ZH background clusters around the Higgs boson mass, while the ZZ background is almost flat. The spike of the WW background close to 210 GeV is unphysical and it is due to only one MC event in this bin combined with the high background cross section (10.7165 $\mathrm{pb}^{-1}$). (b): The recoil mass distribution of the same decay but after an additional BDT cut. The background is almost completely cut down.

## Z($\rightarrow q\bar{q}$)H

As in the 240 GeV case, the hadronic ZH has the highest cross section among all Higgs boson production processes at 365 GeV (see Fig. 5). Adding it would increase the sensitivity on the measured Higgs boson observables considerably with respect to the 240 GeV hadronic ZH inclusion. Again, we categorize the events (see table 15) according to the flavor of jets which can be attributed to the Z (after a mass cut) and proceed analogously as in chapter 2.2.2.

**Selection cuts and flavor categorization** The categorization requires, that the final state is either free of any charged leptons or contains two electrons and two muons. At least two jets should be present in the final state and its invariant mass has to fulfill additionally $|m_{qq} - m_H| > 30$ GeV. To ensure that the jets come from the Z, we require $m_{qq} \in [86, 96]$ GeV. After flavor-tagging the jets with the efficiencies from table 5, six orthogonal categories are created: $bb$, $bc/cb$, $bj/jb$, $cc$, $cj/jc$ and $ij$ where $i, j \in \{u, d, s\}$.

To reduce the abundant background contribution from $e^+e^- \rightarrow q\bar{q}$ and WW, an adaptive BDT was

| | Sample designation | Main process | MC events | Cross section |
|---|---|---|---|---|
| Signal | wzp6_ee_qqH_ecm365 | $e^+e^- \to Z(q\bar{q})H$ | 2'000'000 | 0.084307 |
| Background | p8_ee_WW_ecm365 | $e^+e^- \to WW$ | 5'000'000 | 10.7165 |
| | p8_ee_ZZ_ecm365 | $e^+e^- \to ZZ$ | 5'000'000 | 0.6428 |
| | p8_ee_Zqq_ecm365 | $e^+e^- \to q\bar{q}$ | 59'500'000 | 21.4149 |

Table 15: Monte Carlo samples used for the hadronic ZH at $\sqrt{s} = 365$ GeV [33]. The cross sections are in $\text{pb}^{-1}$.

trained per category. The number of signal and background events used to train the BDTs depend per category and mostly variables related to the Z system are used as input variables: The energy and the transverse momentum of the jets, the azimuthal and pseudorapidity difference between the two jets, the recoil mass and the invariant mass of the Z system, the hadronic activity, the missing transverse energy and its angle with respect to the beam pipe and finally the number of $b$-jets and the number of ordinary jets. After the training and testing of the BDTs, the six final classifiers had been computed. For every category, the number of jets was the most discriminating variable (ZH events cluster around higher values), followed by the number of $b$-jets for each channel involving signal $b$-jets. Another high-ranking variable is the hadronic activity which can be used to separate between ZH and $q\bar{q}$.

The result of the cutflow before and after the cut on the BDT classifiers are in table B.2. The relative performance of the BDT is slightly better for the $bb$, $cc$ and $ij$. It has to be noted however, that all BDTs at $\sqrt{s} = 365$ GeV suffer from the same optimistic separation due to ISR effects as seen in chapter 2.2.2. After the training of the BDT, the ISR reducing cuts get preferred and finally only events with the correct invariant di-jet mass are chosen to remain in the dataset. The full pre- and post-BDT 2D distributions ($M_{\text{Rec}}, M_{ij}$) for each flavor category can be found in the Appendix E.2.

# 3 Results

In this chapter, different routes are explored how the analysis of the ZH and VBF channels can be used to estimate the sensitivity of the Higgs boson mass $m_H$, the signal strength parameter $\mu$ and the deviation of the Higgs boson self-coupling from the SM value $\kappa_\lambda$. The first section introduces the statistical model and motivates the signal strength modifiers. These are used to extract the Higgs boson production cross section and also play a role in the estimation of the Higgs boson self-coupling. After that, the sensitivity of measuring the Higgs boson mass is determined when combining the leptonic ZH channels at 240 and 365 GeV. Followed by the estimation of the signal strength parameter combining all ZH channels at separate energies ($\mu_{ZH}$) as well as the separate VBF channels ($\mu_{VBF,WW}$ and $\mu_{VBF,ZZ}$). The chapter concludes with the treatment of the precision reach of $\kappa_\lambda$ at the FCC-ee considering all available channels (ZH and VBF).

## 3.1 Statistical model and fitting

In the following, the statistical models describing the observed mass distributions in the single-Higgs production channels are introduced. The signal strength parameter $\mu_i^f$ for a particular production $i$ and decay process $f$ can be extracted directly from the expected number of signal events. In section 3.4 we motivate the $\kappa$ framework and how it can be used to probe the validity of the SM. We find that the Higgs boson trilinear self-coupling $\kappa_\lambda$ appear in a correction to the production cross section and can thus be treated model-wise in the same way as the signal strength modifiers.

Assuming a single narrow resonance for the Higgs boson centered around 125 GeV and that its intrinsic width $\Gamma_H$ is very small (zero width approximation), the signal strength parameter can be defined as the ratio

$$\mu_i^f := \frac{\sigma_i}{(\sigma_i)_{\mathrm{SM}}} \times \frac{BR^f}{(BR^f)_{\mathrm{SM}}} = \mu_i \times \mu^f \tag{3.1}$$

where $\sigma_i$ and $(\sigma_i)_{\mathrm{SM}}$ are the observed and expected Higgs boson production cross sections of the process $i$ respectively and $BR^f$ and $(BR^f)_{\mathrm{SM}}$ are the observed and expected Higgs boson branching ratios of a process $f$ respectively. For the inclusive Higgs boson decays, we set $(BR)_{\mathrm{SM}} := 1$.

The assumptions made to introduce the signal strength parameter are experimentally well justified [46] and because of its definition as a ratio, it is especially useful for testing the SM for the reasons highlighted in chapter 1.

The expected number of signal events can be parametrized as $N_{sig} = \mu_i^f \cdot \epsilon \cdot \mathscr{L} \cdot (\sigma_i \cdot BR^f)_{\mathrm{SM}}$, where $\mu_i^f$ is the signal strength modifier, $\epsilon := N_{\mathrm{sig}}^{\mathrm{sel}}/N_{\mathrm{sig}}^{\mathrm{tot}}$ is the signal selection efficiency and $\mathscr{L}$ the integrated luminosity.

In the leptonic decay channels of the $Z$, an additional parameter of interest (POI) is introduced: the reconstructed Higgs boson mass $m_H$. The principal observable used in the statistical inference is the recoil mass $\mathrm{M_{Rec}}$ calculated using the recoil mass technique introduced in chapter 2.1. All other parameters which describe the shape of the distribution are called nuisance parameters $\vec{\theta_j}$, where $j \in \{s, b\}$ correspond to either signal or background nuisance parameters respectively.

The POI are extracted using an unbinned extended maximum likelihood fit [47] of a function to the dataset of each considered process:

$$L(\mathcal{D}, \mathcal{G}|\alpha) = \prod_{c \in \mathcal{D}} \left[ \mathrm{Pois}(n_c|\nu_c(\alpha)) \prod_{i=1}^{n_c} L_c(\mathrm{M}_{\mathrm{Rec}}^{c,i}|\alpha) \right] \times \prod_{p \in \mathcal{S}} L_p(\hat{\theta}_{\mathrm{glob,p}}|\alpha_{glob,p}) \tag{3.2}$$

where $\mathcal{D}$ and $\mathcal{G}$ correspond to the vector of individual datasets of the channels and of global observables $\alpha_{glob}$ respectively. The number of observed and expected events for a given channel is denoted with $n_c$ and $\nu_c(\alpha)$. To shorten the notation, the POI and the nuisance parameters are written as $\alpha = (\mu, \vec{\theta_j})$. The set $\mathcal{S}$ contains the constraint terms and $\hat{\theta}_{\mathrm{glob,p}}$ corresponds to the estimator of the global observable.

The bare model $L_c(\mathrm{M_{Rec}}|\alpha)$ without any constraint terms (see eq. 3.3) is a function of the signal and background normalization and the respective probability density functions (PDFs): $S$ and $B$.

$$L_c(\mathrm{M_{Rec}}|\alpha) = N_{sig}(\mu) * S(\mathrm{M_{Rec}}|\vec{\theta_s}) + N_{bkg} * B(\mathrm{M_{Rec}}|\vec{\theta_b}) \tag{3.3}$$

Known sources of systematic uncertainties $\theta_{\mathrm{sys}}$ are taken into account with a Gaussian function $G(\theta_{\mathrm{sys}}|\theta_{\mathrm{sys,true}}, \sigma_{\theta_{\mathrm{sys,true}}})$ which is multiplied with the model (see last term of eq. 3.2).

Constraints on a POI made by measurements of other experiments can be taken into account the same way. In this case, the mean of the Gaussian is the externally measured value and the width is the (Gaussian) measurement uncertainty made by the other experiment.

## 3.2 Higgs boson mass measurement

The Higgs boson mass is measured by taking into account the leptonic ZH processes measured at 240 GeV and 365 GeV only. This is done, because the recoil mass resolution is degraded by the inferior hadronic energy resolution of the dual readout calorimeter (see chapter 1.1). The datasets obtained by applying the final selection cuts for each leptonic channel are fitted to a signal PDF $S(M_{\text{Rec}}|\vec{\theta_s})$ consisting of a sum of two one-sided Crystal Ball shapes together with a Gaussian function. The Crystal Ball functions shared the same mean (the Higgs boson mass parameter) and width, while the rest of their parameters are kept floating. Moreover, the mean and the width of the Gaussian have been left floating as well. The background was parametrized with a second order polynomial function $B(\text{M}_{\text{Rec}}|\vec{\theta_b})$.

Furthermore, several Gaussian constraint terms were added to the model to account for experimental systematic sources of error. For the Higgs boson mass measurement, the sample COM energy was being constrained within 2.8 MeV of the nominal COM energy ($\sqrt{s} = 240, 365$ GeV). Also, the Higgs boson mass parameter was constrained by the corresponding mass measurement done at CMS [48]. Finally, the sample signal selection efficiency and the sample integrated luminosity were constraint by 1% and 0.1% around their nominal values respectively. The conservative constraint of the sample integrated luminosity is in accordance with the FCC-ee CDR [19].

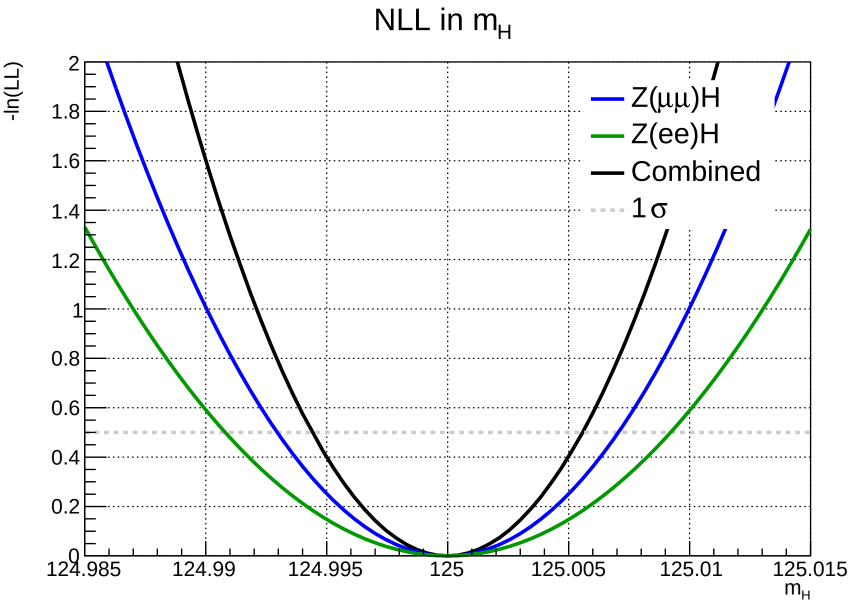


Figure 14: The profile likelihood of the reconstructed Higgs boson mass $m_H$. The contribution of $Z(\mu^+\mu^-)H$ at 240 GeV in blue, $Z(e^+e^-)H$ at 240 GeV is in green and the combined contribution at both energies for all leptonic Z decays in black. The one sigma line is at 0.5.

Starting with a background only fit, the background normalization was fixed for the remainder of the fitting procedure. After that, the full model including the signal PDF $S$ was fitted in the considered recoil mass range ($M_{\text{Rec}} \in [120, 140]$ GeV) for all leptonic ZH channels using RooFit [49]. For each channel, an Asimov dataset [50] containing 100 bins was created based on the post-fit parameters of the full model. When using this particular dataset, we retrieve the true value of the POI (in this case the Higgs boson mass) with respect to the SM expectation (125 GeV, Higgs boson mass in used in the MC samples). Its bins contain the correct number of entries and statistical uncertainties such that the expected value of the POI is realized.

All four Higgs boson mass parameters extracted from the channels were fitted simultaneously to the Asimov datasets. The sensitivity on the Higgs boson mass was determined using the 65% confidence interval found by `MINOS` [51].

Figure 14 shows the profile likelihood of the POI of the combined dataset and the contributions from the channels at $\sqrt{s} = 240$ GeV. The muonic ZH ($Z(\mu^+\mu^-)H$) process at 240 GeV is the most sensitive one since it profits from a very high cross section and an extremely precise reconstruction of the di-muon system. The electronic ZH ($Z(e^+e^-)H$) process at the same energy is slightly less sensitive because of the increased interactions of the electrons with the detector compared to the muons. When increasing the COM energy to 365 GeV the sensitivity on $m_H$ decreases considerably due to the degraded $p_T$ resolution of the drift chamber (see Appendix D.1).

Using the muonic ZH process at 240 GeV, the Higgs boson mass parameter can be constrained to 7.05 MeV around the nominal value of 125 GeV. We get a slightly degraded mass resolution with the electronic ZH process at the same energy (9.20 MeV). At 365 GeV we can constrain the Higgs boson mass to $\mathcal{O}(0.1)$ GeV for both channels (see Fig. 21). This shows again the necessity of the lower energy point for precision Higgs boson mass measurements. Combined the analysis constrains $m_H$ to 5.6 MeV.

## 3.3 Cross section sensitivity

The Higgs boson production cross section is extracted from the expected number of signal events $N_{sig}$ as seen in chapter 3.1, which is completely independent from the shape of the signal or background PDFs. In equation 3.1 the signal strength modifier $\mu_i$ was introduced as the ratio of the observed versus the expected (SM) Higgs boson production cross section. In the following, we assume that the Higgs boson decays as in the SM predicted ($\mu^f := 1$) for both the inclusive and the exclusive processes. A more global approach can be achieved if $\mu^f$ ($\forall\ f \in \{b, c, l\}$) is extracted from e.g. exclusive leptonic ZH processes. On the other hand, such a $\mu^f$ is not extracted in a purely model-independent manner as some dependence is introduced through the jet clustering procedure.

Depending on the considered channel, different signal and background PDF are used. For the leptonic ZH channels at both energy points the same PDFs as in chapter 3.2 were used. Since the hadronic ZH channels, as well as the VBF channels feature non-parametric post-BDT mass distributions for both the signal and background, different models must be used. Because we are only interested in the background normalization, all post-BDT background distributions have been modelled with one-dimensional kernel estimation PDFs [52]. Each datapoint in the background distribution is attributed to a Gaussian kernel, whose width is chosen such that the statistical peculiarities of the dataset are not reflected in the final superposition of Gaussian kernels. For the post-BDT signal distributions, a sum of Gaussian functions (up to five at a time) is used.

Further, the same constraint terms as in the Higgs boson mass analysis are used for the leptonic ZH channels. Recalling that the precision of the Higgs boson mass measurement is degraded in the hadronic ZH and VBF channels, no specific $\sqrt{s}$ or $m_H$ constraint terms are considered.

The background normalization was extracted channel-wise using a background-only fit over the respective mass range. The full model was then fitted to the complete dataset to extract the signal strength modifier and to create an Asimov dataset with $\mu_i = 1$ (SM expectation) for each channel at both energy points. Four datasets are then constructed, which contain the merged Asimov datasets from the 240 GeV ZH, 365 GeV ZH, 365 GeV neutral VBF and 365 GeV charged VBF processes. The motivation behind the use of different signal strength modifiers for VBF is the different final state (neutrinos in charged VBF and electrons in neutral VBF, see Fig. 4).

All four signal strength modifiers are found by a simultaneous fit to the merged Asimov datasets and the sensitivity on these parameters is extracted from `MINOS`. Figure 15 shows the profile likelihood of the full model with respect to the POI in question.

The sensitivity on the signal strength modifier is by construction driven by the number of observed signal events $N_{sig}$. Hence, we expect the highest contribution to the sensitivity on $\mu_i$ coming from channels with the highest cross section (see Fig. 5) such as the hadronic ZH. Looking at Figs.

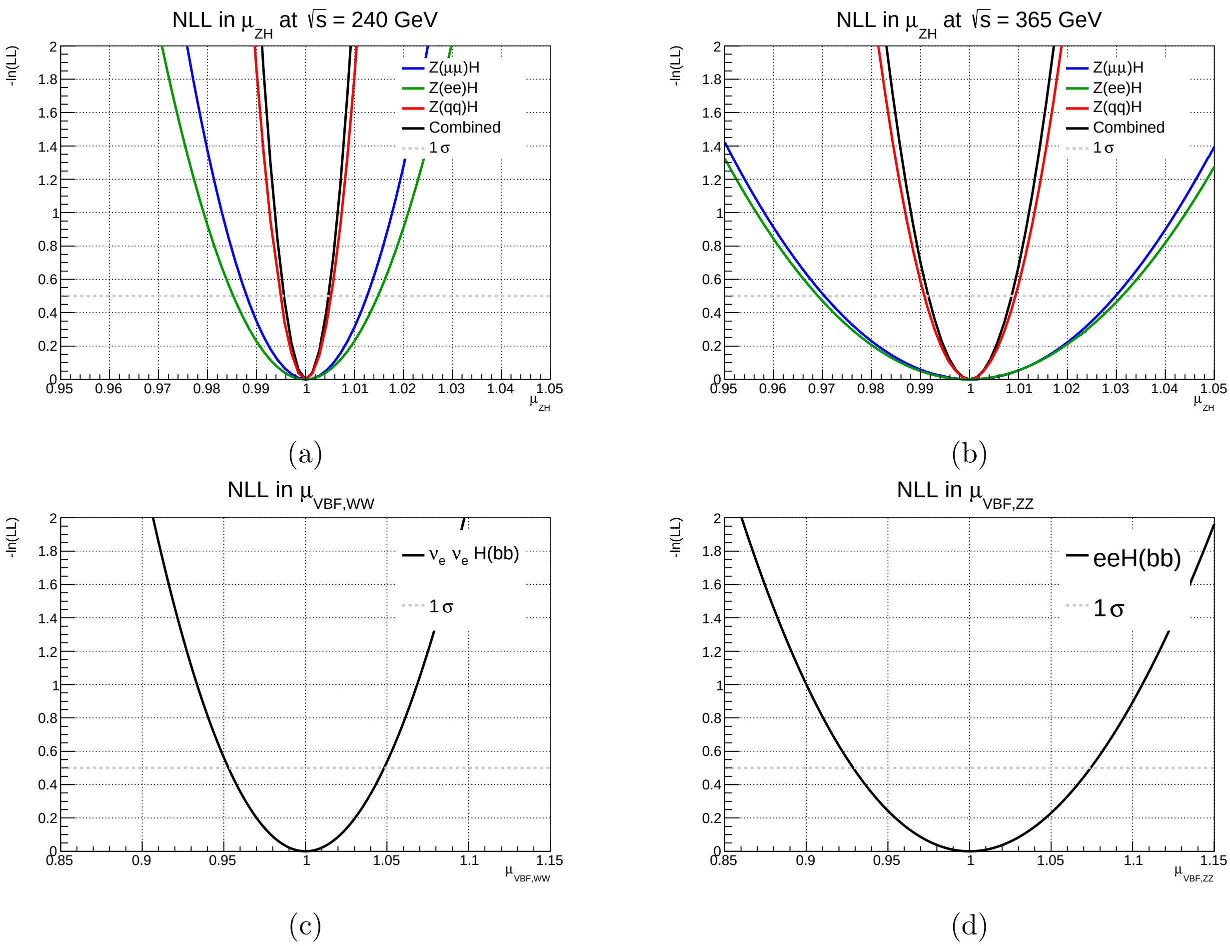


Figure 15: The profile likelihoods of the signal strength modifier $\mu$ for different Higgs boson production processes. (a), (b): The contributions to $\mu_{\mathrm{ZH}}$ from different ZH channels at $\sqrt{s} = 240$ GeV (a) and $\sqrt{s} = 365$ GeV (b). In both cases the hadronic ZH has the highest contribution to the sensitivity. (c): The signal strength modifier $\mu_{\mathrm{VBF,WW}}$ for the charged VBF. (d): The signal strength modifier $\mu_{\mathrm{VBF,ZZ}}$ for the neutral VBF. The one sigma line is at 0.5 in all Figures.

15a and 15b showing the profile likelihood as a function of $\mu_{\mathrm{ZH}}$ at different energies reveal, that indeed the highest contribution comes from the hadronic ZH channels and their large statistics. This relationship between production cross section and sensitivity on $\mu_i$ is also reflected in the other channels. However, we have to recall that the datasets of the hadronic ZH channel heavily depends on the type of jet clustering and its settings, the choice of the input variables of the BDTs as well as its hyperparameters (e.g. number of trees, etc.). The performance of the measurement of $\mu_i$ for various Higgs boson production processes can be found in table 16.

## 3.4 Kappa lambda sensitivity

We can consider the Higgs boson self-coupling $\kappa_\lambda$ after a slight modification of the model used in the previous chapters. The number of observed signal events $N_{sig}$ depends on the signal strength modifier $\mu_i^f$ and on the expected production cross section which is calculated by evaluating the matrix elements of the considered processes. In case of our MC samples, the cross sections were calculated at tree level using either `WHIZARD` or `PYTHIA8` (see tables 18 and 19). We can reparametrize the cross section term appearing in $N_{sig}$ to account also for one-loop and Higgs boson self-energy corrections (see Fig. 16a) at next-to-leading order (NLO). First, the origin of the self-coupling in the SM is discussed and the Kappa framework introduced. After that, the modified cross section is presented together with the fitting model and the final constraints on $\delta\kappa_\lambda$.

| Production process | 68% Confidence Interval |
|---|---|
| ZH at 240 GeV | $\delta\mu_{\mathrm{ZH}} \in [-4.59, 4.59] \cdot 10^{-3}$ |
| ZH at 365 GeV | $\delta\mu_{\mathrm{ZH}} \in [-8.61, 8.59] \cdot 10^{-3}$ |
| charged VBF | $\delta\mu_{\mathrm{VBF,WW}} \in [-4.72, 4.82] \cdot 10^{-2}$ |
| neutral VBF | $\delta\mu_{\mathrm{VBF,ZZ}} \in [-7.13, 7.42] \cdot 10^{-2}$ |

Table 16: The sensitivity on $\mu_i$ of several Higgs boson production processes. If we assume that $\mu_{\mathrm{ZH}}$ is the same for both energy points, we can constrain $\delta\mu_{\mathrm{ZH}} \in [-4.04, 4.09] \cdot 10^{-3}$ at 68% CL.

**Higgs sector in the SM**

In the SM, the Higgs potential is responsible for inducing electroweak symmetry breaking (EWSB, [3]) $SU(2)_L \times U(1)_Y \to U(1)_{\mathrm{elm}}$. Its form is given by renormalizability, and gauge symmetry constraints and it can be written as

$$V^{\mathrm{SM}}(\Phi) = -\mu^2(\Phi^\dagger\Phi) + \lambda(\Phi^\dagger\Phi)^2, \tag{3.4}$$

where $\Phi$ is the Higgs doublet, $\mu^2 = \frac{m_H^2}{2}$ and $\lambda = \frac{m_H^2}{2v^2}$ given in terms of the Higgs mass $m_H$ and the vacuum expectation value (VEV) of the Higgs field $v = 1/\sqrt{\sqrt{2}G_F} \approx 246.22$ GeV [53].

After EWSB, the Higgs potential reduces in the unitary gauge [54, 55] to $V^{\mathrm{SM}}(H) = \frac{m_H^2}{2}H^2 + \lambda v H^3 + \frac{\lambda}{4}H^4$. From the last two terms of the post-EWSB Higgs potential it can be observed that the relation between the dimensionless trilinear and quadrilinear Higgs self-coupling is a constant one, in fact it can be chosen that $\lambda_3^{\mathrm{SM}} = \lambda_4^{\mathrm{SM}} = \lambda$.

If we assume that the SM is the only theory, there should be no measurable difference between the two couplings. However, the determination of the self-couplings is a difficult task since $\lambda$ itself is rather small compared to the $m_H$. Moreover, large energies and high luminosities are generally required as multiple Higgses are involved.

**Kappa framework**

To check the validity of the SM, we can either proceed as in the previous chapters and measure deviations of $\mu_i = 1$ or let certain prefactors in the Higgs potential float to measure the deviations from the predicted SM value. Such tests can be conducted in the $\kappa$ framework [56, 57]. Connecting the observed Higgs cross sections and thus the signal strength modifiers $\mu_i^f$ with the $\kappa$ framework relies on the assumptions of the single narrow resonance the Higgs boson has to pass through as well as the zero width approximation which were already introduced in chapter 3.1. In the $\kappa$ framework the signal strength modifiers read

$$\mu_i^f = \frac{\kappa_i^2 \cdot \kappa_f^2}{\kappa_H^2}, \tag{3.5}$$

where $\kappa_H^2$ corrects the SM value of $\Gamma_H$ to take into account the modifications introduced by $\kappa_i$.

Apart from cross sections and the modification of Higgs boson coupling strengths, we can consider modifications of the Higgs potential $V^{\mathrm{SM}}(H)$. Currently our knowledge of the Higgs sector restricts itself on the first term, but determining the exact shape of the Higgs potential promises vast implications on BSM and cosmology [58]. In addition, the Higgs potential is connected to the natural problem and determines the stability of the electroweak vacuum [59]. It is hence worthwhile to explore the Higgs sector beyond the SM and thus motivates undertaking the estimation of the precision reach at the next circular collider.

We can extend the idea of the $\kappa$ framework on the third and fourth order self-couplings of the Higgs potential and introduce two new variables $\kappa_3$ and $\kappa_4$ which parametrize the deviation of the measured self-couplings with respect to the SM prediction: $\kappa_i := \lambda_i/\lambda_i^{\mathrm{SM}}$. The Higgs boson trilinear self-coupling $\kappa_3$ can be measured at the LHC as well as the HL-LHC through di-Higgs production [60, 61]. The precision of these direct measurements ($\mathcal{O}(10)$ for LHC and $\mathcal{O}(1)$ for HL-LHC) are degraded due to other di-Higgs production channels which interfere. At circular lepton colliders such as the FCC-ee the di-Higgs production threshold is reachable as well, however the cross section for a di-Higgs production is too small such that statistically significant quantities can be collected [62]. Even for FCC-hh with $\sqrt{s} = 100$ TeV, extracting the quadrilinear Higgs boson self-coupling remains difficult but strategies exist to measure this coupling with a significance larger than 3 $\sigma$ [63].

At FCC-ee the trilinear Higgs boson self-coupling can be accessed indirectly through one-loop corrections of the single-Higgs processes. In the following, we look at the one-loop corrections to Higgsstrahlung, as well as charged and neutral VBF. With the large luminosity obtained at the two energy points of the FCC-ee and the accurate measurement of the Higgs boson production cross section through $\mu_i$, sub-percentage precision on $\delta\kappa_\lambda := \kappa_\lambda - 1$ is expected.

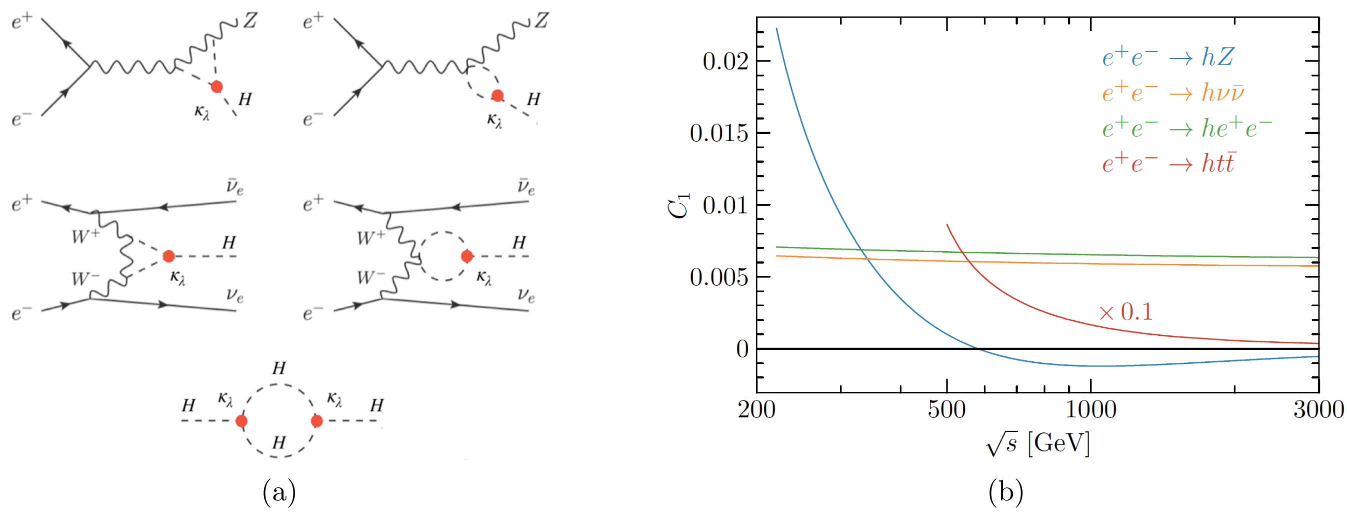


Figure 16: (a): One-loop corrections of the considered ZH and VBF processes with $\kappa_\lambda$ and the self-energy diagram. (b): Coefficient $C_1$ for different Higgs boson production processes as a function of $\sqrt{s}$ [64].

Starting from the amplitudes in Fig. 16a, we can parametrize the NLO production cross section of the single-Higgs channels

$$\sigma_{\mathrm{i,NLO}} = Z_H \sigma_{\mathrm{i,LO}} (1 + \kappa_\lambda C_{1,i}), \tag{3.6}$$

where $\sigma_{\mathrm{i,LO}}$ corresponds to the leading order production cross section of the process $i$. The coefficient $C_{1,i}$ depends on the process $i$ as well as on $\sqrt{s}$ (see Fig. 16b) and it emerges from the interference between the one-loop diagrams linear in $\sqrt{\kappa_\lambda}$ and the tree level diagrams [65]. Finally, $Z_H$ is a universal resummed wave-function renormalization which depends on $\kappa_\lambda$ as follows

$$Z_H = \frac{1}{1 - \kappa_\lambda^2 \delta Z_H}, \tag{3.7}$$

where $\delta Z_H = -\frac{9}{16}\frac{G_F m_H^2}{\sqrt{2}\pi^2}\left(\frac{2\pi}{3\sqrt{3}} - 1\right) \approx -0.00154$.

Within the $\kappa$ framework, we can also consider deviations from the Higgs boson couplings to the vector bosons $\kappa_{HZZ}$ and $\kappa_{HWW}$. Using equation 3.5 together with 3.1, the NLO cross section is modified $\sigma_{\text{i,NLO}} \rightarrow \sigma_{\text{i,NLO}} \cdot \kappa_i^2$.

### Fitting model and constraints

In order to extract the precision of $\kappa_\lambda$ per Higgs boson production channel, the parametrization of $N_{sig}$ has been modified to incorporate the NLO cross section as a function of $\kappa_\lambda$. Since the shape of the signal and background PDF is not depending on the production cross section, the same PDFs as in the estimation of $\mu_i$ are used. Apart from the constraints on the integrated luminosity and the signal selection efficiency, the current constraint on $\delta\kappa_\lambda$ from di-Higgs production processes made by the LHC has been included as well [61].

The fitting procedure for the individual channels is identical to chapter 3.3: First, the background normalization was fixed after a background only fit. After fitting the full model to the respective datasets, an Asimov dataset with $\delta\kappa_\lambda := 0$ and $\mu_i := 1$ was created for each channel $i$. Subsequently, the parameter of interest $\delta\kappa_\lambda$ is simultaneously fitted to the combined Asimov dataset and the profile likelihood is extracted leaving only $\delta\kappa_\lambda$ floating (see Fig. 17).

From there, we explored three different scenarios. The highest precision on $\delta\kappa_\lambda$ was achieved by leaving only itself floating in the simultaneous fit (1D). This scenario is very optimistic, as all the other POI have to be fixed to their SM value and thus restricting the appearance of NP coming from these parameters. The situation changes considerably if we let multiple POI float as well. In the following, each of these cases are examined in more detail.

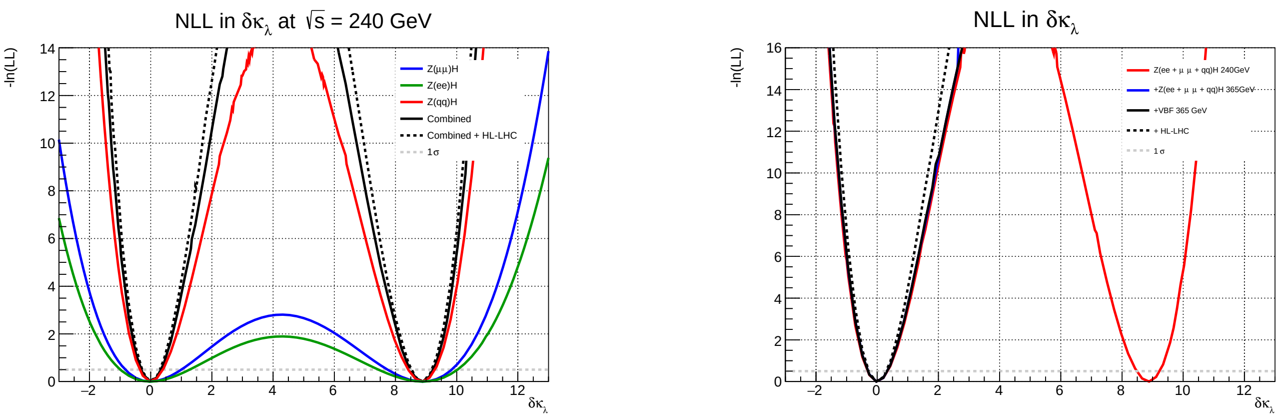


(a) (b)

Figure 17: (a): Profile likelihood of Higgsstrahlung processes at 240 GeV. The degeneracy around $\delta\kappa_\lambda \approx 9$ is introduced by the wave-function renormalization $Z_H$ (eq. 3.7). (b): The combined analysis with ZH and VBF at both energies. The degeneracy is lifted after introducing the ZH channel at 365 GeV.

### One-dimensional fit

In this scenario, only $\delta\kappa_\lambda$ was fitted simultaneously and we set $\mu_i := 1$ for all processes $i$. The profile likelihood scan of all ZH channels at $\sqrt{s} = 240$ GeV can be seen in Fig. 17a. As it is the case with $\mu_i$, the precision reach of $\delta\kappa_\lambda$ is driven by the number of observed signal events $N_{sig}$. This is reflected in the fact that the hadronic ZH process constrain the value of $\delta\kappa_\lambda$ much better than their leptonic counterparts. The second minimum of $\delta\kappa_\lambda$ around 9 is due to the Higgs boson self-energy (bottommost diagram of Fig. 16a) introducing a quadratic correction in $\kappa_\lambda$. This degeneracy is expected to be lifted when including processes at $\sqrt{s} = 365$ GeV and exploiting the energy dependence of the interference term $C_{1,i}$. Figure 25 shows the profile likelihood scans of the individual channels and an absence of the degeneracy at processes with $\sqrt{s} = 365$ GeV. However, due to the reduced cross section of the Higgsstrahlung compared to 240 GeV and the small number of VBF signal events, the overall precision on $\delta\kappa_\lambda$ is diminished. On the other hand, if all channels are combined the degeneracy is lifted and $\delta\kappa_\lambda$ is well constrained around the first minimum in the interval $[-0.36, 0.40]$ at 68% CL (see Fig. 17b). Adding the expected HL-LHC measurement to the analysis, the interval can be further narrowed down to $[-0.29, 0.31]$ at 68% CL. This underlines the importance of including processes at 365 GeV, despite their worse resolution and fewer events (excluding VBF).

### Two-dimensional fit

A more realistic scenario can be considered, if two POI are left as floating parameters in the fit. We conducted two different studies with this assumption in mind. The first study is made with $\delta\kappa_\lambda$ and $\delta\kappa_{\mathrm{HZZ}} := \kappa_{\mathrm{HZZ}} - 1$, where $\kappa_{\mathrm{HZZ}}$ is the coupling of the Higgs to Z bosons. The second study is made with $\delta\kappa_\lambda$ and $\mu_{\mathrm{ZH}}$ supposing that $\mu_{\mathrm{ZH}}$ is the same for the two energies.

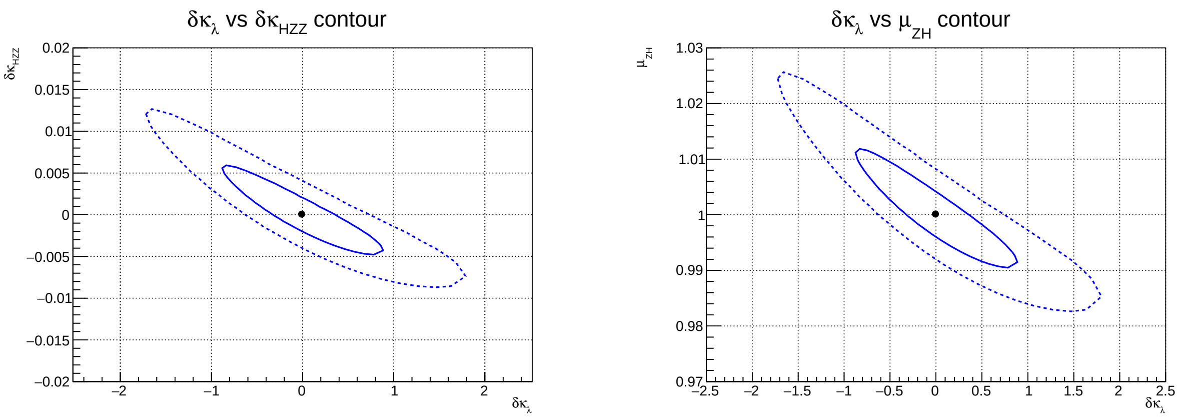


(a) (b)

Figure 18: (a): The NLL contour of $\delta\kappa_\lambda$ (x axis) and $\delta\kappa_{\mathrm{HZZ}}$ (y axis) involving all ZH and VBF at both energies and no HL-LHC constraint. The solid blue line represents the contour at 68% CL and the dashed blue line represents the contour at 95% CL. The black dot is corresponding to the SM expectation of the two POI. (b): The NLL contour of $\delta\kappa_\lambda$ (x axis) and $\mu_{\mathrm{ZH}}$ (y axis) involving all ZH and VBF at both energies and no HL-LHC constraint. The values of $\mu_{\mathrm{VBF,WW}}$ and $\mu_{\mathrm{VBF,ZZ}}$ are fixed to unity.

Leaving only $\delta\kappa_\lambda$ and $\delta\kappa_{\mathrm{HZZ}}$ floating increases the positive and negative error interval around the SM value $\delta\kappa_\lambda = 0$ by approximately a factor of 2.4 and 2.6.

Figure 18a shows the contours in $\delta\kappa_\lambda$ and $\delta\kappa_{\mathrm{HZZ}}$ both at 68% (solid blue line) and 95% (dashed blue line) CL without the constraints from HL-LHC, while the black dot represents the SM expectation. We notice that the two POI are anti-correlated, which is due to the fact that in the $\kappa$ framework the substitution $\sigma_{\mathrm{i,NLO}} \to \sigma_{\mathrm{i,NLO}} \cdot \kappa_i^2$ has to be made.

For the second study we considered $\delta\kappa_\lambda$ and $\mu_{\mathrm{ZH}}$ floating in the fit. That decreases the precision on $\delta\kappa_\lambda$ similarly with respect to the first study and also spoils the sensitivity on $\mu_{\mathrm{ZH}}$ by increasing the negative and positive boundary of the confidence interval at 68% CL by a factor of 2.4 and 2.9. Here are the POI anti-correlated as well (see Fig. 18b), because in the equation of $N_{sig}$ $\mu_{\mathrm{ZH}}$ is multiplied directly with the NLO cross section which contains $\kappa_\lambda$ at first order.

### Four-dimensional fit

The most general case we considered is, when we leave four POI floating in the simultaneous fit ($\delta\kappa_\lambda$, $\mu_{\rm ZH}$, $\mu_{\rm VBF,WW}$ and $\mu_{\rm VBF,ZZ}$), while assuming $\mu_f := 1$ for all channels including VBF. Since the VBF channels contribution to the sensitivity of $\delta\kappa_\lambda$ is subdominant compared to the Higgsstrahlung, the degradation of the precision reach of $\delta\kappa_\lambda$ is limited. The impact on the performance on the measurement of $\delta\kappa_\lambda$ compared to the two-dimensional fit is thus negligible (see Fig. 19).

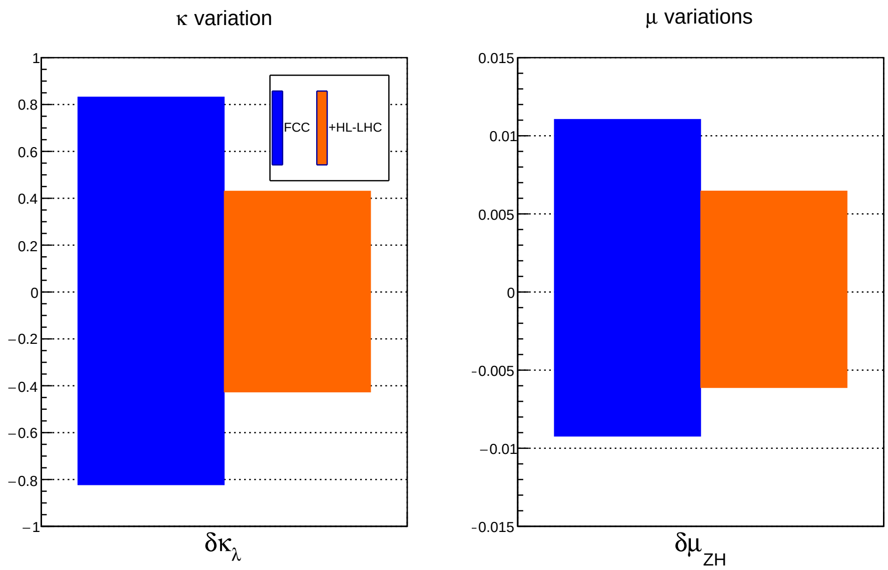


(a)

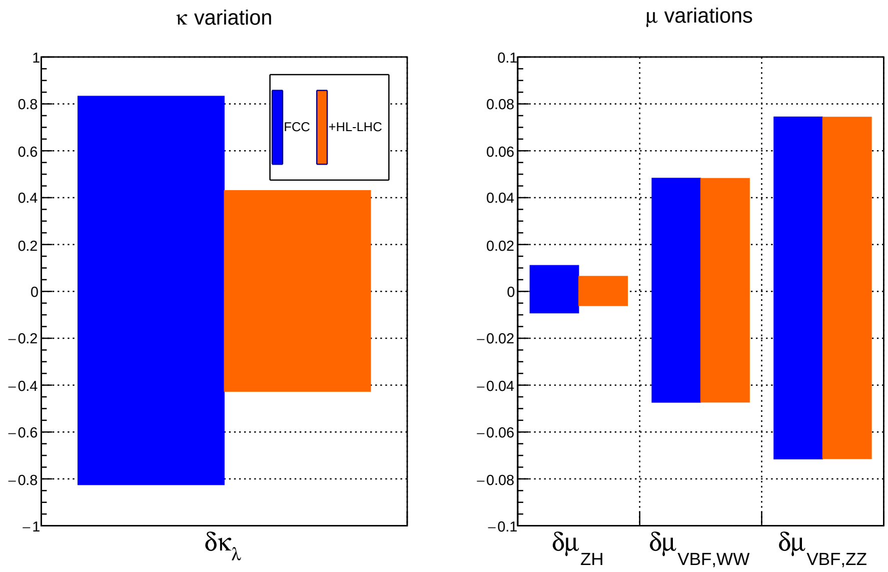


(b)

Figure 19: (a): The variations from $\kappa_\lambda$ and $\mu_{\rm ZH}$ when leaving them floating in the 2D fit without (blue) and with (orange) constraints from HL-LHC. We assumed that $\mu_{\rm ZH}$ is the same at 240 GeV and 365 GeV. (b): Situation for the 4D case.

# 4 Conclusion and outlook

The purpose of this work was to show how well future lepton colliders, namely the FCC-ee, can be used to test the Standard Model Higgs sector. It improved and expanded the previous analysis [43] by adding the hadronic Higgsstrahlung at both energy points as well as the leptonic Higgsstrahlung at 365 GeV. Furthermore, it featured the inclusion of more background channels especially at 365 GeV, a new orthogonal categorization of events and the usage of Monte Carlo samples which included both initial as well as final state radiation.

We considered three main observables related to the Higgs sector which can be measured to high precision at the FCC-ee. The Higgs boson mass $m_H$ can be constrained at the FCC-ee using leptonic Higgsstrahlung using both energy points by measuring the invariant mass of the system recoiling to the $Z$ to 5.6 MeV around the nominal value of 125 GeV. This analysis incorporated experimental systematic uncertainties such as fluctuations of the COM energy, the measured integrated luminosity and the signal selection efficiency which influence the ultimate precision of the Higgs boson mass measurement. Other sources of systematic uncertainties coming from e.g ISR, FSR, lepton momentum scale or the jet energy scale are not treated, because it would be beyond the scope of this work.

The second observable is the Higgs boson production cross section of leptonic and hadronic Higgsstrahlung and VBF. The performance of measuring this parameter was evaluated by using the signal strength modifiers $\mu_i^f$, while assuming that the observed Higgs boson branching ratios follow the SM prediction. We showed that when including the hadronic ZH processes, the FCC-ee would be capable to constrain $\mu_{\mathrm{ZH}}$ with sub-percent precision. The VBF signal strength modifiers $\mu_{\mathrm{VBF,ZZ}}$ and $\mu_{\mathrm{VBF,WW}}$ are far less constraint ($\mathcal{O}(0.1)$) due to their small number of signal events. A more realistic estimate of the precision reach of $\mu_i$ is expected, if the assumption $\mu^f := 1$ is dropped and, for the hadronic ZH only, the BDTs are trained on datasets which feature a priori anti-ISR selection cuts. Apart from that, the jet tagging algorithm currently in use can be improved with ParticleNet [66], which represents the jet as a particle cloud and uses deep learning techniques to extract the jet flavor.

Lastly, we looked at the Higgs boson trilinear self-coupling $\kappa_\lambda$ as well as the precision of measuring possible deviations of the Higgs boson coupling to vector bosons $\delta\kappa_{HZZ}$ and $\delta\kappa_{HWW}$. Taking into account one-loop corrections of the ZH and VBF Feynman diagrams as well as self-energy corrections, the NLO cross sections as a function of $\kappa_\lambda$, $\kappa_{HZZ}$ and $\kappa_{HWW}$ were computed. Due to the quadratic correction on the NLO cross section introduced by the renormalization factor $Z_H$, the NLL of $\delta\kappa_\lambda$ has a second minimum at around 9 which is lifted well beyond the 5 $\sigma$ threshold when including inclusive ZH and exclusive VBF at 365 GeV. In this one-dimensional case, the FCC together with measurements from HL-LHC can constrain $\delta\kappa_\lambda$ by the end of the 365 GeV run within [-0.29, 0.31] at 68% CL. The precision on the measurement of $\kappa_\lambda$ will decrease if two or more POI are left floating in the fit. We showed, that for $\delta\kappa_\lambda$ the boundaries (negative, positive) of the confidence interval at 68% CL increases by approximately a factor of 2.4 and 2.6 respectively. For $\mu_{\mathrm{ZH}}$ the negative and positive boundaries of the confidence interval at 68% CL increase by a factor of 2.4 and 2.9 thus spoiling the precision on this parameter as well.

More global scenarios can be probed, if also Higgs boson couplings to fermions are included. In the $\kappa$ framework, additional couplings can be added through the replacement $\sigma_{\mathrm{i,NLO}} \to \sigma_{\mathrm{i,NLO}} \cdot \bar{\kappa_f}^2$ where $\bar{\kappa_f} := \kappa_f/\kappa_H$. Also, the currently used MC samples feature a Delphes fast-simulation. In order to draw a comparison to LHC or other electron-positron colliders (e.g. ILC, CEPC) the IDEA detector has to be fully modelled. Furthermore, additional sources of systematic uncertainties (ISR/FSR, momentum scale variations, etc.) have to be considered as well. In summary, the present analysis gives a promising estimate of the very rich Higgs boson physics potential of the FCC-ee and the road in this direction should be continued.

# References


[1] S. Chatrchyan et al. “Observation of a new boson at a mass of 125 GeV with the CMS experiment at the LHC”. In: *Physics Letters B* 716.1 (2012), pp. 30–61. ISSN: 0370-2693. DOI: https://doi.org/10.1016/j.physletb.2012.08.021. URL: https://www.sciencedirect.com/science/article/pii/S0370269312008581.

[2] G. Aad et al. “Observation of a new particle in the search for the Standard Model Higgs boson with the ATLAS detector at the LHC”. In: *Physics Letters B* 716.1 (2012), pp. 1–29. ISSN: 0370-2693. DOI: https://doi.org/10.1016/j.physletb.2012.08.020. URL: https://www.sciencedirect.com/science/article/pii/S037026931200857X.

[3] M. Spira and P. M. Zerwas. “Electroweak symmetry breaking and Higgs physics”. In: *Lecture Notes in Physics*. Springer Berlin Heidelberg, pp. 161–225. DOI: 10.1007/bfb0106895. URL: https://doi.org/10.1007%2Fbfb0106895.

[4] G. Altarelli. *The Higgs and the Excessive Success of the Standard Model*. 2014. DOI: 10.48550/ARXIV.1407.2122. URL: https://arxiv.org/abs/1407.2122.

[5] R. Foot et al. “Charge quantization in the Standard Model and some of its extensions”. In: *Modern Physics Letters A* 05.32 (1990), pp. 2721–2731. DOI: 10.1142/S0217732390003176. eprint: https://doi.org/10.1142/S0217732390003176. URL: https://doi.org/10.1142/S0217732390003176.

[6] R. Barbieri. *Ten Lectures on the ElectroWeak Interactions*. 2007. DOI: 10.48550/ARXIV.0706.0684. URL: https://arxiv.org/abs/0706.0684.

[7] G. C. Branco et al. “Theory and phenomenology of two-Higgs-doublet models”. In: *Physics Reports* 516.1-2 (2012), pp. 1–102. DOI: 10.1016/j.physrep.2012.02.002. URL: https://doi.org/10.1016%2Fj.physrep.2012.02.002.

[8] V. Keus, S. F. King, and S. Moretti. “Three-Higgs-doublet models: symmetries, potentials and Higgs boson masses”. In: *Journal of High Energy Physics* 2014.1 (2014), p. 52. DOI: 10.1007/JHEP01(2014)052. URL: https://doi.org/10.1007/JHEP01(2014)052.

[9] F. Maltoni, D. Pagani, and X. Zhao. “Constraining the Higgs self-couplings at $e^+e^-$ colliders”. In: *Journal of High Energy Physics* 2018.7 (2018). DOI: 10.1007/jhep07(2018)087. URL: https://doi.org/10.1007%2Fjhep07%282018%29087.

[10] F. Boudjema and E. Chopin. “Double Higgs production at the linear colliders and the probing of the Higgs selfcoupling”. In: *Z. Phys. C* 73 (1996), pp. 85–110. DOI: 10.1007/s002880050298. arXiv: hep-ph/9507396.

[11] LHCb Collaboration et al. *Test of lepton universality in beauty-quark decays*. 2021. DOI: 10.48550/ARXIV.2103.11769. URL: https://arxiv.org/abs/2103.11769.

[12] R. Aaij et al. “Measurement of the Ratio of Branching Fractions $\mathcal{B}(\overline{B}^0 \to D^{*+}\tau^-\overline{\nu}_\tau)/\mathcal{B}(\overline{B}^0 \to D^{*+}\mu^-\overline{\nu}_\mu)$”. In: *Phys. Rev. Lett.* 115 (11 2015), p. 111803. DOI: 10.1103/PhysRevLett.115.111803. URL: https://link.aps.org/doi/10.1103/PhysRevLett.115.111803.

[13] O. Aberle et al. *High-Luminosity Large Hadron Collider (HL-LHC): Technical design report.* CERN Yellow Reports: Monographs. Geneva: CERN, 2020.

[14] A. Dainese et al. *Report on the Physics at the HL-LHC, and Perspectives for the HE-LHC.* Tech. rep. Geneva, Switzerland, 2019. DOI: 10.23731/CYRM-2019-007. URL: https://cds.cern.ch/record/2703572.

[15] G. Aad et al. "Determination of the parton distribution functions of the proton from ATLAS measurements of differential $W^{\pm}$and Z boson production in association with jets". In: *Journal of High Energy Physics* 2021.7 (2021), p. 223. DOI: 10.1007/JHEP07(2021)223. URL: https://doi.org/10.1007/JHEP07(2021)223.

[16] V. Khachatryan et al. "Constraints on parton distribution functions and extraction of the strong coupling constant from the inclusive jet cross section in pp collisions at $\sqrt{s} = 7$ TeV". In: *The European Physical Journal C* 75.6 (2015), p. 288. DOI: 10.1140/epjc/s10052-015-3499-1. URL: https://doi.org/10.1140/epjc/s10052-015-3499-1.

[17] European Strategy Group. *2020 Update of the European Streategy for Particle Physics.* 2020. URL: https://home.cern/sites/default/files/2020-06/2020%20Update%20European%20Strategy.pdf.

[18] M. Mangano et al. *FCC Physics Opportunities: Future Circular Collider Conceptual Design Report Volume 1. Future Circular Collider.* Tech. rep. Geneva: CERN, 2018. DOI: 10.1140/epjc/s10052-019-6904-3. URL: https://cds.cern.ch/record/2651294.

[19] M. Benedikt et al. *FCC-ee: The Lepton Collider: Future Circular Collider Conceptual Design Report Volume 2. Future Circular Collider.* Tech. rep. Geneva: CERN, 2018. DOI: 10.1140/epjst/e2019-900045-4. URL: https://cds.cern.ch/record/2651299.

[20] M. Benedikt et al. *FCC-hh: The Hadron Collider: Future Circular Collider Conceptual Design Report Volume 3. Future Circular Collider.* Tech. rep. Geneva: CERN, 2018. DOI: 10.1140/epjst/e2019-900087-0. URL: https://cds.cern.ch/record/2651300.

[21] I. Agapov et al. *Future Circular Lepton Collider FCC-ee: Overview and Status.* 2022. DOI: 10.48550/ARXIV.2203.08310. URL: https://arxiv.org/abs/2203.08310.

[22] M. Benedikt. *FCC Feasibility Study Overview.* FCC Week 2022. 2022.

[23] D. Shatilov. "Beam-beam effects at High Energy $e^+e^-$ colliders". In: *62nd ICFA Advanced Beam Dynamics Workshop on High Luminosity Circular ee Colliders.* 2019, TUYBA02. DOI: 10.18429/JACoW-eeFACT2018-TUYBA02.

[24] R Turchetta et al. "A monolithic active pixel sensor for charged particle tracking and imaging using standard VLSI CMOS technology". In: *Nuclear Instruments and Methods in Physics Research Section A: Accelerators, Spectrometers, Detectors and Associated Equipment* 458.3 (2001), pp. 677–689. ISSN: 0168-9002. DOI: https://doi.org/10.1016/S0168-9002(00)00893-7. URL: https://www.sciencedirect.com/science/article/pii/S0168900200008937.

[25] M. Poli Lener et al. "The mu-RWELL: A compact, spark protected, single amplification-stage MPGD". In: *Nuclear Instruments and Methods in Physics Research Section A Accelerators*

*Spectrometers Detectors and Associated Equipment* 824 (July 2016), pp. 565–568. DOI: 10.1016/j.nima.2015.11.098.

[26] M. Antonello. "IDEA: A detector concept for future leptonic colliders". In: *Nuovo Cim. C* 43.2-3 (2020). Ed. by G. D'Ambrosio and G. De Nardo, p. 27. DOI: 10.1393/ncc/i2020-20027-2.

[27] J. de Favereau et al. "DELPHES 3: a modular framework for fast simulation of a generic collider experiment". In: *Journal of High Energy Physics* 2014.2 (2014). DOI: 10.1007/jhep02(2014)057. URL: https://doi.org/10.1007%2Fjhep02%282014%29057.

[28] W. Kilian, M. Kraemer, and P. M. Zerwas. "Higgs-strahlung and WW fusion in $e^+e^-$ collisions". In: *Physics Letters B* 373.1-3 (1996), pp. 135–140. DOI: 10.1016/0370-2693(96)00100-1. URL: https://doi.org/10.1016%2F0370-2693%2896%2900100-1.

[29] B.A. Kniehl. "Radiative corrections for associated ZH production at future $e^+e^-$ colliders". In: *Z. Phys. C Particles and Fields* 55 (1992), pp. 605–618. DOI: https://doi.org/10.1007/BF01561297.

[30] Z.-X. Chen et al. "Cross section and Higgs mass measurement with Higgsstrahlung at the CEPC". In: *Chinese Physics C* 41 (Feb. 2017), p. 023003. DOI: 10.1088/1674-1137/41/2/023003.

[31] X. Mo et al. "Physics cross sections and event generation of $\mathrm{e^+e^-}$ annihilations at the CEPC". In: *Chinese Physics C* 40.3 (2016), p. 033001. DOI: 10.1088/1674-1137/40/3/033001. URL: https://doi.org/10.1088/1674-1137/40/3/033001.

[32] A. Djouadi, J. Kalinowski, and P.M. Zerwas. "Higgs radiation off top quarks in high-energy $e^+e^-$ colliders". In: *Z. Phys. C Particles and Fields* 54 (1992), pp. 255–262.

[33] *Delphes FCCee Physics events spring 2021 production*. 2022. URL: http://fcc-physics-events.web.cern.ch/fcc-physics-events/Delphesevents_spring2021_IDEA.php.

[34] W. Kilian, T. Ohl, and J. Reuter. "WHIZARD—simulating multi-particle processes at LHC and ILC". In: *The European Physical Journal C* 71.9 (2011). DOI: 10.1140/epjc/s10052-011-1742-y. URL: https://doi.org/10.1140%2Fepjc%2Fs10052-011-1742-y.

[35] M. Moretti, T. Ohl, and J. Reuter. "O'Mega: An Optimizing Matrix Element Generator". In: (2001). DOI: 10.48550/ARXIV.HEP-PH/0102195. URL: https://arxiv.org/abs/hep-ph/0102195.

[36] C. Bierlich et al. "A comprehensive guide to the physics and usage of PYTHIA 8.3". In: (2022). DOI: 10.48550/ARXIV.2203.11601. URL: https://arxiv.org/abs/2203.11601.

[37] *FCCAnalyses Github repository*. 2022. URL: https://github.com/HEP-FCC/FCCAnalyses.

[38] J. Eysermans et al. *Higgs mass and cross-section studies using ZH recoil with $Z \to \mu^+\mu^-$*. 2021. URL: https://indico.cern.ch/event/995850/contributions/4415989/attachments/2272945/3860610/ZHRecoilAnalysis_FCCWeek_29062021.pdf.

[39] P. Azzi et al. “Higgs and top physics reconstruction challenges and opportunities at FCC-ee”. In: *The European Physical Journal Plus* 137.1 (2021), p. 39. DOI: 10.1140/epjp/s13360-021-02223-z. URL: https://doi.org/10.1140/epjp/s13360-021-02223-z.

[40] M. Cacciari, G. Salam, and G. Soyez. “FastJet user manual”. In: *The European Physical Journal C* 72.3 (2012). DOI: 10.1140/epjc/s10052-012-1896-2. URL: https://doi.org/10.1140%2Fepjc%2Fs10052-012-1896-2.

[41] R. Brun and F. Rademakers. “ROOT - An Object Oriented Data Analysis Framework”. In: *AIHENP’96 Workshop, Lausane*. Vol. 389. 1996, pp. 81–86.

[42] A. Hoecker et al. “TMVA: Toolkit for Multivariate Data Analysis”. In: *PoS* ACAT (2007), p. 040. arXiv: physics/0703039.

[43] C. T. Cazzaniga. “Exploring the precision frontier on the Higgs boson properties at the FCC-ee”. MA thesis. Ecole Polytechnique - ETH Zurich, 2021.

[44] L. Breiman et al. *Classification And Regression Trees*. 1st ed. Routledge, 1984. DOI: https://doi.org/10.1201/9781315139470.

[45] M. A. Thomson. “Model-Independent Measurement of the $e^+e^- \to$ HZ Cross Section at a Future $e^+e^-$ Linear Collider using Hadronic Z Decays”. In: *The European Physical Journal C* 76.2 (2016). DOI: 10.1140/epjc/s10052-016-3911-5. URL: https://doi.org/10.1140%2Fepjc%2Fs10052-016-3911-5.

[46] R. Nicolaidou and Y. Sirois. “The Higgs boson discovery and measurements”. In: *Comptes Rendus Physique* 16.4 (2015). Highlights of the LHC run 1 / Résultats marquants de la première période d’exploitation du GCH, pp. 379–393. ISSN: 1631-0705. DOI: https://doi.org/10.1016/j.crhy.2015.03.015. URL: https://www.sciencedirect.com/science/article/pii/S1631070515000663.

[47] K. Cranmer. “Practical Statistics for the LHC”. In: (2015). DOI: 10.48550/ARXIV.1503.07622. URL: https://arxiv.org/abs/1503.07622.

[48] A. M. Sirunyan et al. “A measurement of the Higgs boson mass in the diphoton decay channel”. In: *Physics Letters B* 805 (2020), p. 135425. DOI: 10.1016/j.physletb.2020.135425. URL: https://doi.org/10.1016%2Fj.physletb.2020.135425.

[49] W. Verkerke and D. P. Kirkby. “The RooFit toolkit for data modeling”. In: *eConf* C0303241 (2003). Ed. by L. Lyons and Muge Karagoz, MOLT007. arXiv: physics/0306116.

[50] G. Cowan et al. “Asymptotic formulae for likelihood-based tests of new physics”. In: *Eur. Phys. J. C* 71.1554 (2011). URL: https://doi.org/10.1140/epjc/s10052-011-1554-0.

[51] F. James and M. Roos. “Minuit: A System for Function Minimization and Analysis of the Parameter Errors and Correlations”. In: *Comput. Phys. Commun.* 10 (1975), pp. 343–367. DOI: 10.1016/0010-4655(75)90039-9.

[52] K. Cranmer. “Kernel estimation in high-energy physics”. In: *Computer Physics Communications* 136.3 (2001), pp. 198–207. DOI: 10.1016/s0010-4655(00)00243-5. URL: https://doi.org/10.1016%2Fs0010-4655%2800%2900243-5.

[53] C. Amsler, M. Doser, and M. Antonelli. “Review of particle physics”. eng. In: *Physics Letters B* 667.1-5 (2008), 1–1340. ISSN: 0370-2693. URL: {http://dx.doi.org/10.1016/j.physletb.2008.07.018}.

[54] S. Weinberg. “Physical Processes in a Convergent Theory of the Weak and Electromagnetic Interactions”. In: *Phys. Rev. Lett.* 27 (24 1971), pp. 1688–1691. DOI: 10.1103/PhysRevLett.27.1688. URL: https://link.aps.org/doi/10.1103/PhysRevLett.27.1688.

[55] S. Weinberg. “General Theory of Broken Local Symmetries”. In: *Phys. Rev. D* 7 (4 1973), pp. 1068–1082. DOI: 10.1103/PhysRevD.7.1068. URL: https://link.aps.org/doi/10.1103/PhysRevD.7.1068.

[56] LHC Higgs Cross Section Working Group et al. *LHC HXSWG interim recommendations to explore the coupling structure of a Higgs-like particle*. 2012. DOI: 10.48550/ARXIV.1209.0040. URL: https://arxiv.org/abs/1209.0040.

[57] C. T. Potter et al. *Handbook of LHC Higgs Cross Sections: 3. Higgs Properties: Report of the LHC Higgs Cross Section Working Group*. en. 2013. DOI: 10.5170/CERN-2013-004. URL: http://cds.cern.ch/record/1559921.

[58] S. D. Bass, A. De Roeck, and M. Kado. “The Higgs boson implications and prospects for future discoveries”. In: *Nature Reviews Physics* 3.9 (2021), pp. 608–624. DOI: 10.1038/s42254-021-00341-2. URL: https://doi.org/10.1038/s42254-021-00341-2.

[59] A. Blondel and P. Janot. *Future strategies for the discovery and the precise measurement of the Higgs self coupling*. 2018. DOI: 10.48550/ARXIV.1809.10041. URL: https://arxiv.org/abs/1809.10041.

[60] M. Cepeda et al. *Higgs Physics at the HL-LHC and HE-LHC*. 2019. DOI: 10.48550/ARXIV.1902.00134. URL: https://arxiv.org/abs/1902.00134.

[61] F. Maltoni et al. “Trilinear Higgs coupling determination via single-Higgs differential measurements at the LHC”. In: *The European Physical Journal C* 77.12 (2017), p. 887. DOI: 10.1140/epjc/s10052-017-5410-8. URL: https://doi.org/10.1140/epjc/s10052-017-5410-8.

[62] Abramowicz, H. et al. “Higgs physics at the CLIC electron-positron linear collider”. In: *Eur. Phys. J. C* 77.7 (2017), p. 475. DOI: 10.1140/epjc/s10052-017-4968-5. URL: https://doi.org/10.1140/epjc/s10052-017-4968-5.

[63] B. Fuks, J. H. Kim, and S. J. Lee. “Scrutinizing the Higgs quartic coupling at a future 100 TeV proton-proton collider with taus and b-jets”. In: *Physics Letters B* 771 (2017), pp. 354–358. DOI: 10.1016/j.physletb.2017.05.075. URL: https://doi.org/10.1016%2Fj.physletb.2017.05.075.

[64] S. Di Vita et al. “A global view on the Higgs self-coupling at lepton colliders”. In: *Journal of High Energy Physics* 2018.2 (2018). ISSN: 1029-8479. DOI: 10.1007/jhep02(2018)178. URL: http://dx.doi.org/10.1007/JHEP02(2018)178.

[65] G. Degrassi et al. “Probing the Higgs self coupling via single Higgs production at the LHC”. In: *JHEP* 12 (2016), p. 080. DOI: 10.1007/JHEP12(2016)080. arXiv: 1607.04251 [hep-ph].

[66] H. Qu and L. Gouskos. “Jet tagging via particle clouds”. In: *Physical Review D* 101.5 (2020). DOI: 10.1103/physrevd.101.056019. URL: https://doi.org/10.1103%2Fphysrevd.101.056019.

# A Categorization of events

## A.1 Categorization of events at 240 GeV

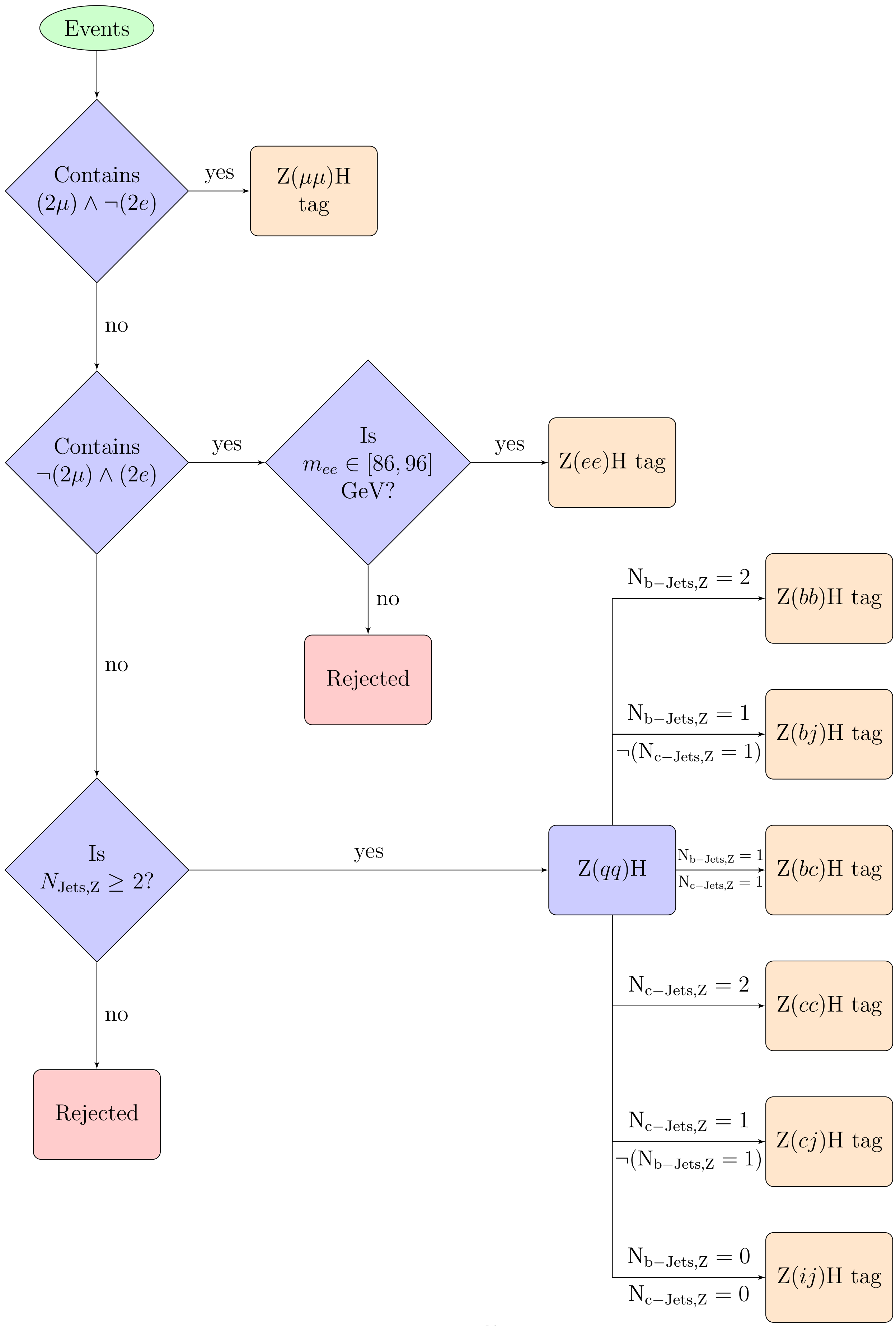

## A.2 Categorization of events at 365 GeV

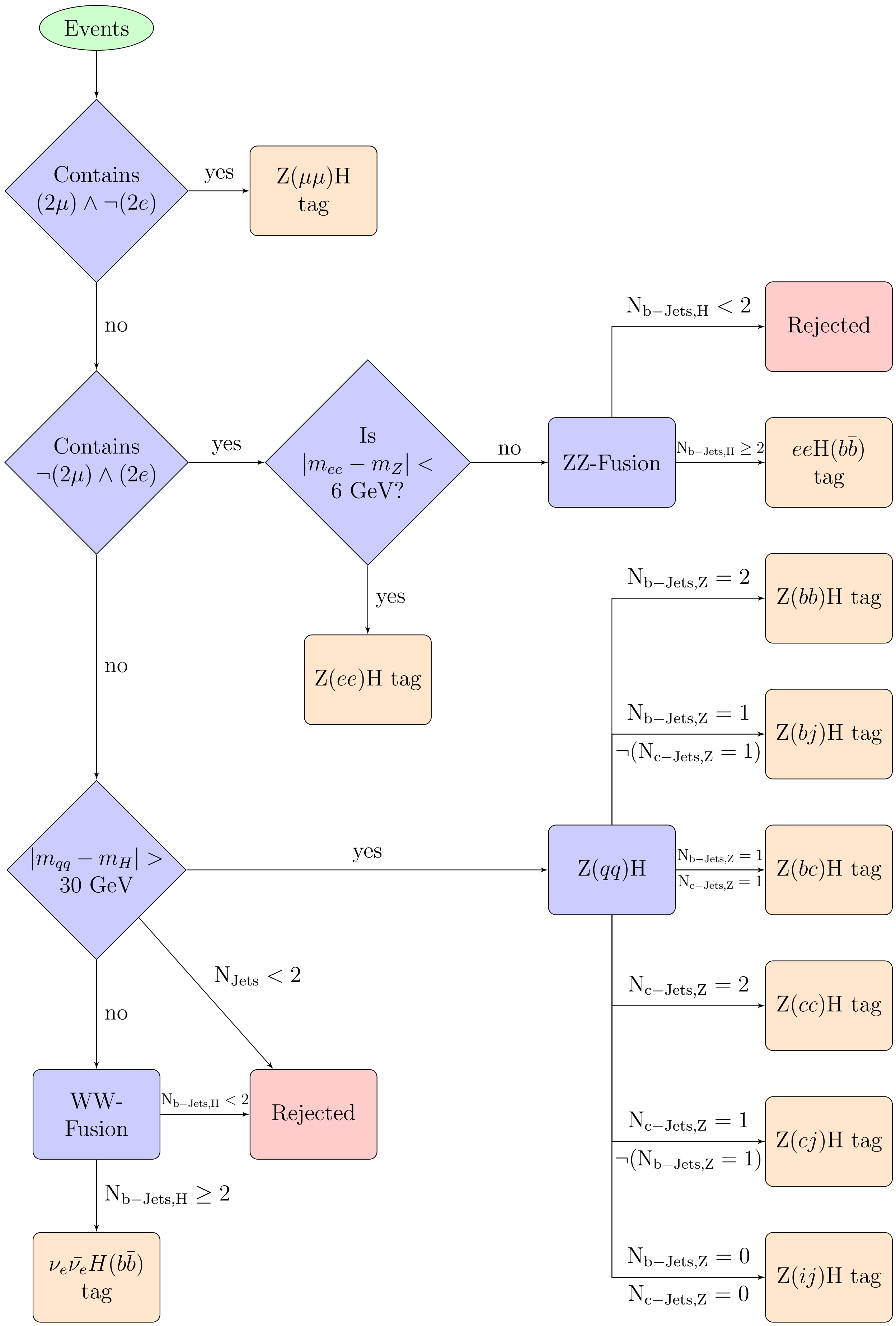

# B Cutflow

## B.1 Z($q\bar{q}$)H at 240 GeV

| | Z($q\bar{q}$)H | ZZ | WW | Z$\rightarrow q\bar{q}$ |
|---|---|---|---|---|
| Number of bb events (Yield) | 35’980 | 102’058 | 3’657 | 2’749’902 |
| Z($bb$) tag, $M_{bb} \in [86, 96]$ GeV | 100 % | 100 % | 100 % | 100 % |
| + $\beta_{bb} > 0.1535$ | 91.46 % | 33.82 % | 7.85 % | 1.86 % |
| Number of bc events (Yield) | 21’323 | 72’333 | 340’276 | 1’178’552 |
| Z($bc$) tag, $M_{bc} \in [86, 96]$ GeV | 100 % | 100 % | 100 % | 100 % |
| + $\beta_{bc} > 0.1836$ | 94.84 % | 61.75 % | 37.30 % | 7.41 % |
| Number of bj events (Yield) | 77’962 | 239’121 | 459’119 | 3’877’196 |
| Z($bj$) tag, $M_{bj} \in [86, 96]$ GeV | 100 % | 100 % | 100 % | 100 % |
| + $\beta_{bj} > 0.2211$ | 89.70 % | 56.60 % | 12.35 % | 7.41 % |
| Number of cc events (Yield) | 7’669 | 75’904 | 151’562 | 2’212’543 |
| Z($cc$) tag, $M_{cc} \in [86, 96]$ GeV | 100 % | 100 % | 100 % | 100 % |
| + $\beta_{cc} > 0.3920$ | 43.81 % | 2.48 % | 3.92 % | 0.08 % |
| Number of cj events (Yield) | 28’694 | 247’987 | 3’531’014 | 5’526’605 |
| Z($cj$) tag, $M_{cj} \in [86, 96]$ GeV | 100 % | 100 % | 100 % | 100 % |
| + $\beta_{cj} > 0.3074$ | 62.67 % | 14.07 % | 11.30 % | 0.93 % |
| Number of ij events (Yield) | 152’887 | 1’737’363 | 13’330’415 | 44’087’163 |
| Z($ij$) tag, $M_{ij} \in [86, 96]$ GeV | 100 % | 100 % | 100 % | 100 % |
| + $\beta_{ij} > 0.3710$ | 29.53 % | 1.51 % | 0.37 % | 0.06 % |

Table 17: Effects of the BDTs on the Z($q\bar{q}$)H at 240 GeV. The final classifier $\beta$ is chosen such that the significance $S/\sqrt{S+B}$ is maximized.

## B.2 Z($q\bar{q}$)H at 365 GeV

| | Z($q\bar{q}$)H | ZZ | WW | Z→ $q\bar{q}$ |
|---|---|---|---|---|
| Number of bb events (Yield) | 6'812 | 17'456 | 594 | 418'139 |
| Z($bb$) tag, $M_{bb} \in [86, 96]$ GeV | 100 % | 100 % | 100 % | 100 % |
| + $\beta_{bb} > 0.2860$ | 86.17 % | 20.61 % | 2.69 % | 0.65 % |
| Number of bc events (Yield) | 3'590 | 9'746 | 56'959 | 169'928 |
| Z($bc$) tag, $M_{bc} \in [86, 96]$ GeV | 100 % | 100 % | 100 % | 100 % |
| + $\beta_{bc} > 0.2638$ | 92.90 % | 36.63 % | 22.24 % | 4.77 % |
| Number of bj events (Yield) | 13'335 | 32'046 | 68'732 | 534'669 |
| Z($bj$) tag, $M_{bj} \in [86, 96]$ GeV | 100 % | 100 % | 100 % | 100 % |
| + $\beta_{bj} > 0.2271$ | 94.53 % | 44.75 % | 16.39 % | 7.41 % |
| Number of cc events (Yield) | 2'019 | 12'928 | 28'384 | 314'981 |
| Z($cc$) tag, $M_{cc} \in [86, 96]$ GeV | 100 % | 100 % | 100 % | 100 % |
| + $\beta_{cc} > 0.3138$ | 69.34 % | 8.00 % | 1.91 % | 0.31 % |
| Number of cj events (Yield) | 6'570 | 36'975 | 574'476 | 786'251 |
| Z($cj$) tag, $M_{cj} \in [86, 96]$ GeV | 100 % | 100 % | 100 % | 100 % |
| + $\beta_{cj} > 0.3071$ | 83.23 % | 17.35 % | 11.37 % | 2.93 % |
| Number of ij events (Yield) | 38'288 | 278'485 | 1'869'718 | 59'900'602 |
| Z($ij$) tag, $M_{ij} \in [86, 96]$ GeV | 100 % | 100 % | 100 % | 100 % |
| + $\beta_{ij} > 0.3271$ | 61.81 % | 5.05 % | 2.19 % | 0.50 % |

## B.3 Z($\mu^+\mu^-$)H at 365 GeV

| | $\mu^+\mu^- H$ | ZZ | WW | $\gamma\gamma \to \mu^+\mu^-$ |
|---|---|---|---|---|
| Number of events (Yield) | 5'061 | 56'990 | 184'907 | 693'722 |
| $N_Z = 1$ | 80.00 % | 5.87 % | 1.15 % | 16.27 % |
| $N_Z = 1$, $M_{\mu\mu} \in [86, 96]$ GeV | 65.19 % | 3.71 % | 0.02 % | 1.72 % |
| $N_Z = 1$, $M_{\mu\mu} \in [86, 96]$ GeV, $M_{Rec} \in [120, 140]$ GeV | 46.41 % | 0.33 % | 5.20$*10^{-4}$ % | 0.04 % |
| $N_Z = 1$, $M_{\mu\mu} \in [86, 96]$ GeV, $M_{Rec} \in [120, 140]$ GeV, $p_T^{\mu\mu} \in [20, 70]$ GeV | 3.11 % | 0.12 % | 2.60$*10^{-4}$ % | 6.00$*10^{-5}$ % |
| $N_Z = 1$, $M_{\mu\mu} \in [86, 96]$ GeV, $M_{Rec} \in [120, 140]$ GeV, $p_T^{\mu\mu} > 70$ GeV | 43.07 % | 0.18 % | 2.60$*10^{-4}$ % | 0 % |
| $N_Z = 1$, $M_{\mu\mu} \in [86, 96]$ GeV, $M_{Rec} \in [120, 140]$ GeV, $p_T^{\mu\mu} > 80$ GeV | 41.69 % | 0.16 % | 2.60$*10^{-4}$ % | 0 % |

# C Centrally produced MC samples

## C.1 $\sqrt{s} = 240$ GeV MC samples

| | Sample designation | Main process | MC events | Cross section |
|---|---|---|---|---|
| Signal | wzp6_ee_mumuH_ecm240 | $e^+e^- \to Z(\mu^+\mu^-)H$ | 1'000'000 | 0.0067643 |
| | wzp6_ee_eeH_ecm240 | $e^+e^- \to Z(e^+e^-)H$ | 900'000 | 0.0071611 |
| | wzp6_ee_qqH_ecm240 | $e^+e^- \to Z(q\bar{q})H$ | 9'900'000 | 0.13635 |
| Background | p8_ee_WW_ecm240 | $e^+e^- \to W^+W^-$ | 10'000'000 | 16.4385 |
| | p8_ee_ZZ_ecm240 | $e^+e^- \to ZZ$ | 10'000'000 | 1.35899 |
| | p8_ee_Zqq_ecm240 | $e^+e^- \to q\bar{q}$ | 10'000'000 | 52.6539 |
| | wzp6_ee_Mee_30_150_ecm240 | $e^+e^- \to e^+e^-$ | 79'400'000 | 8.305 |
| | wzp6_ee_mumu_ecm240 | $e^+e^- \to \mu^+\mu^-$ | 49'400'000 | 5.288 |
| | wzp6_ee_tautau_ecm240 | $e^+e^- \to \tau^+\tau^-$ | 49'600'000 | 4.668 |
| | wzp6_gaga_mumu_60_ecm240 | $\gamma\gamma \to \mu^+\mu^-$ | 30'000'000 | 1.5523 |

Table 18: Monte Carlo samples used for the processes at $\sqrt{s} = 240$ GeV [33]. The cross sections are in $\text{pb}^{-1}$.

## C.2 $\sqrt{s} = 365$ GeV MC samples

| | Sample designation | Main process | MC events | Cross section |
|---|---|---|---|---|
| Signal | wzp6_ee_mumuH_ecm365 | $e^+e^- \to Z(\mu^+\mu^-)H$ | 200'000 | 0.004185 |
| | wzp6_ee_eeH_ecm365 | $e^+e^- \to e^+e^-H$ | 400'000 | 0.00739 |
| | wzp6_ee_qqH_ecm365 | $e^+e^- \to Z(q\bar{q})H$ | 2'000'000 | 0.084307 |
| | wzp6_ee_nunuH_ecm365 | $e^+e^- \to \nu\bar{\nu}H$ | 1'000'000 | 0.05394 |
| Background | p8_ee_WW_ecm365 | $e^+e^- \to WW$ | 5'000'000 | 10.7165 |
| | p8_ee_ZZ_ecm365 | $e^+e^- \to ZZ$ | 5'000'000 | 0.6428 |
| | p8_ee_Zqq_ecm365 | $e^+e^- \to q\bar{q}$ | 59'500'000 | 21.4149 |
| | p8_ee_ZH_ecm365 | $e^+e^- \to ZH$ | 5'000'000 | 0.1173 |
| | wzp6_ee_Mee_30_150_ecm365 | $e^+e^- \to e^+e^-$ | 10'000'000 | 1.53 |
| | wzp6_ee_mumu_ecm365 | $e^+e^- \to \mu^+\mu^-$ | 9'900'000 | 2.287 |
| | wzp6_ee_tautau_ecm365 | $e^+e^- \to \tau^+\tau^-$ | 10'000'000 | 2.017 |
| | wzp6_gaga_mumu_60_ecm365 | $e^+e^- \to \gamma\gamma \to \mu^+\mu^-$ | 10'000'000 | 2.843 |

Table 19: Monte Carlo samples used for the processes at $\sqrt{s} = 365$ GeV [33]. The cross sections are in $\text{pb}^{-1}$.

# D Profile likelihood plots

## D.1 Higgs mass measurement

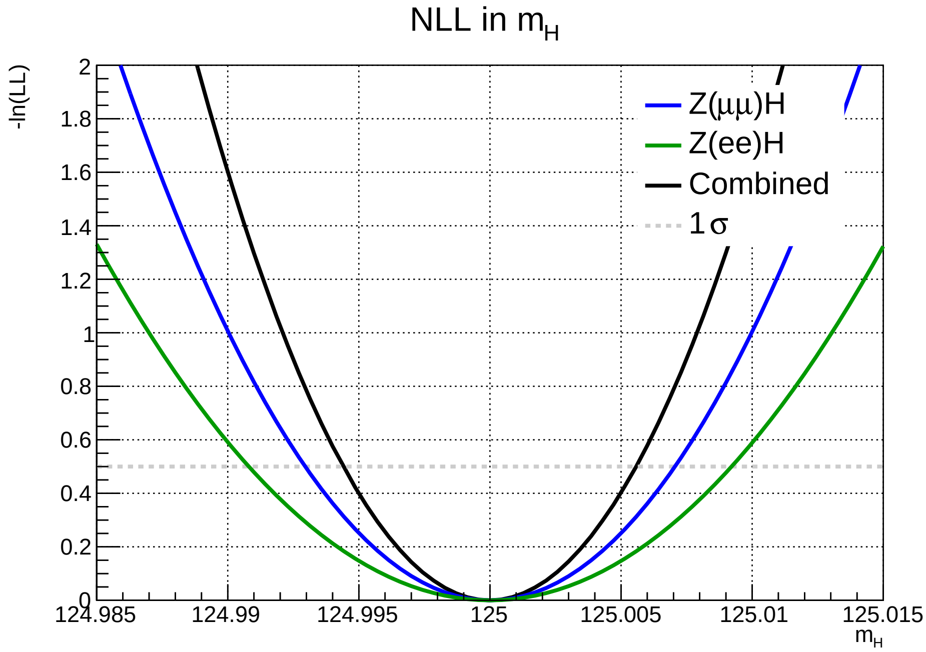


Figure 20: The profile likelihood of the reconstructed Higgs boson mass $m_H$. The contribution of $Z(\mu^+\mu^-)H$ at 240 GeV in blue, $Z(e^+e^-)H$ at 240 GeV is in green and the combined contribution at both energies for all leptonic Z decays in black. The one sigma line is at 0.5.

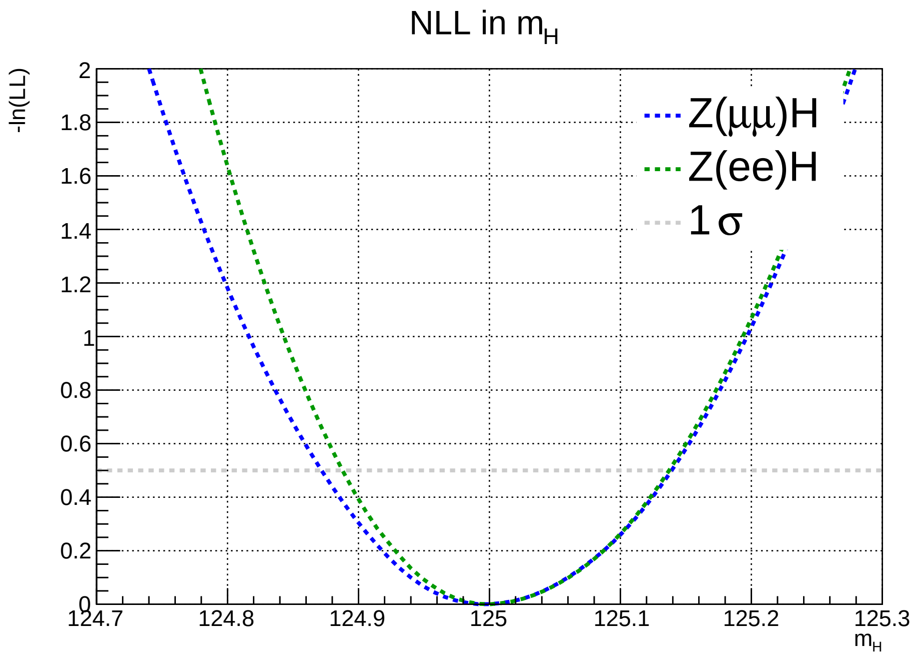


Figure 21: The profile likelihood of the reconstructed Higgs boson mass $m_H$. The contribution of $Z(\mu^+\mu^-)H$ at 365 GeV in blue and $Z(e^+e^-)H$ at 365 GeV in green. The sensitivity on the Higgs boson mass is significantly degraded compared to the 240 GeV channels due to the poor $p_T$ resolution of the drift chamber 1.1. The one sigma line is at 0.5.

## D.2 Cross section measurement

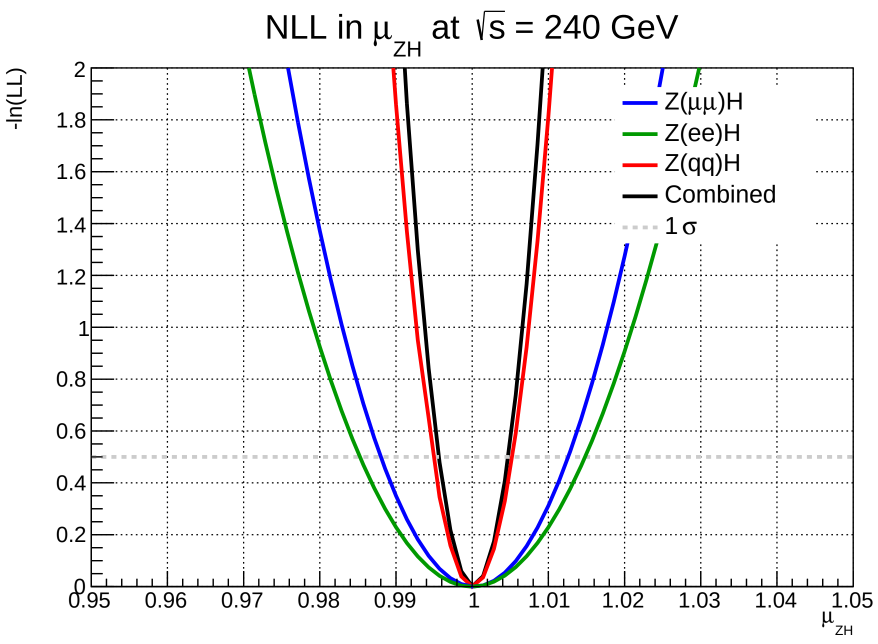


(a)

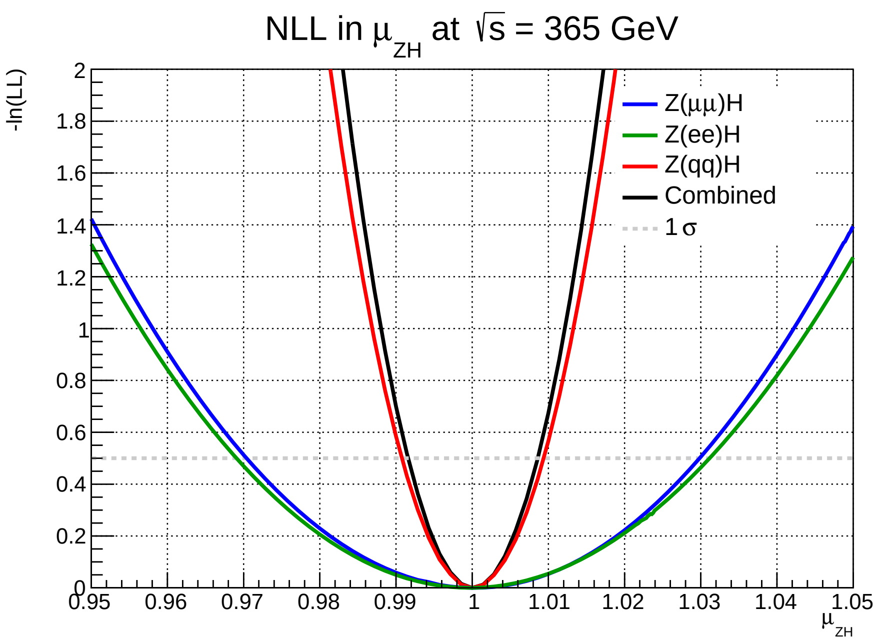


(b)

Figure 22: The profile likelihoods of the signal strength modifier $\mu$ at different energies for different Higgs boson production processes. The contributions to $\mu_{\mathrm{ZH}}$ from different ZH channels at $\sqrt{s} = 240$ GeV (a) and $\sqrt{s} = 365$ GeV (b). In both cases the hadronic ZH has the highest contribution to the sensitivity.

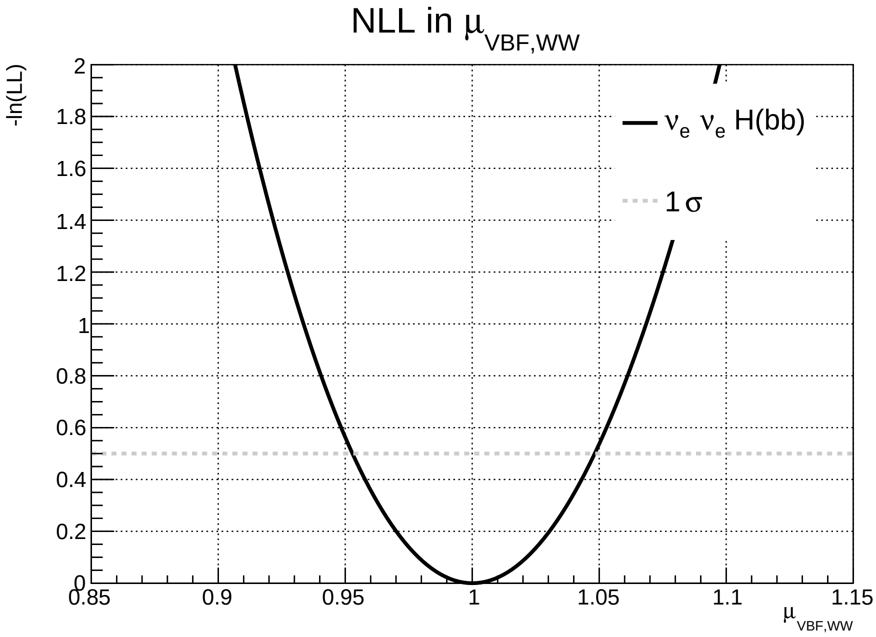


(a)

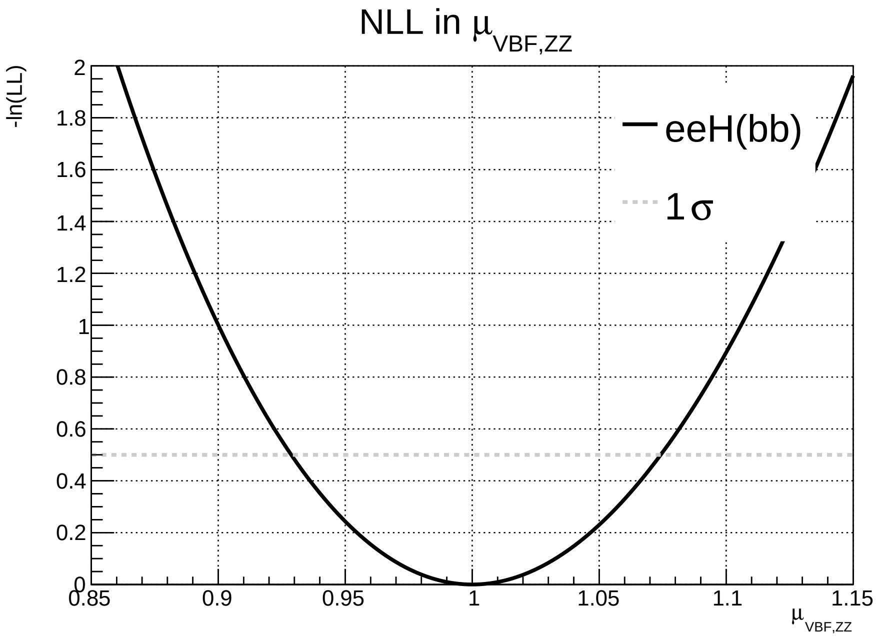


(b)

Figure 23: The profile likelihoods of the signal strength modifier $\mu$ at different energies for different Higgs boson production processes. (a): The signal strength modifier $\mu_{\mathrm{VBF,WW}}$ for the charged VBF. (b): The signal strength modifier $\mu_{\mathrm{VBF,ZZ}}$ for the neutral VBF. The one sigma line is at 0.5 in all Figures.

### D.3 $\kappa_\lambda$ measurement

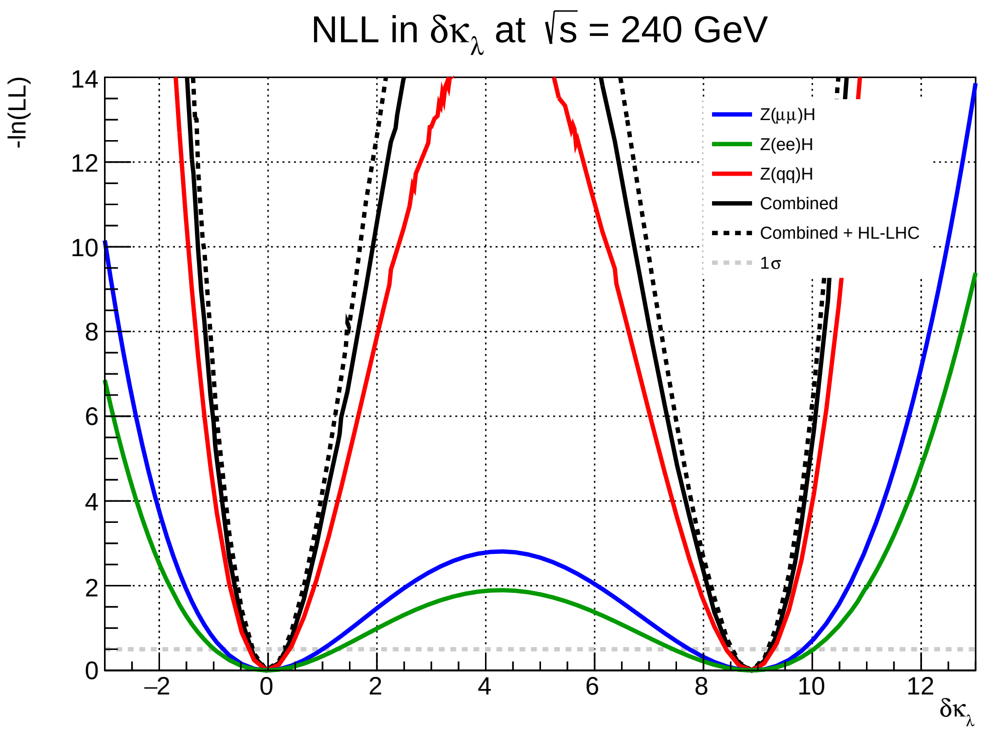


(a)

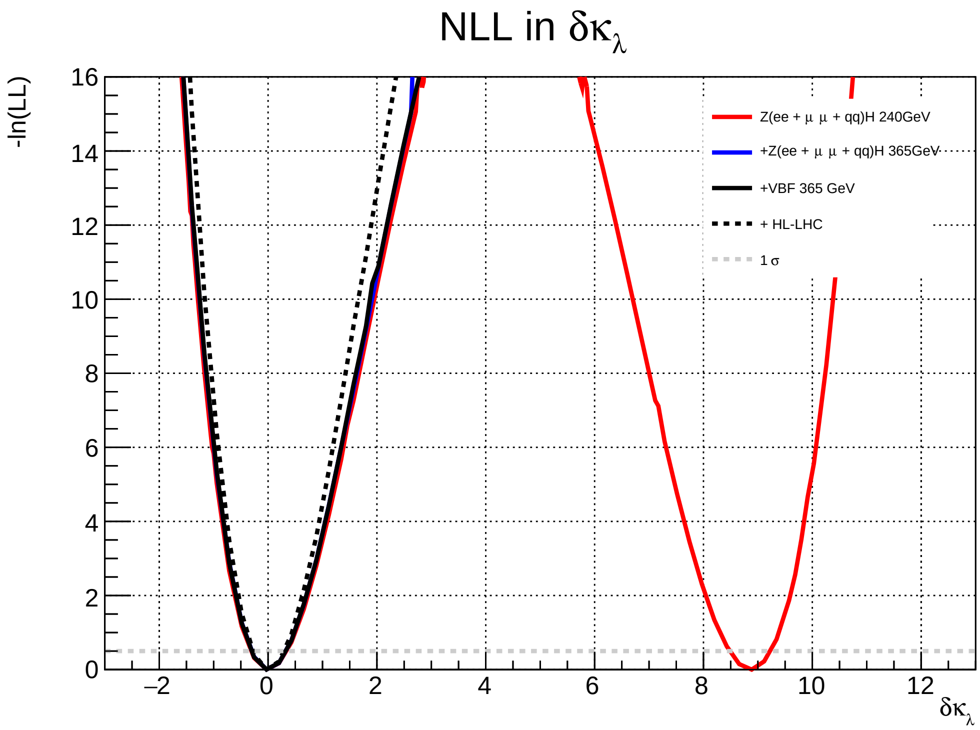


(b)

Figure 24: (a): Profile likelihood of Higgsstrahlung processes at 240 GeV. The degeneracy around $\delta\kappa_\lambda \approx 9$ is introduced by the wave-function renormalization $Z_H$. (b): The combined analysis with ZH and VBF at both energies. The degeneracy is lifted after introducing the inclusive ZH channel at 365 GeV.

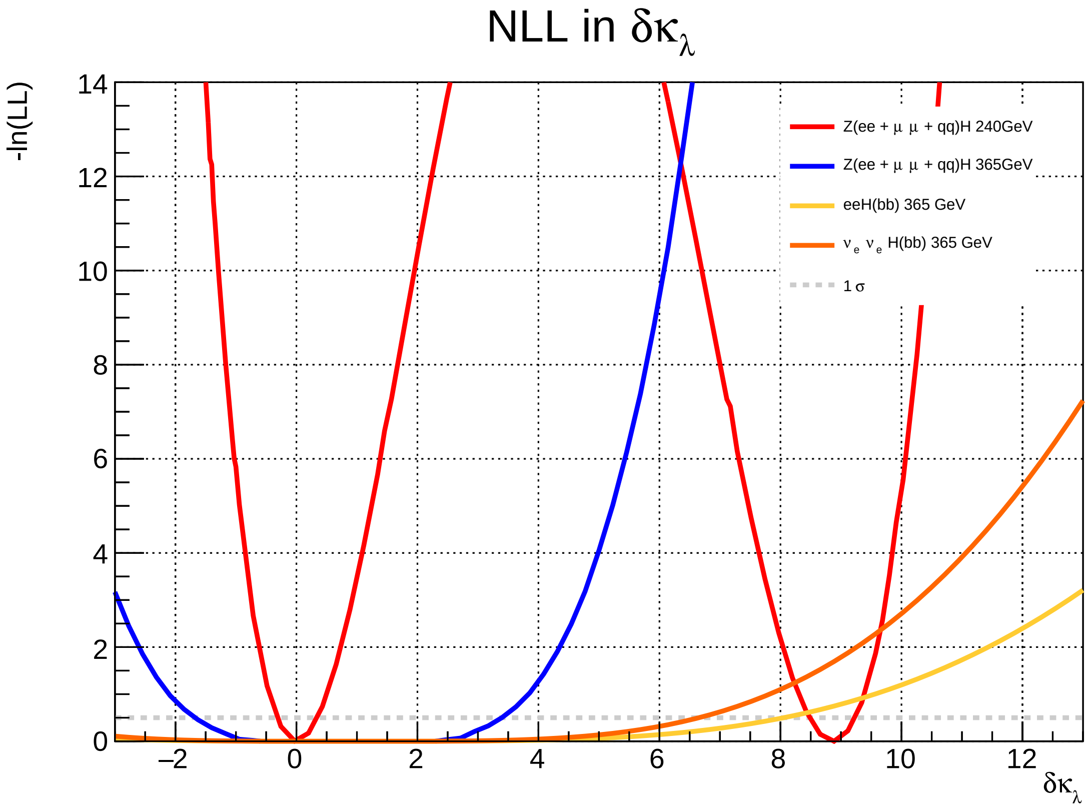


Figure 25: Profile likelihood of all processes at both energies showing the precision reach of each channels separately.

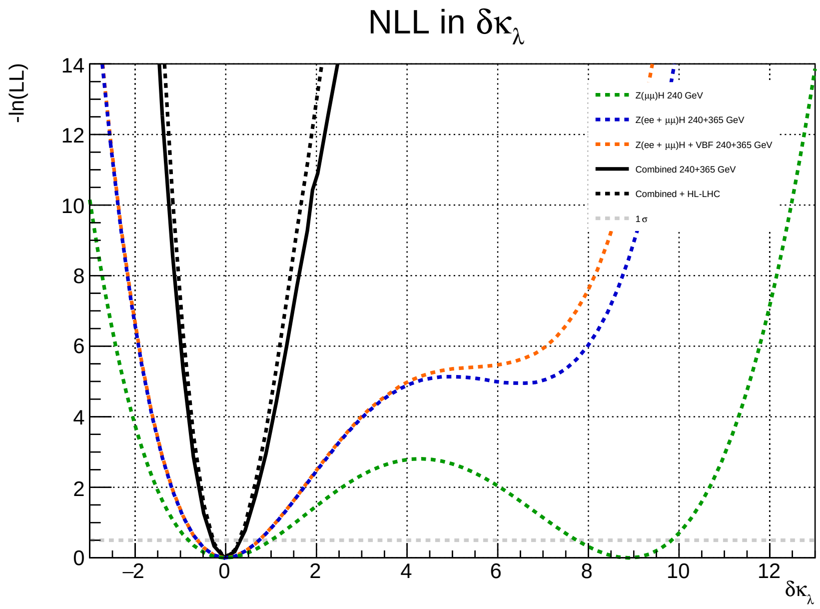


Figure 26: The profile likelihood of the deviation of $\kappa_\lambda$ from the SM value. The contribution of $Z(\mu^+\mu^-)H$ at 240 GeV is in green, leptonic ZH at both energies in blue, leptonic ZH at both energies plus VBF at 365 GeV in orange and the combined contribution at both energies for all considered Higgs boson production processes in black. Adding additionally the constraint expected to be put in place by the HL-LHC [14] result in the dashed black line. The one sigma line is at 0.5.

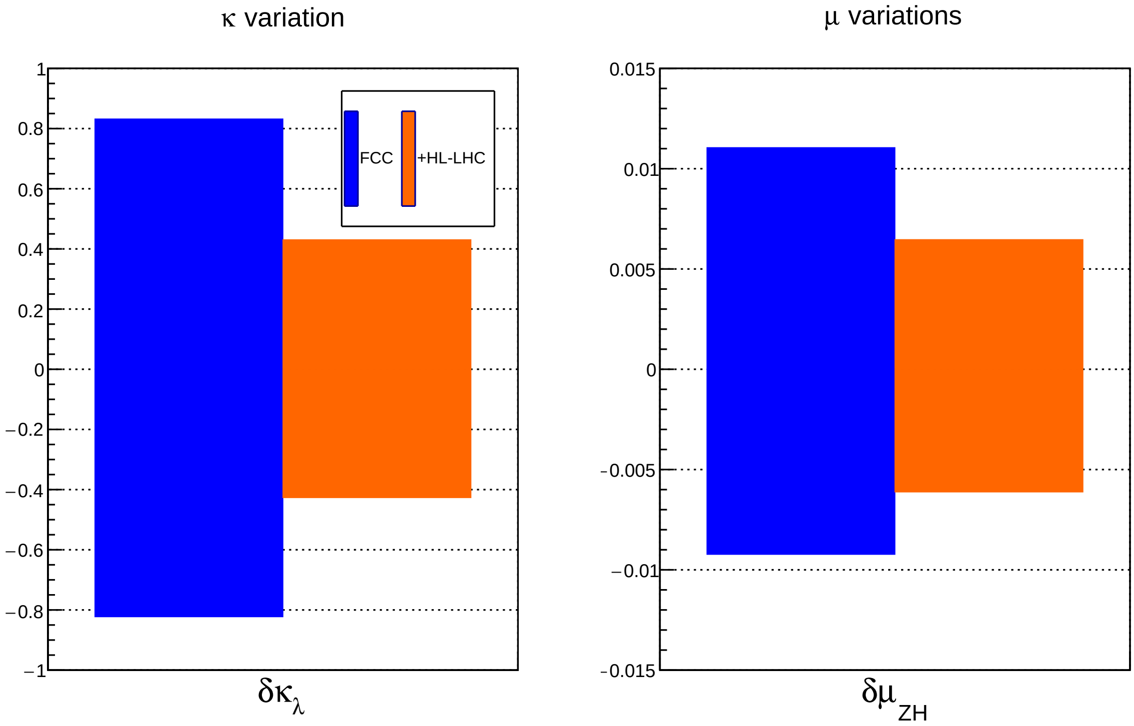


(a)

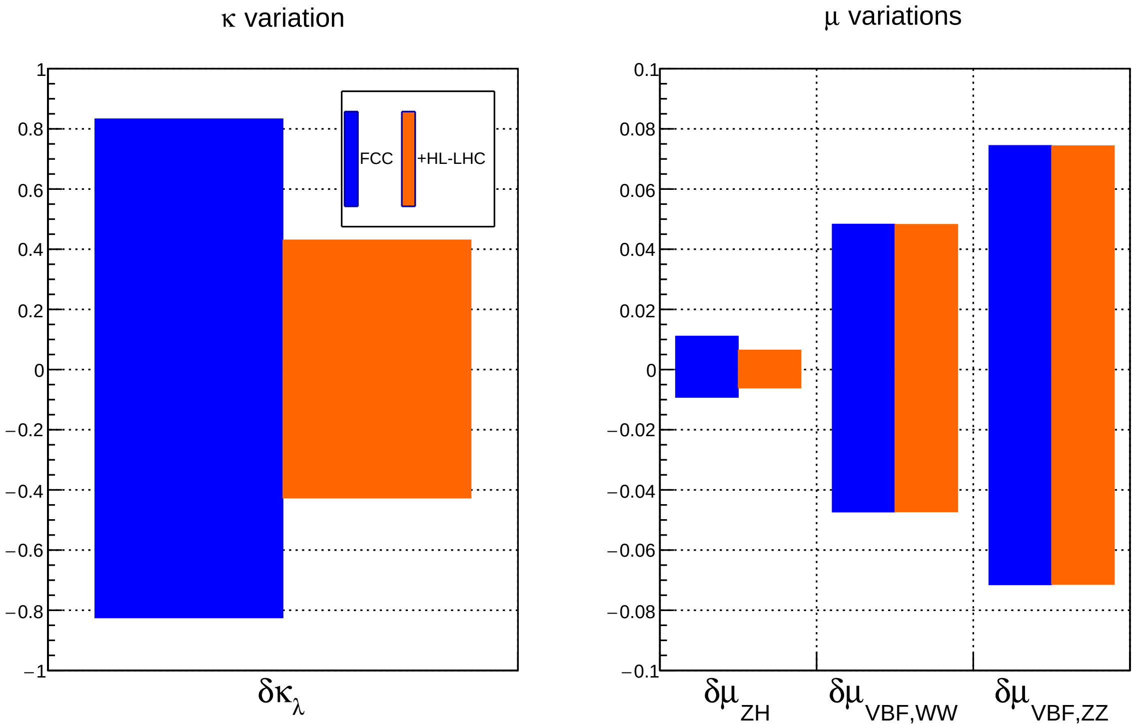


(b)

Figure 27: (a): The variations from $\kappa_\lambda$ and $\mu_{ZH}$ when leaving them floating in the 2D fit without (blue) and with (orange) constraints from HL-LHC. We assumed that $\mu_{ZH}$ is the same at 240 GeV and 365 GeV. (b): The variations from the POI in the 4D fit.

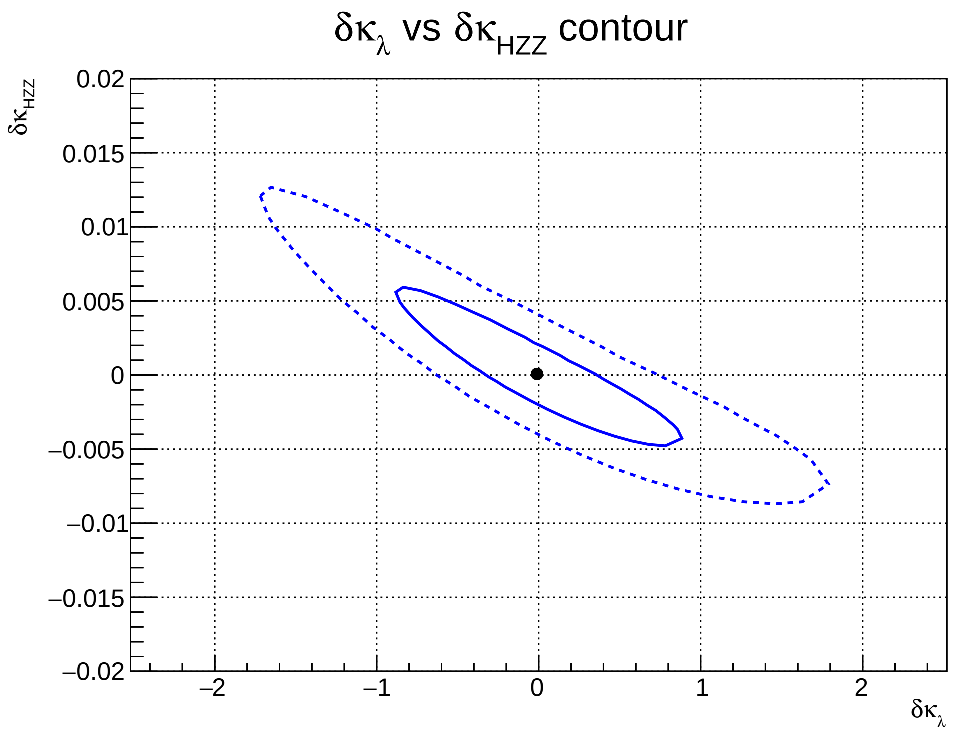


(a)

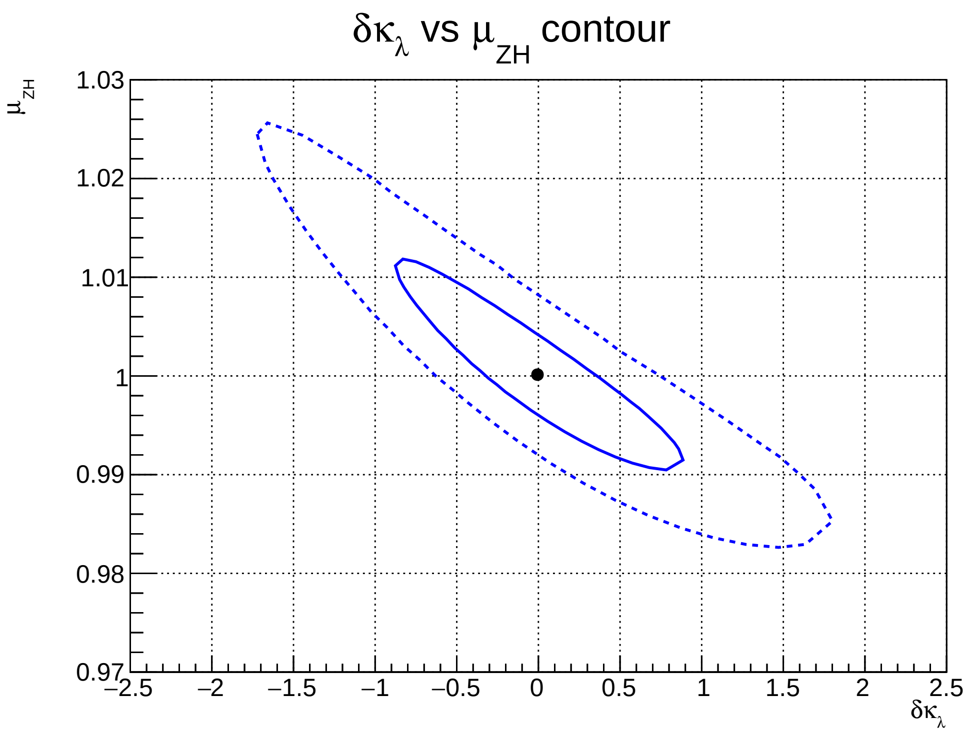


(b)

Figure 28: (a): The NLL contour of $\delta\kappa_\lambda$ (x axis) and $\delta\kappa_{\mathrm{HZZ}}$ (y axis) involving all ZH and VBF at both energies and no HL-LHC constraint. The solid blue line represents the contour at 68% CL and the dashed blue line represents the contour at 95% CL. The black dot is corresponding to the SM expectation of the two POI. (b): The NLL contour of $\delta\kappa_\lambda$ (x axis) and $\mu_{\mathrm{ZH}}$ (y axis) involving all ZH and VBF at both energies and no HL-LHC constraint. The values of $\mu_{\mathrm{VBF,WW}}$ and $\mu_{\mathrm{VBF,ZZ}}$ are fixed to unity.

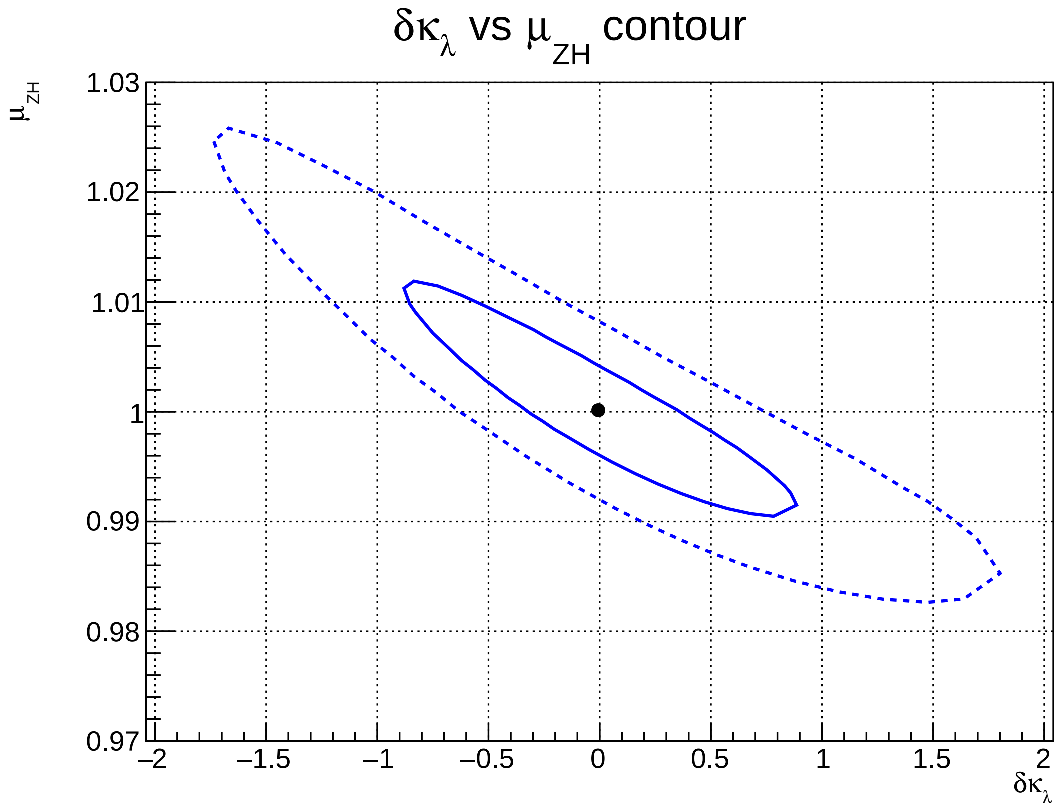


Figure 29: The NLL contour of $\delta\kappa_\lambda$ (x axis) and $\mu_{\text{ZH}}$ (y axis) involving all ZH and VBF at both energies and no HL-LHC constraint. The solid blue line represents the contour at 68% CL and the dashed blue line represents the contour at 95% CL. The black dot is corresponding to the SM expectation of the two POI. The values of $\mu_{\text{VBF,WW}}$ and $\mu_{\text{VBF,ZZ}}$ are floating parameters of the fit.

## E $M_{\text{Rec}}$ vs. $M_{ij}$ distribution

The following section will show the $M_{\text{Rec}}$ vs. $M_{ij}$ distribution of the $e^+e^- \to q\bar{q}$ background sample before and after applying the BDT.

### E.1 $\sqrt{s} = 240$ GeV

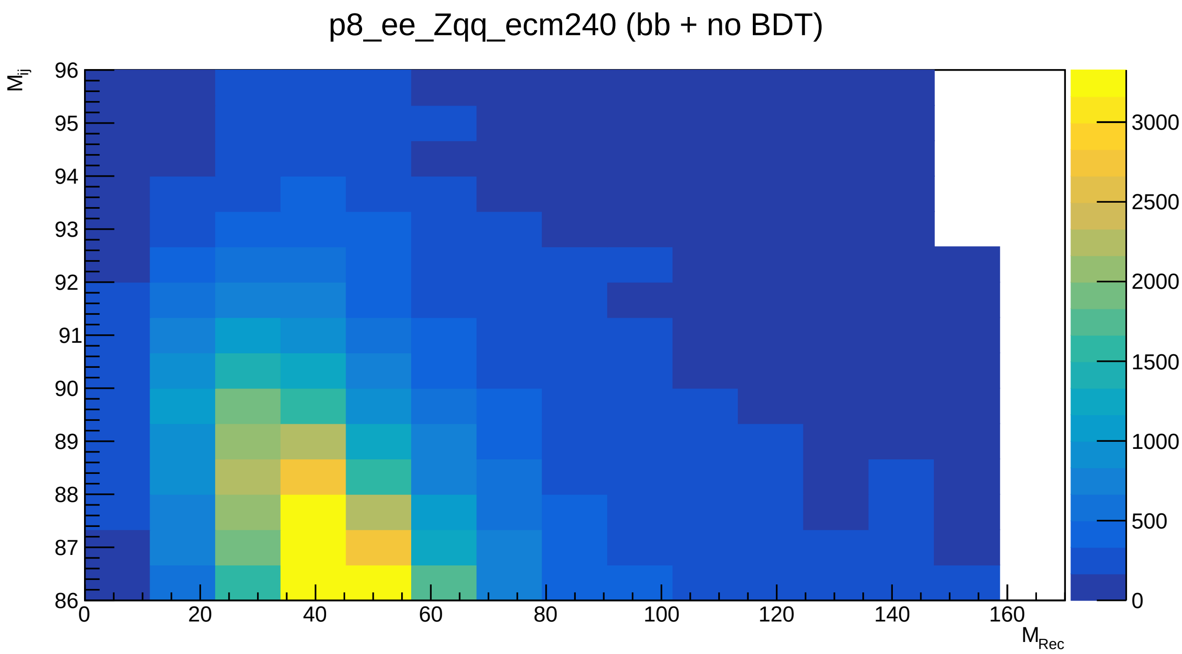


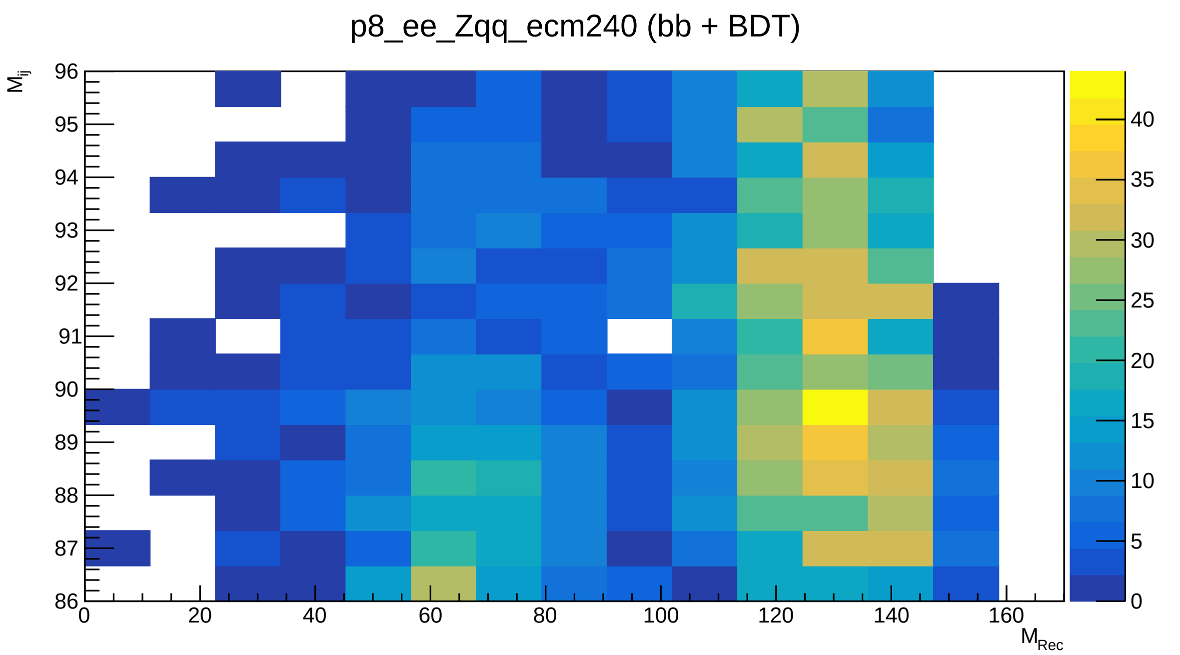


Figure 30: A 2D distribution with the recoil mass $M_{\text{Rec}} \in [0, 170]$ GeV on the x axis and the di-jet mass $M_{ij} \in [86, 96]$ GeV on the y axis. Both plots show the PYTHIA8 $Z \to q\bar{q}$ background sample where $q, \bar{q} = b$.

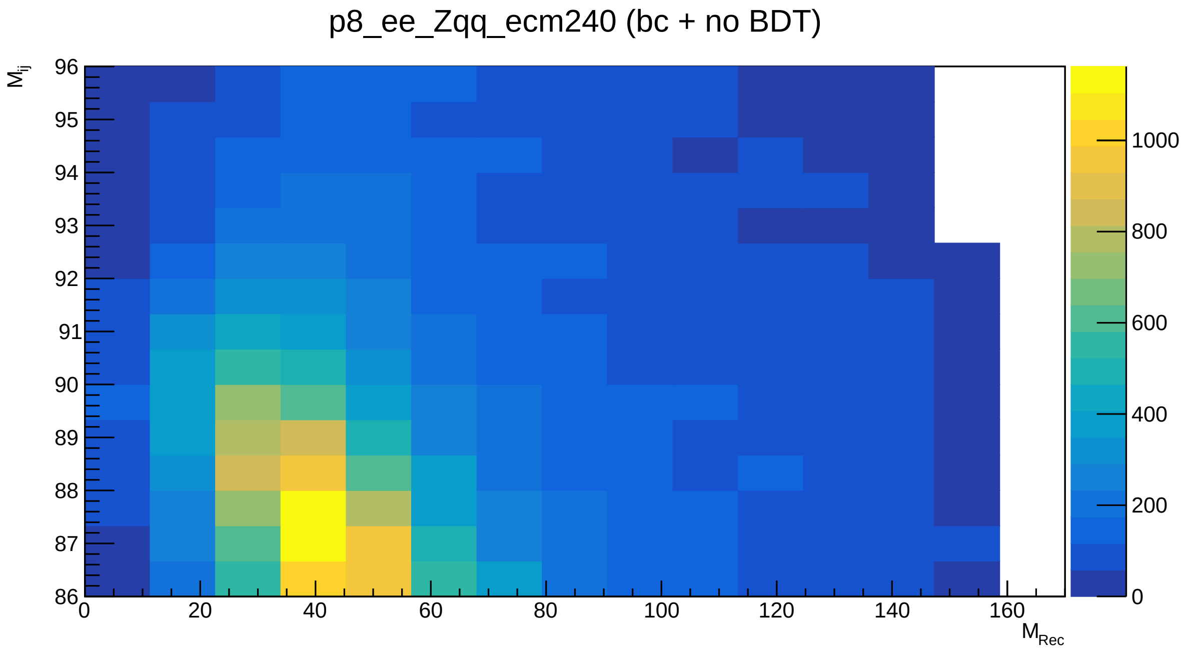


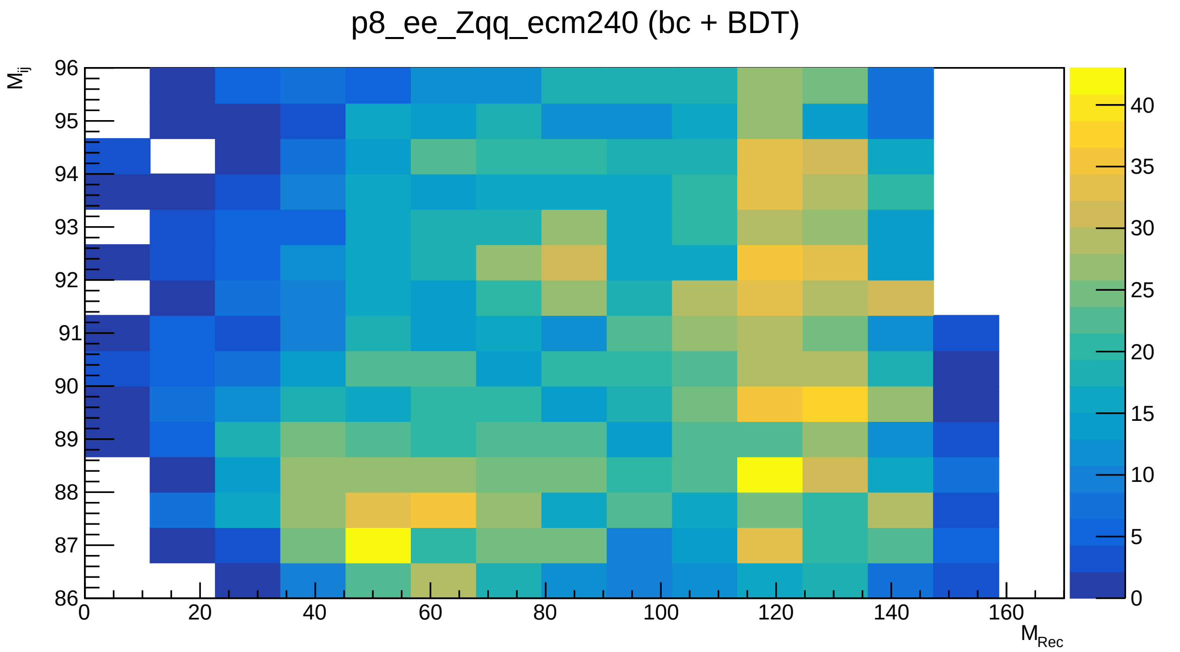


Figure 31: A 2D distribution with the recoil mass $M_{\text{Rec}} \in [0, 170]$ GeV on the x axis and the di-jet mass $M_{ij} \in [86, 96]$ GeV on the y axis. Both plots show the PYTHIA8 $Z \to q\bar{q}$ background sample where $q, \bar{q} \in \{b, c\}$.

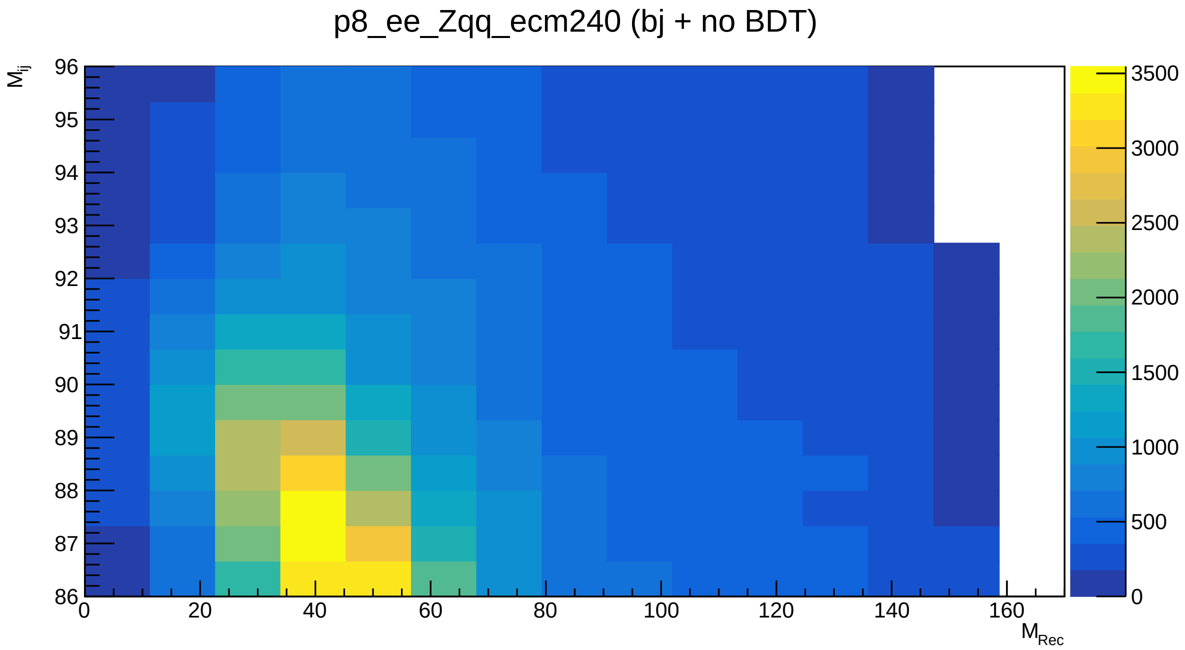


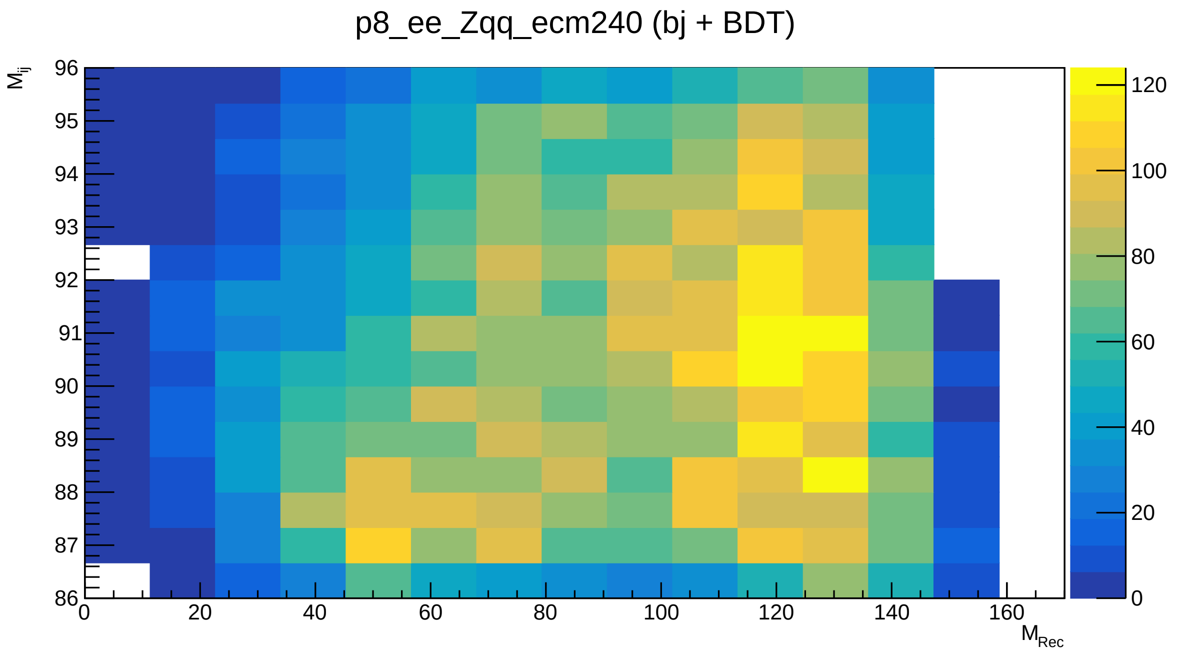


Figure 32: A 2D distribution with the recoil mass $M_{\text{Rec}} \in [0, 170]$ GeV on the x axis and the di-jet mass $M_{ij} \in [86, 96]$ GeV on the y axis. Both plots show the `PYTHIA8` $Z \to q\bar{q}$ background sample where $q, \bar{q} \in \{b, j\}$.

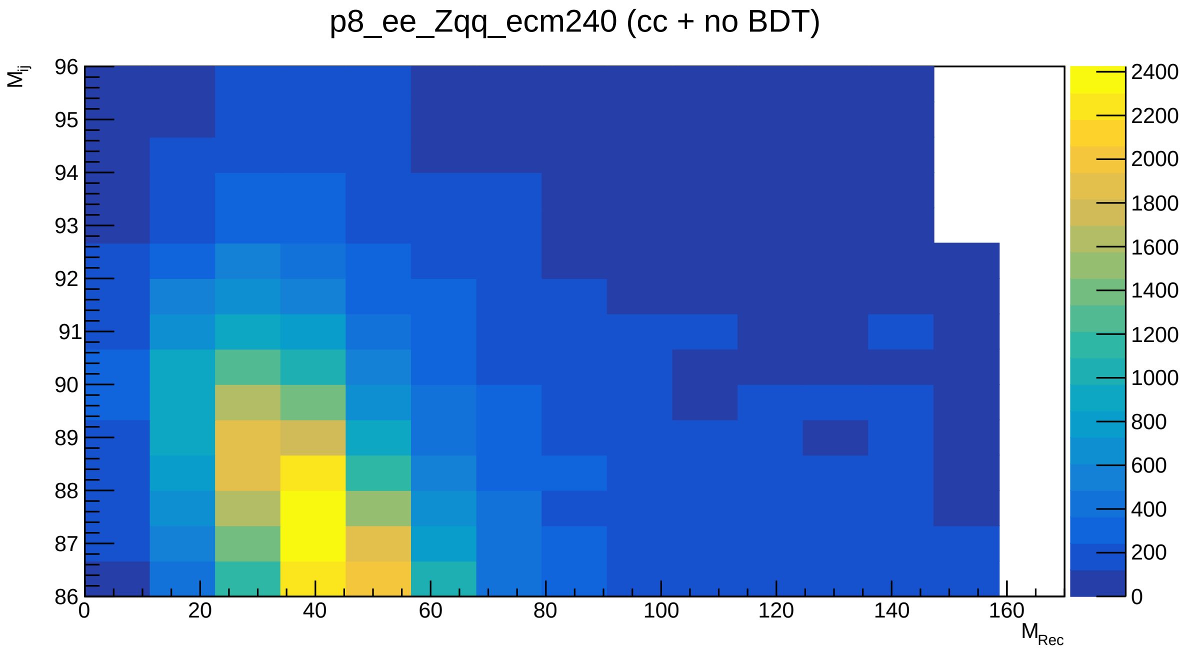


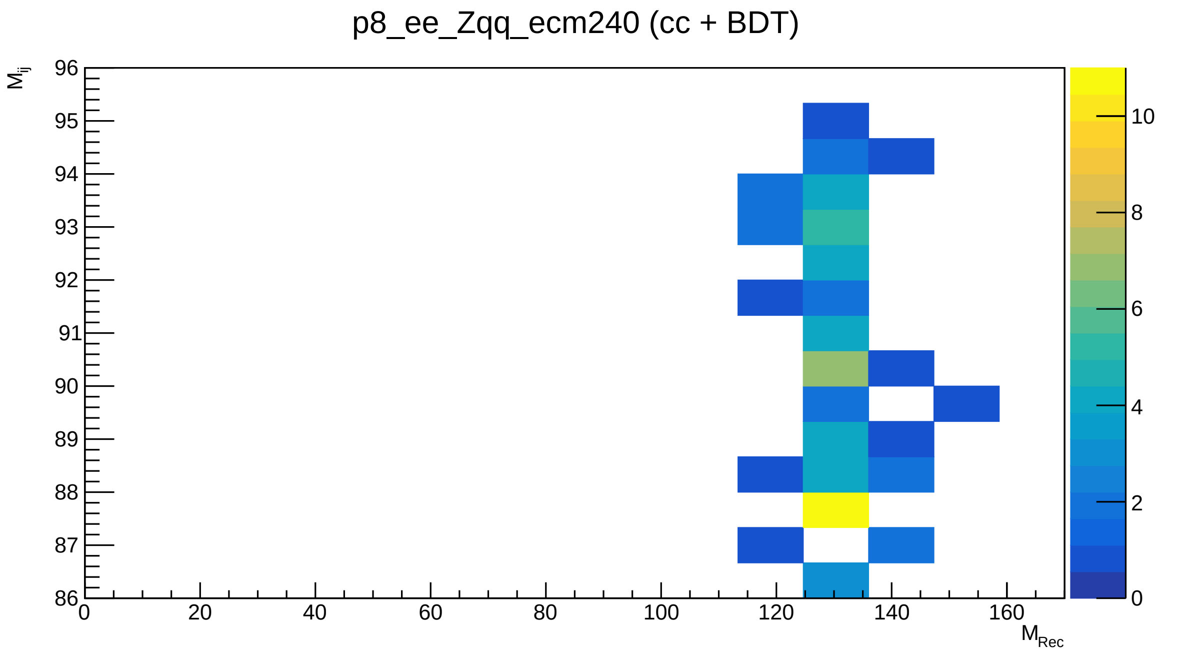


Figure 33: A 2D distribution with the recoil mass $M_{\text{Rec}} \in [0, 170]$ GeV on the x axis and the di-jet mass $M_{ij} \in [86, 96]$ GeV on the y axis. Both plots show the PYTHIA8 $Z \to q\bar{q}$ background sample where $q, \bar{q} = c$.

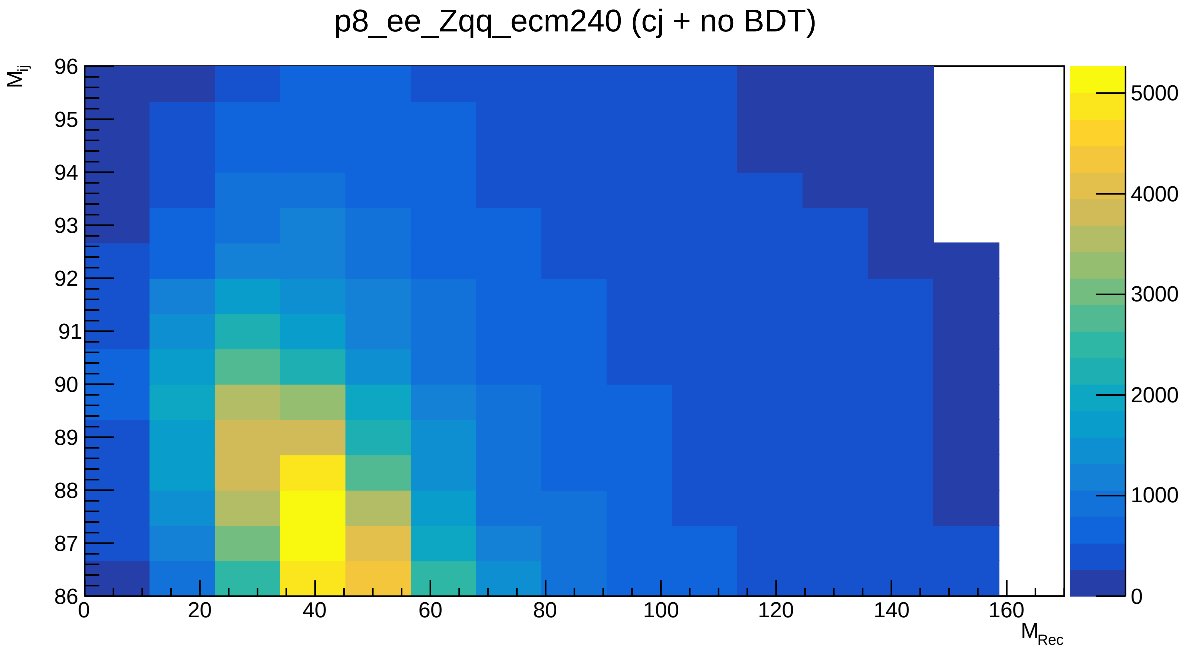


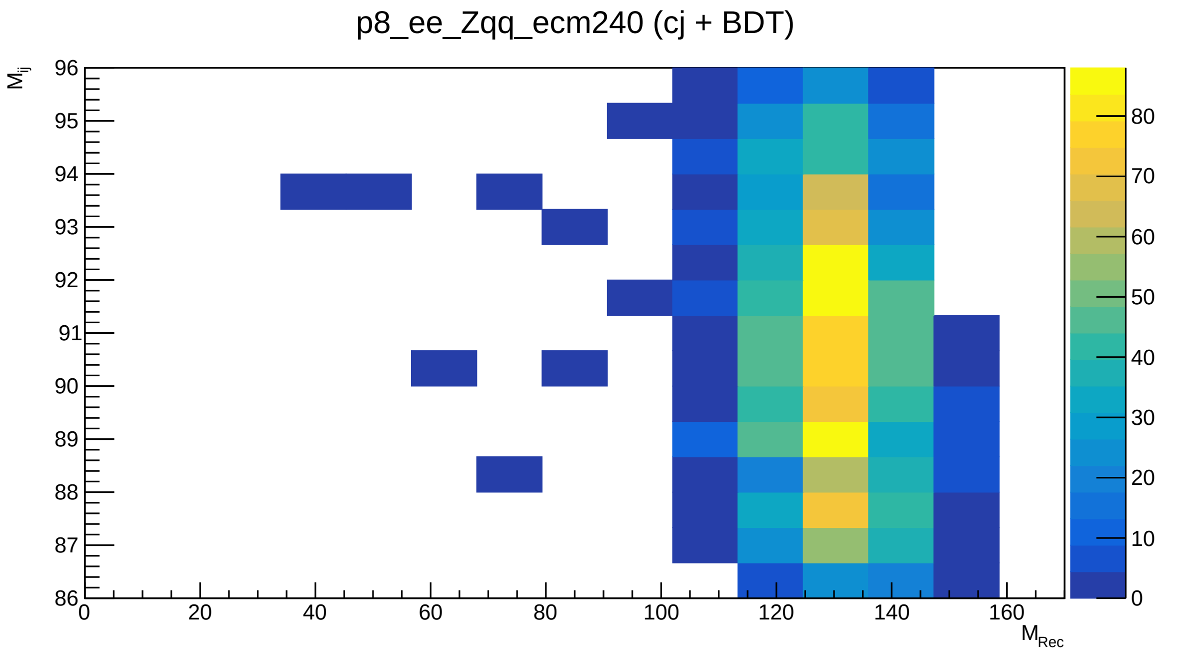


Figure 34: A 2D distribution with the recoil mass $M_{\text{Rec}} \in [0, 170]$ GeV on the x axis and the di-jet mass $M_{ij} \in [86, 96]$ GeV on the y axis. Both plots show the PYTHIA8 $Z \to q\bar{q}$ background sample where $q, \bar{q} \in \{c, j\}$.

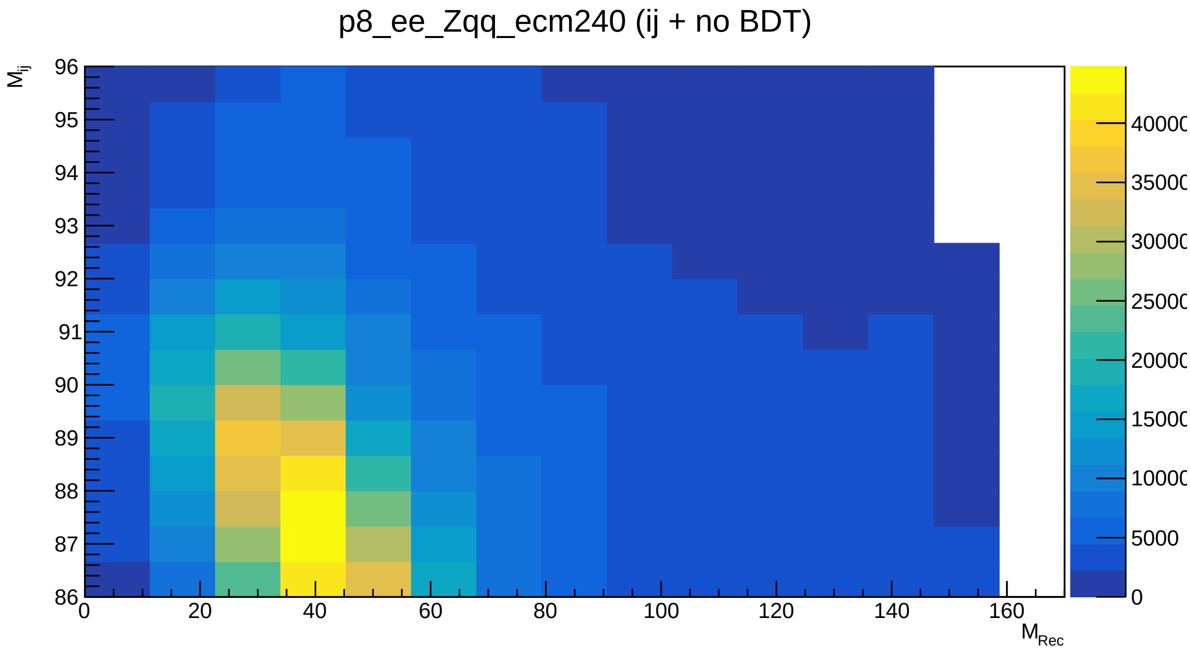


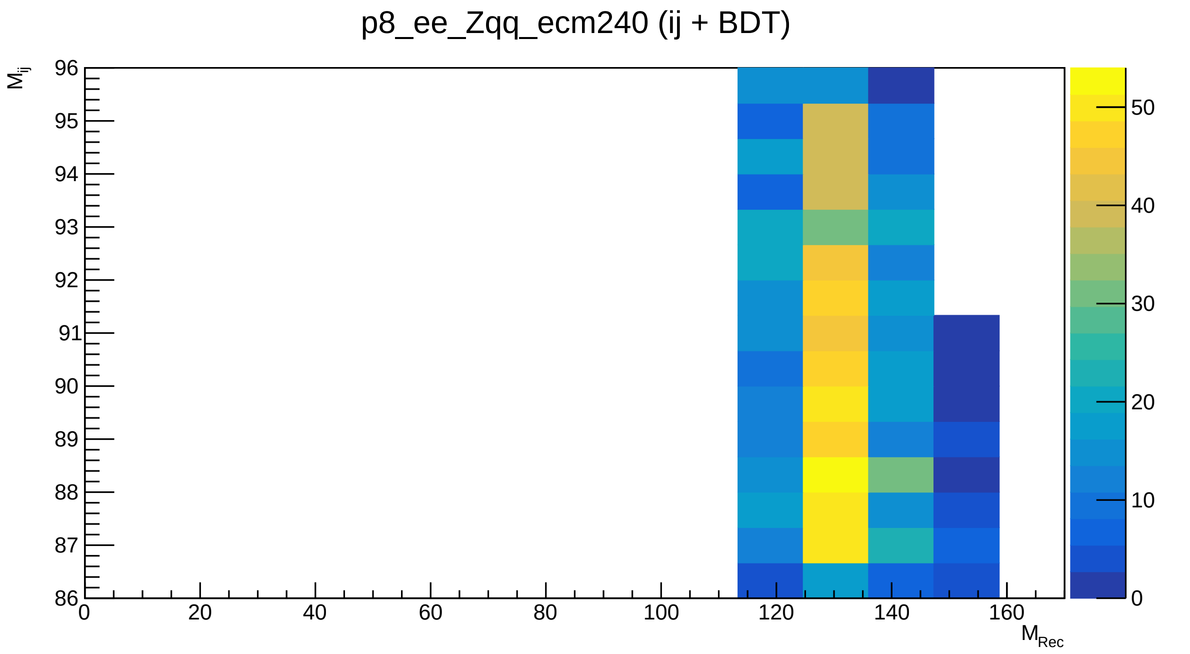


Figure 35: A 2D distribution with the recoil mass $M_{\mathrm{Rec}} \in [0, 170]$ GeV on the x axis and the di-jet mass $M_{ij} \in [86, 96]$ GeV on the y axis. Both plots show the `PYTHIA8` $Z \rightarrow q\bar{q}$ background sample where $q, \bar{q} \in \{i, j\}$.

## E.2 $\sqrt{s} = 365$ GeV

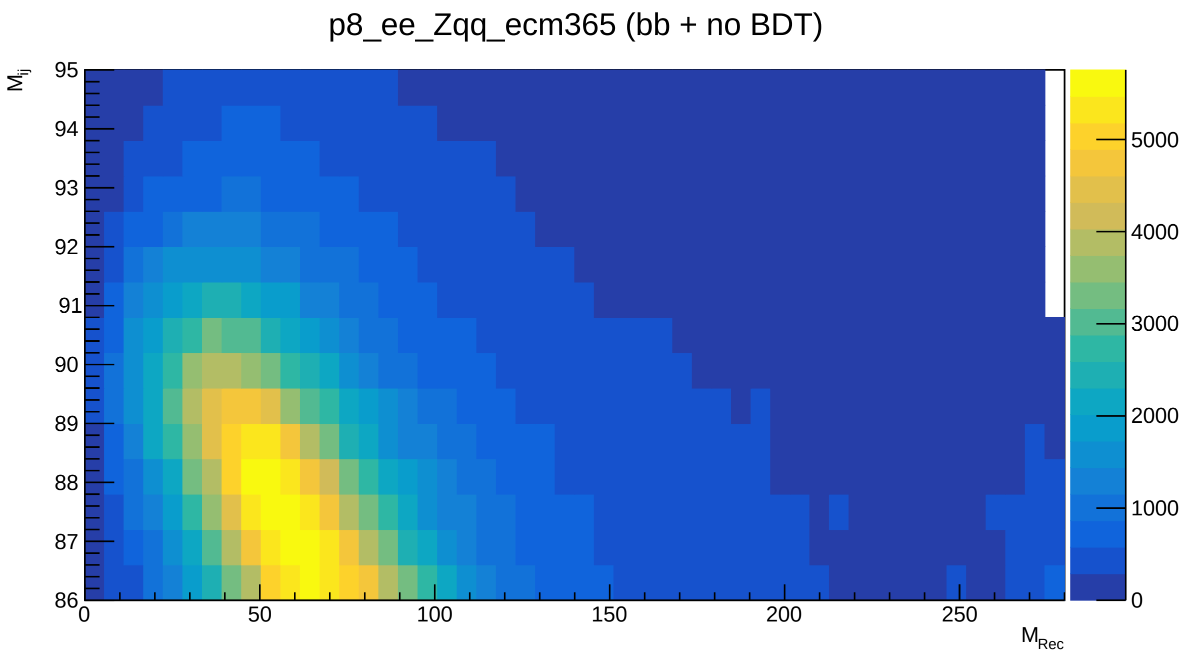


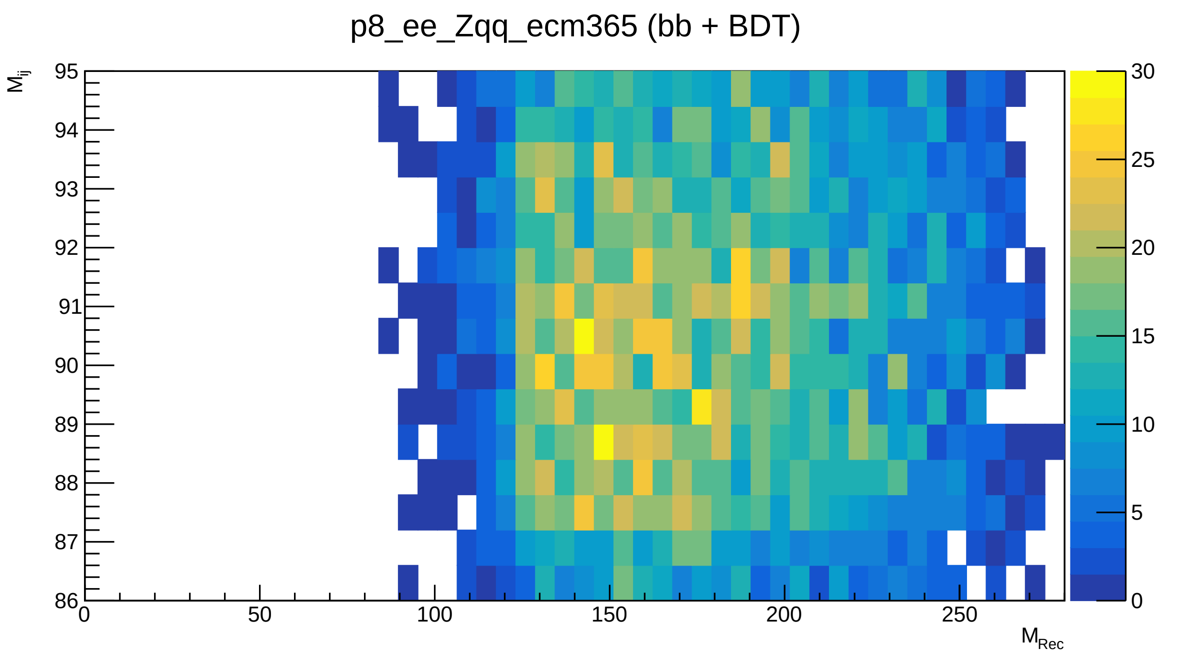


Figure 36: A 2D distribution with the recoil mass $M_{\text{Rec}} \in [0, 170]$ GeV on the x axis and the di-jet mass $M_{ij} \in [86, 96]$ GeV on the y axis. Both plots show the PYTHIA8 $Z \to q\bar{q}$ background sample where $q, \bar{q} = b$.

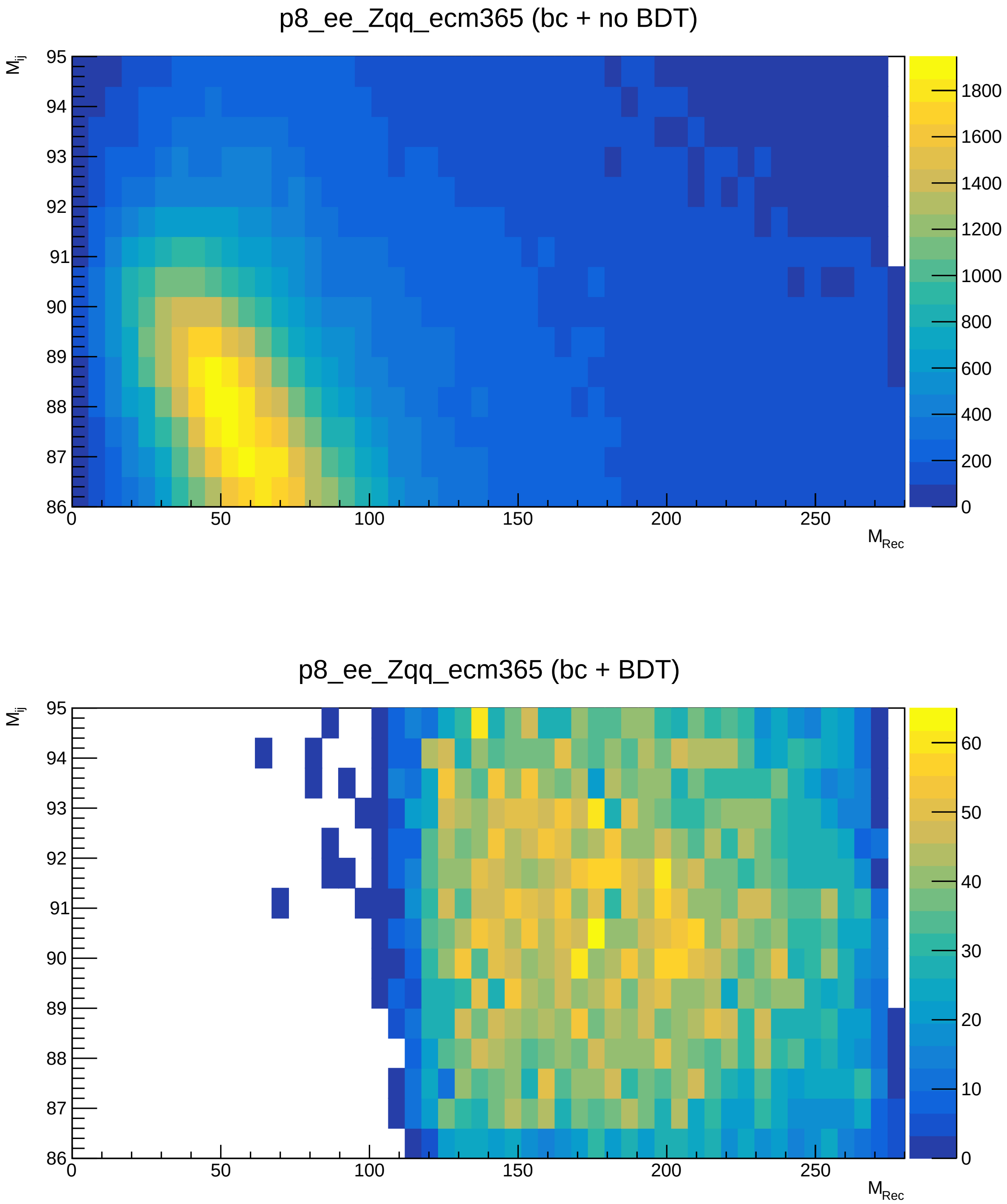


Figure 37: A 2D distribution with the recoil mass $M_{\text{Rec}} \in [0, 170]$ GeV on the x axis and the di-jet mass $M_{ij} \in [86, 96]$ GeV on the y axis. Both plots show the PYTHIA8 $Z \to q\bar{q}$ background sample where $q, \bar{q} \in \{b, c\}$.

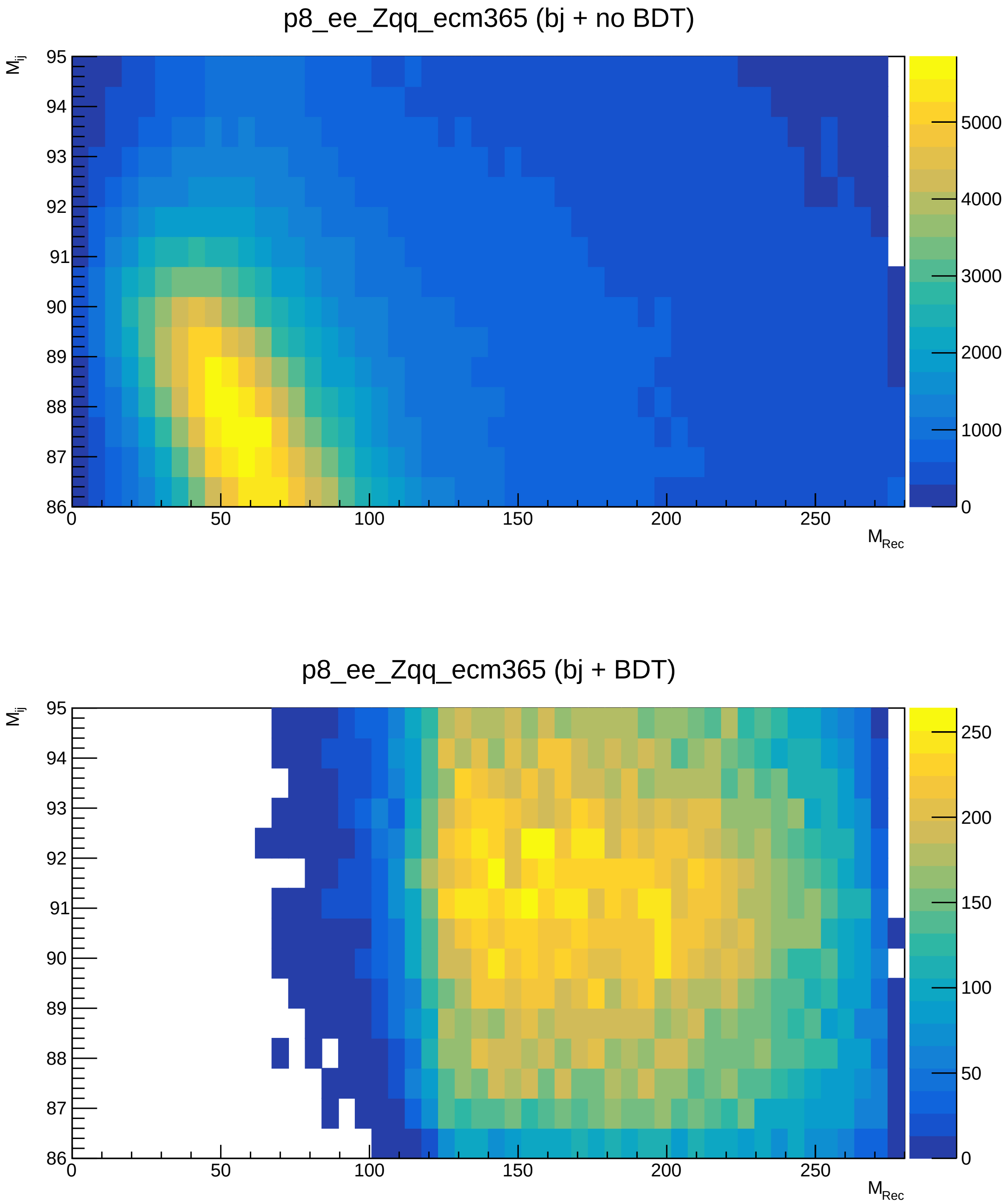


Figure 38: A 2D distribution with the recoil mass $M_{\text{Rec}} \in [0, 170]$ GeV on the x axis and the di-jet mass $M_{ij} \in [86, 96]$ GeV on the y axis. Both plots show the `PYTHIA8` $Z \to q\bar{q}$ background sample where $q, \bar{q} \in \{b, j\}$.

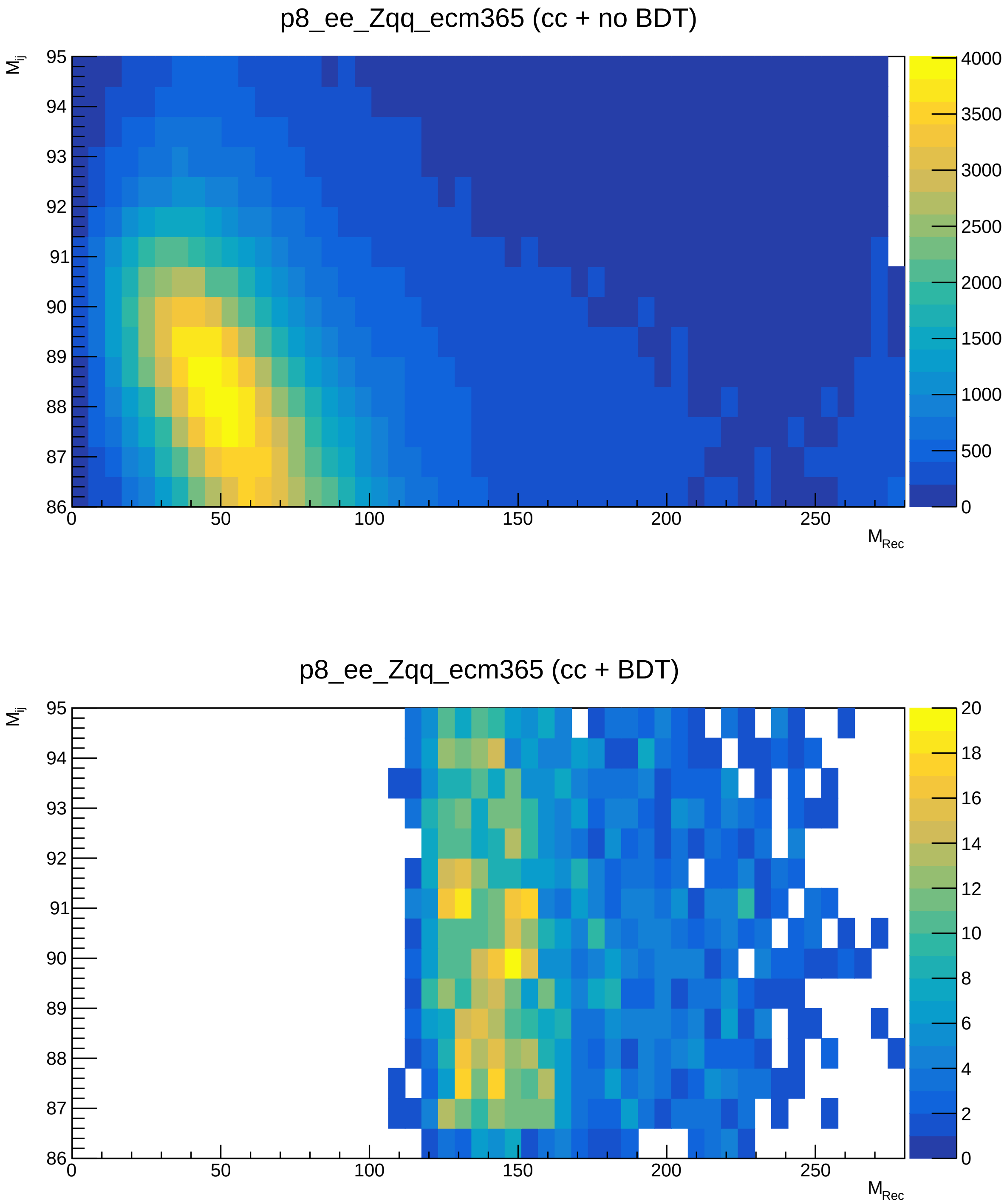


Figure 39: A 2D distribution with the recoil mass $M_{\text{Rec}} \in [0, 170]$ GeV on the x axis and the di-jet mass $M_{ij} \in [86, 96]$ GeV on the y axis. Both plots show the `PYTHIA8` $Z \to q\bar{q}$ background sample where $q, \bar{q} = c$.

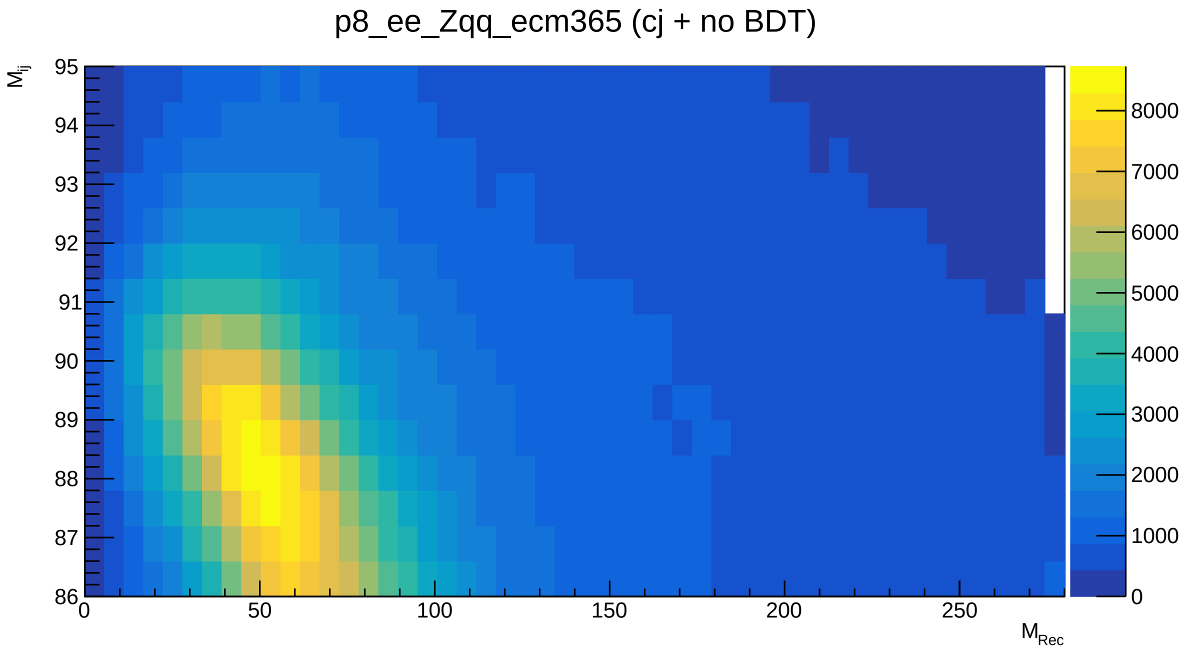


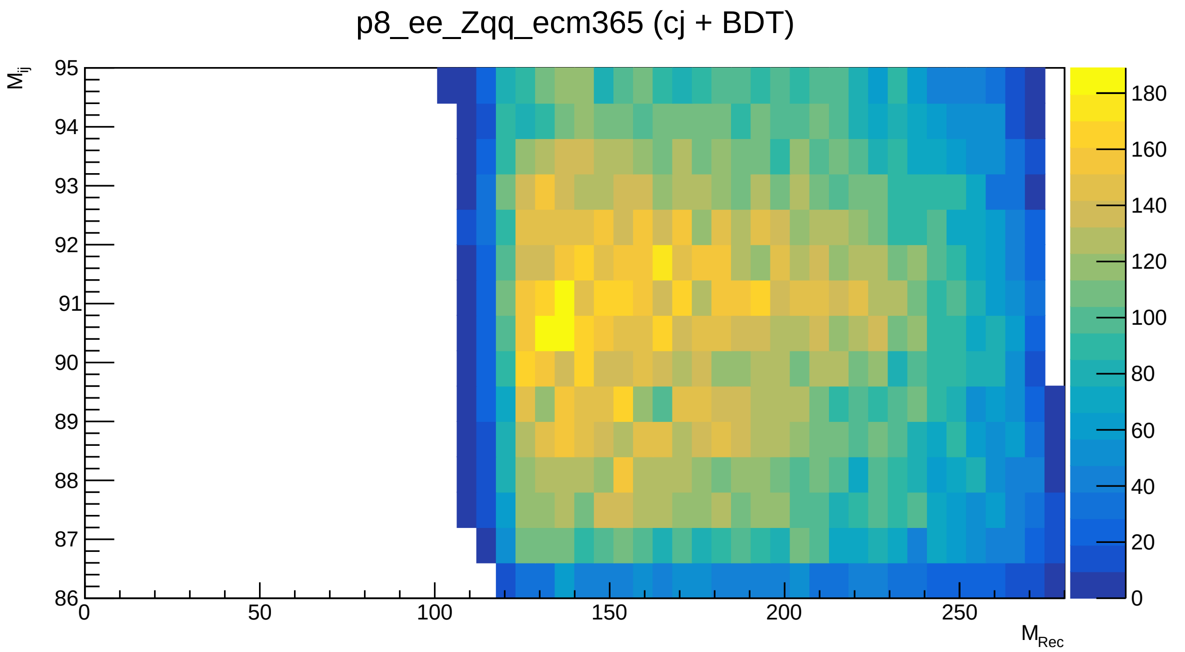


Figure 40: A 2D distribution with the recoil mass $M_{\text{Rec}} \in [0, 170]$ GeV on the x axis and the di-jet mass $M_{ij} \in [86, 96]$ GeV on the y axis. Both plots show the `PYTHIA8` $Z \to q\bar{q}$ background sample where $q, \bar{q} \in \{c, j\}$.

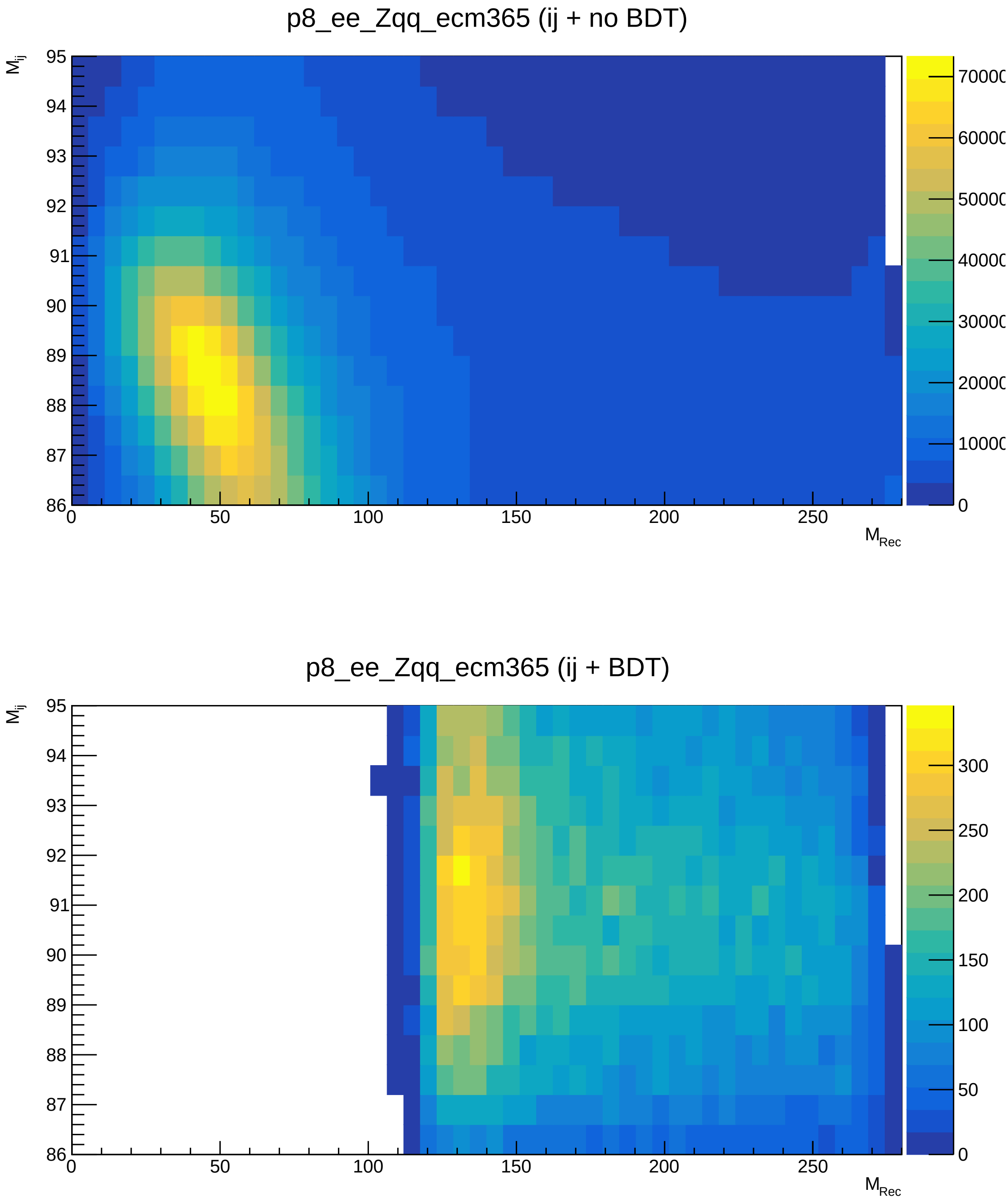


Figure 41: A 2D distribution with the recoil mass $M_{\mathrm{Rec}} \in [0, 170]$ GeV on the x axis and the di-jet mass $M_{ij} \in [86, 96]$ GeV on the y axis. Both plots show the `PYTHIA8` $Z \to q\bar{q}$ background sample where $q, \bar{q} \in \{i, j\}$.

# F BDT configurations

In the following chapter, we discuss the BDT configurations (input variable distributions, correlations and response curves) for each channel in more detail. The BDTs were trained for processes at both 240 GeV and 365 GeV to reduce the background (especially coming from $e^+e^- \to Z(q\bar{q})$ and vector boson production). Over the course of this work 14 BDTs were created (twelve for hadronic ZH, one for charged VBF and one for neutral VBF). For each BDT a learning rate of $\beta_{\text{ada}} = 0.1$ was used to train 800 trees with a minimum node size of 1% and with a maximum depth of the trees of 3. Globally, the Gini index [44] was used as a decision metric. The choice of the input variables largely depends on the channel at hand and what distribution is considered.

## F.1 $\sqrt{s} = 240$ GeV

### $e^+e^- \to Z(b\bar{b})H$

In total 16 input variables were used to train the BDT which are mostly related to the Z system. The most discriminative variable is the number of $b$-jets in the final state (see table 20). We used 20'000 signal events and 120'000 background events for training the BDT. To determine the cut on the final BDT classifier, we used the maximum of the significance distribution ($S/\sqrt{S+B}$, Fig. 44) which is calculated with 31'651 signal events and 298'464 background events in mind (number of events before applying any BDT cut).

| Rank | Variable | Rank | Variable |
|---|---|---|---|
| 1 | $N_{\text{bjets}}$ | 9 | $\theta_{bb}$ |
| 2 | $M_{bb}$ | 10 | Acollinearity of jets |
| 3 | $N_{\text{jets}}$ | 11 | $p_{T,bb}$ |
| 4 | $M_{\text{Rec}}$ | 12 | $\cos(\theta_{\text{miss}})$ |
| 5 | MET | 13 | $p_{\text{T,b,2}}$ |
| 6 | $\text{H}_T$ | 14 | $\Delta\phi(bb)$ |
| 7 | $E_{\text{j,2}}$ | 15 | $p_{\text{T,b,1}}$ |
| 8 | $E_{\text{j,1}}$ | 16 | $\Delta\eta(bb)$ |

Table 20: The ranking of the input variables according to their separation power. The highest ranked variable corresponds to the most discriminative variable.

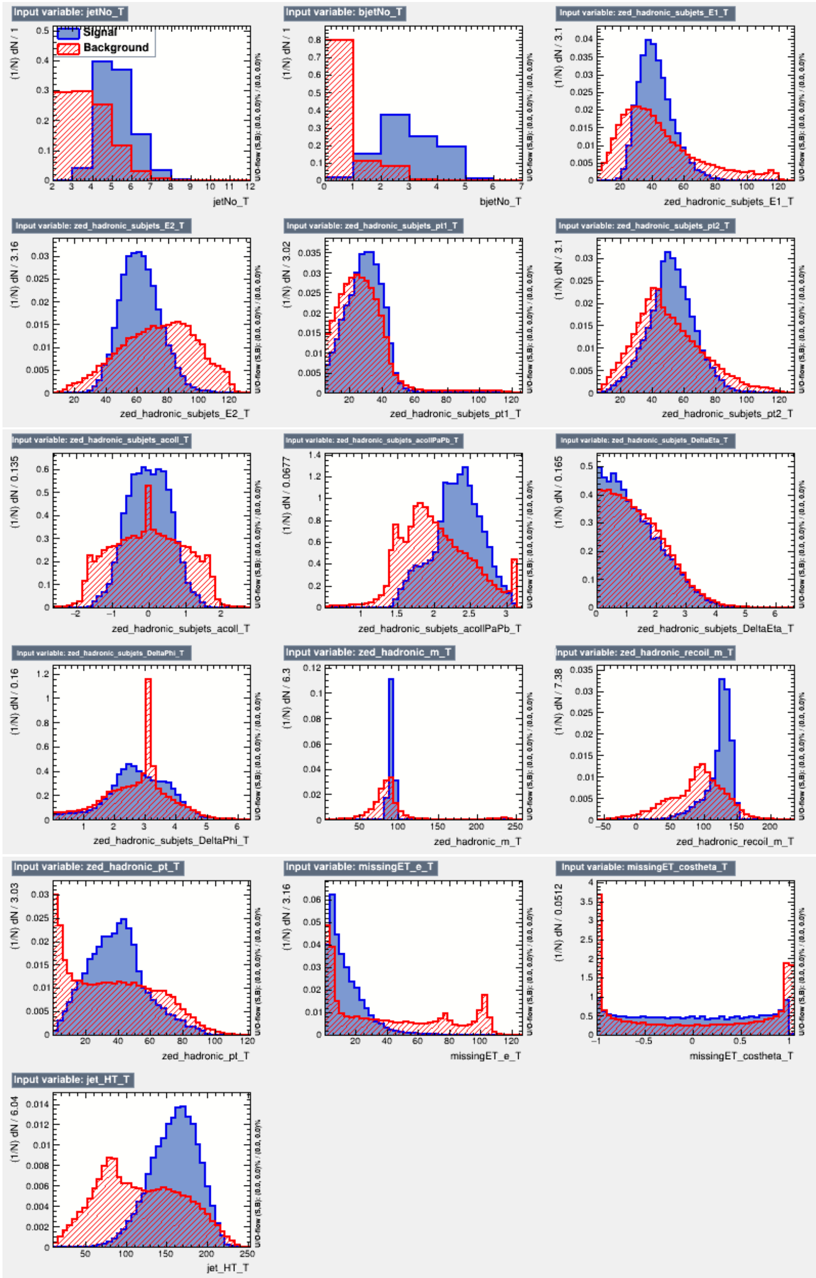

Figure 42: The input variable distributions for the $bbH$-BDT at 240 GeV.

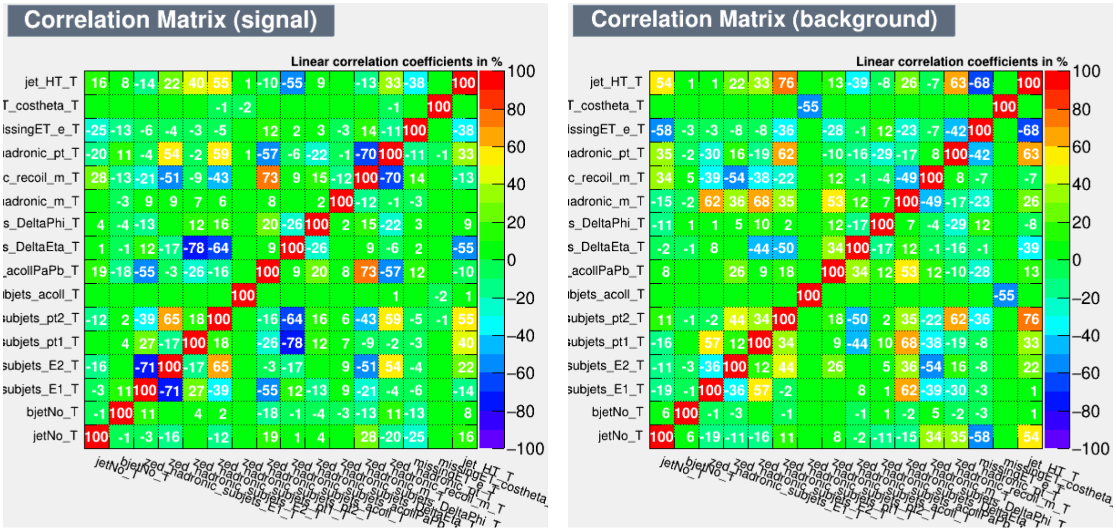


Figure 43: (a): Correlation matrix based on events from the signal sample. (b): Correlation matrix based on events from the background samples.

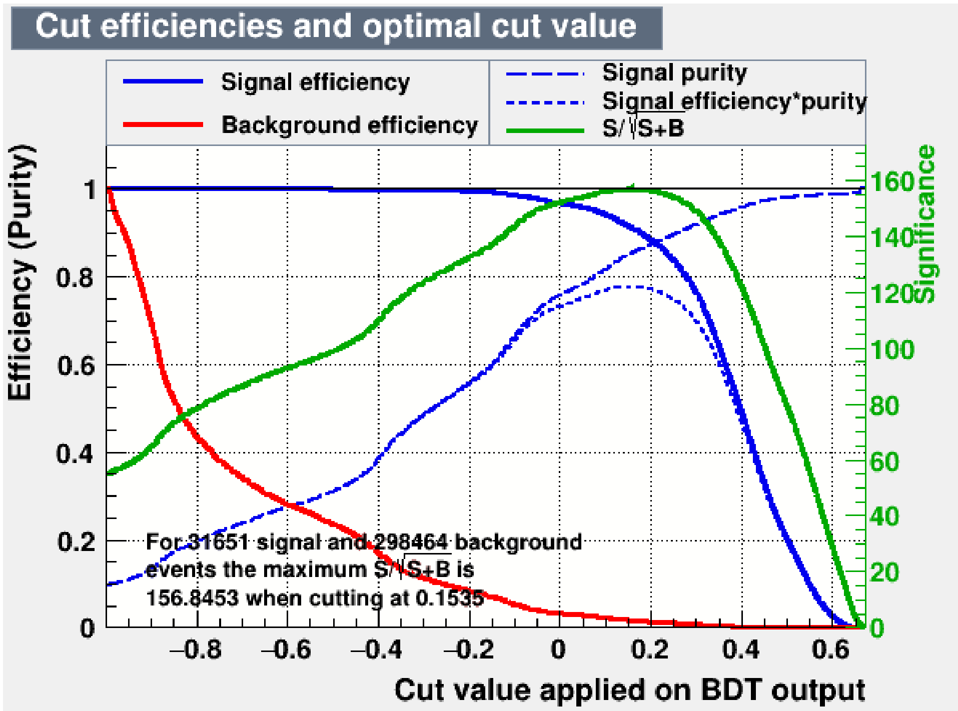


Figure 44: Significance as a function of the final BDT classifier. The significance function is based on 31’651 signal events and 298’464 background events.

### $e^+e^- \rightarrow Z(b\bar{c})H$

In total 18 input variables were used to train the BDT which are mostly related to the Z system. The most discriminative variable is the number of *b*-jets in the final state (see table 21). We used 20'000 signal events and 120'000 background events for training the BDT. To determine the cut on the final BDT classifier, we used the maximum of the significance distribution ($S/\sqrt{S+B}$, Fig. 47) which is calculated with 15'973 signal events and 369'666 background events in mind (number of events before applying any BDT cut).

| Rank | Variable | Rank | Variable |
|---|---|---|---|
| 1 | $N_{\text{bjets}}$ | 10 | $b$ Jet flag 1 |
| 2 | $M_{bc}$ | 11 | $\cos(\theta_{\text{miss}})$ |
| 3 | $N_{\text{jets}}$ | 12 | $p_{T,bc}$ |
| 4 | $\text{H}_T$ | 13 | $p_{\text{T,j,2}}$ |
| 5 | MET | 14 | $\theta_{bc}$ |
| 6 | $b$ Jet flag 2 | 15 | Acollinearity of Jets |
| 7 | $E_{\text{j,2}}$ | 16 | $\Delta\phi(bc)$ |
| 8 | $E_{\text{j,1}}$ | 17 | $p_{\text{T,j,1}}$ |
| 9 | $M_{\text{Rec}}$ | 18 | $\Delta\eta(bc)$ |

Table 21: The ranking of the input variables according to their separation power. The highest ranked variable corresponds to the most discriminative variable.

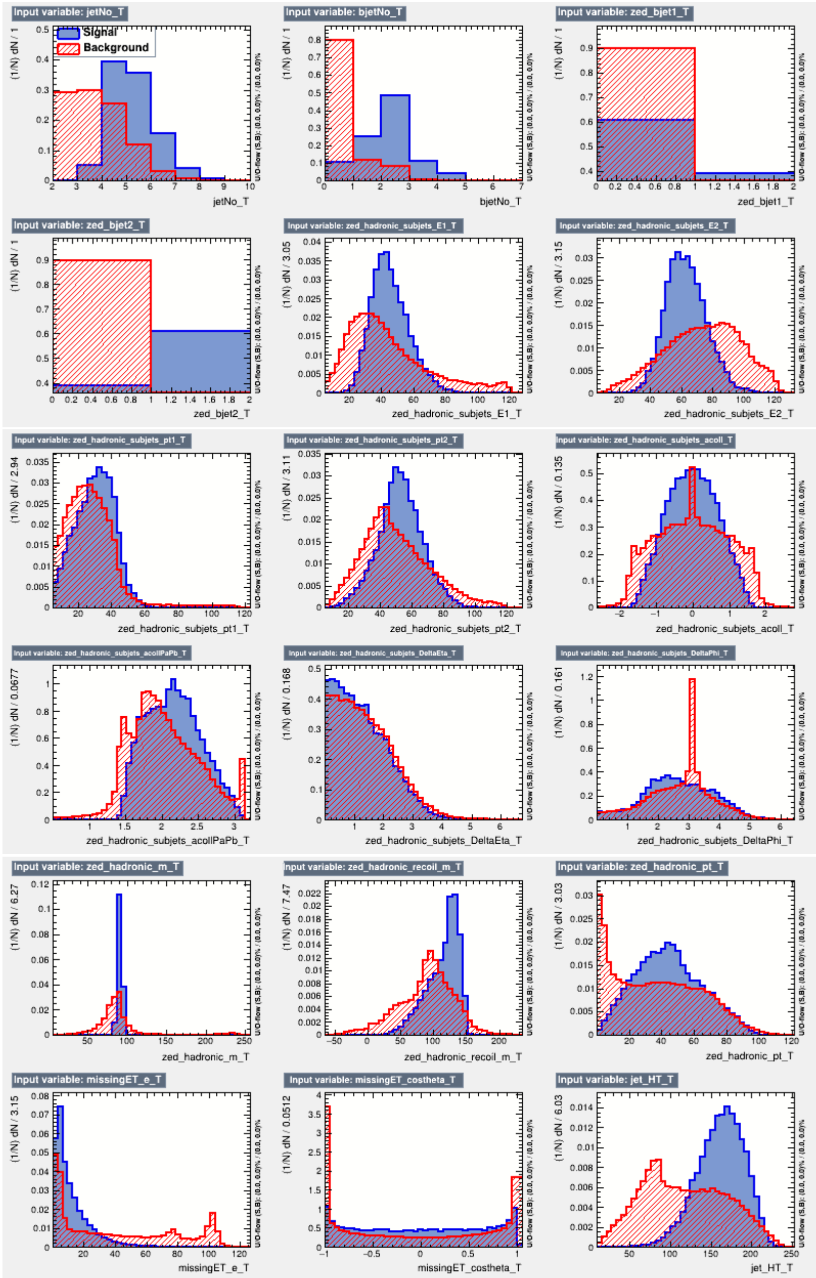


Figure 45: The input variable distributions for the $bcH$-BDT at 240 GeV.

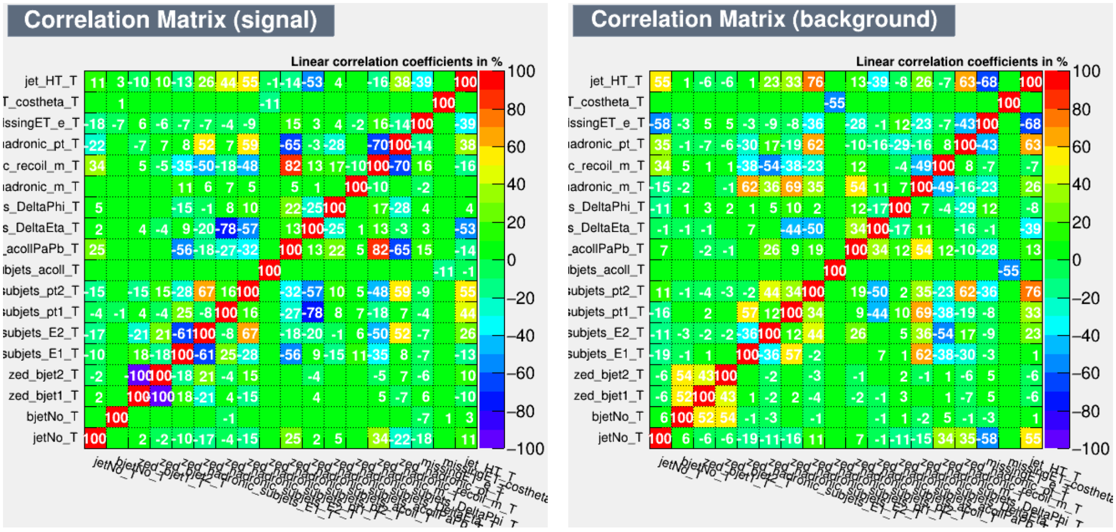


Figure 46: (a): Correlation matrix based on events from the signal sample. (b): Correlation matrix based on events from the background samples.

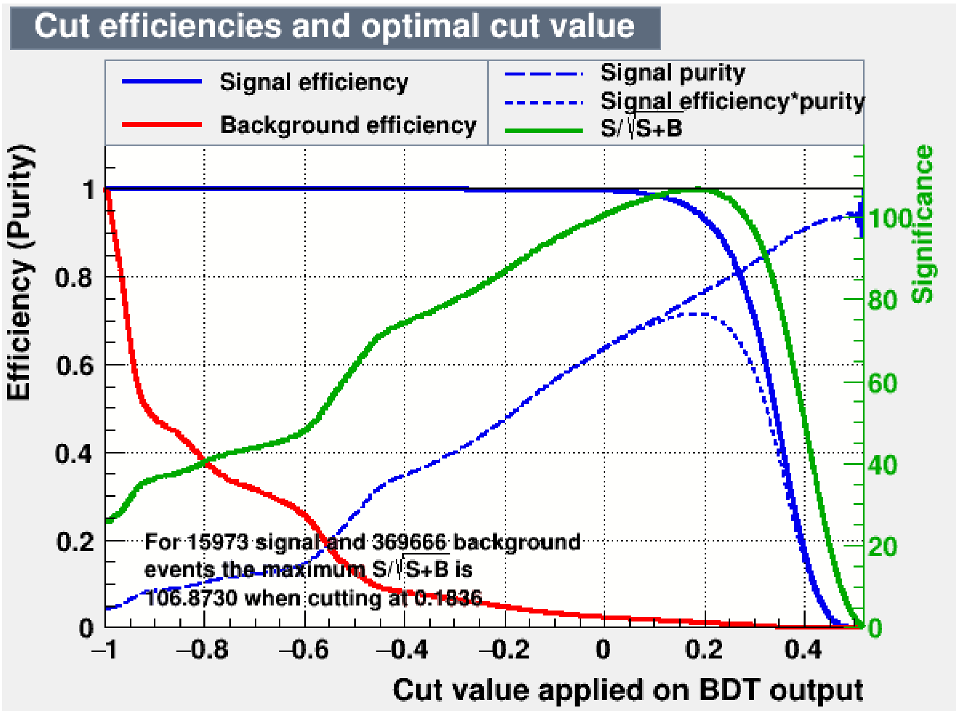


Figure 47: Significance as a function of the final BDT classifier. The significance function is based on 15’973 signal events and 369’666 background events.

### $e^+e^- \rightarrow Z(b\bar{j})H$

In total 18 input variables were used to train the BDT which are mostly related to the Z system. The most discriminative variable is the number of $b$-jets in the final state (see table 22). We used 20'000 signal events and 120'000 background events for training the BDT. To determine the cut on the final BDT classifier, we used the maximum of the significance distribution ($S/\sqrt{S+B}$, Fig. 50) which is calculated with 77'962 signal events and 4'575'436 background events in mind (number of events before applying any BDT cut).

| Rank | Variable | Rank | Variable |
|---|---|---|---|
| 1 | $N_{\mathrm{bjets}}$ | 10 | $\cos(\theta_{\mathrm{miss}})$ |
| 2 | $M_{bj}$ | 11 | $b$ Jet flag 1 |
| 3 | $N_{\mathrm{jets}}$ | 12 | $p_{T,bj}$ |
| 4 | $\mathrm{H}_T$ | 13 | $p_{\mathrm{T,j,2}}$ |
| 5 | $b$ Jet flag 2 | 14 | $\theta_{bc}$ |
| 6 | MET | 15 | Acollinearity of Jets |
| 7 | $E_{\mathrm{j,2}}$ | 16 | $\Delta\phi(bj)$ |
| 8 | $E_{\mathrm{j,1}}$ | 17 | $p_{\mathrm{T,j,1}}$ |
| 9 | $M_{\mathrm{Rec}}$ | 18 | $\Delta\eta(bj)$ |

Table 22: The ranking of the input variables according to their separation power. The highest ranked variable corresponds to the most discriminative variable.

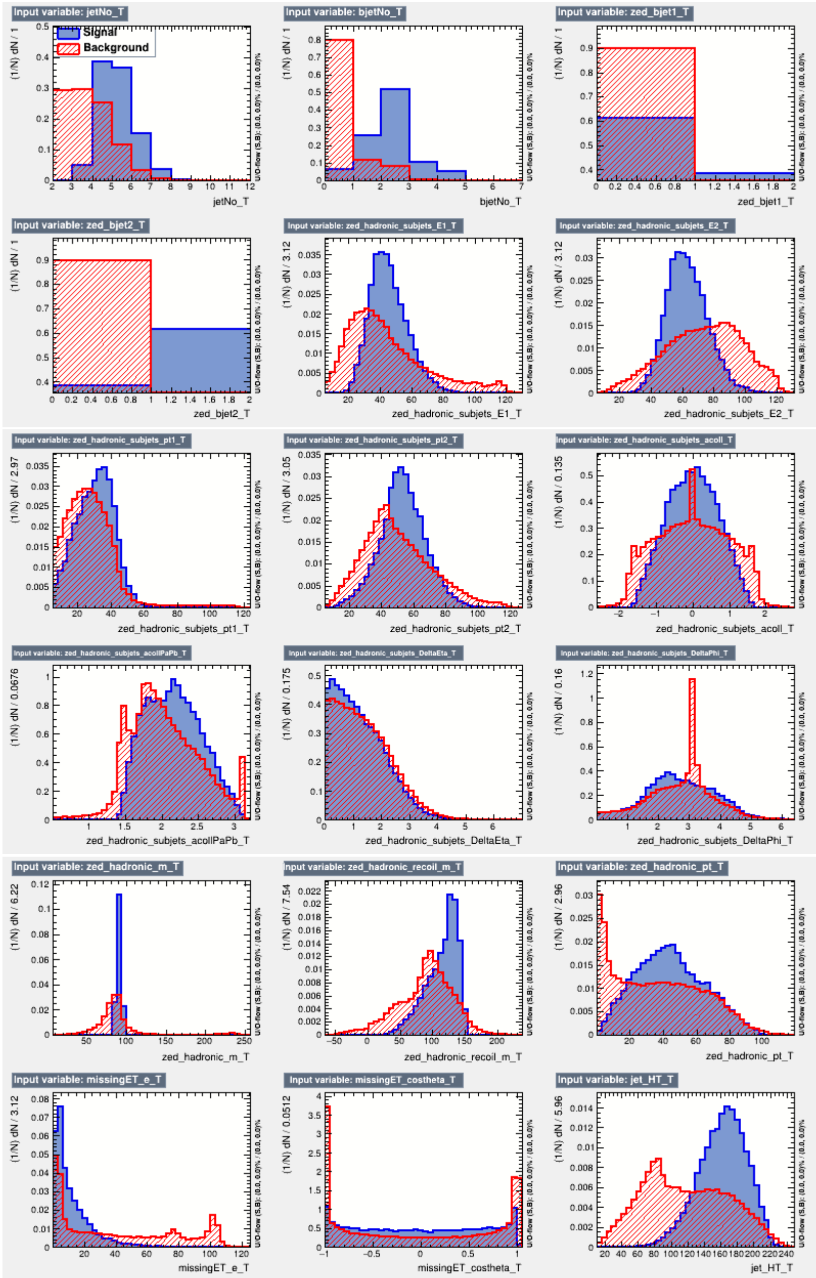


Figure 48: The input variable distributions for the $bjH$-BDT at 240 GeV.

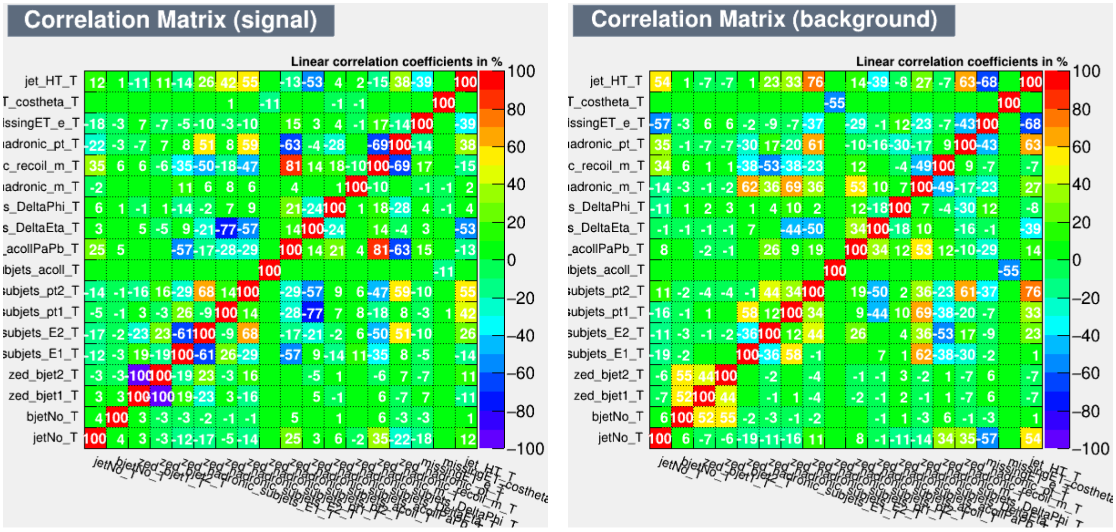


Figure 49: (a): Correlation matrix based on events from the signal sample. (b): Correlation matrix based on events from the background samples.

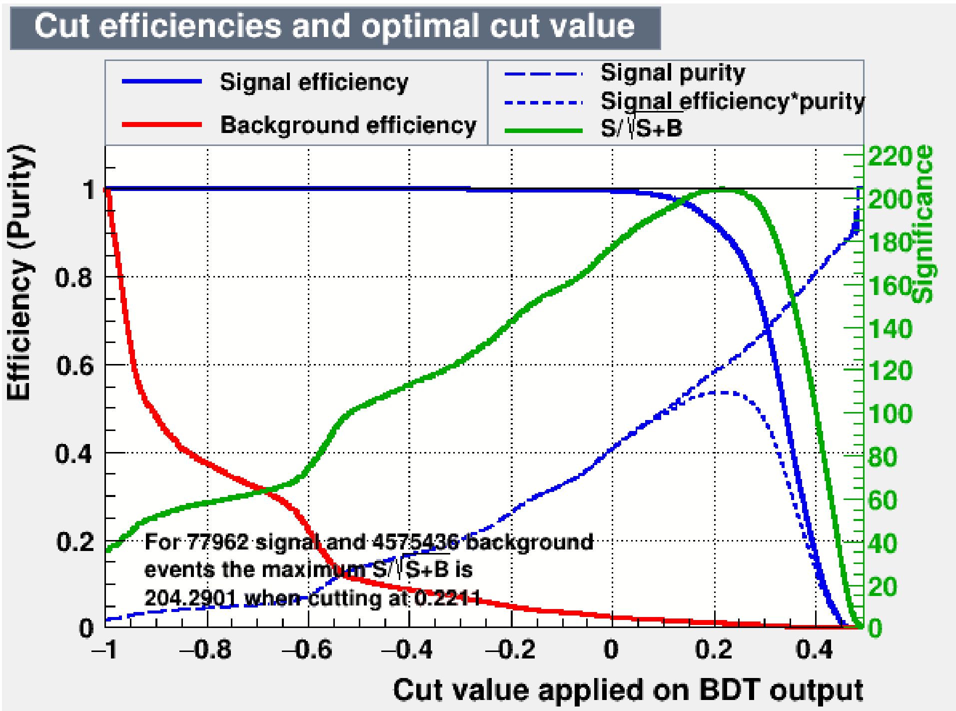


Figure 50: Significance as a function of the final BDT classifier. The significance function is based on 77’962 signal events and 4’575’436 background events.

### $e^+e^- \to Z(c\bar{c})H$

In total 17 input variables were used to train the BDT which are mostly related to the Z system. The most discriminative variable is the recoil mass (see table 23). We used 10'000 signal events and 120'000 background events for training the BDT. To determine the cut on the final BDT classifier, we used the maximum of the significance distribution ($S/\sqrt{S+B}$, Fig. 53) which is calculated with 7'669 signal events and 2'440'009 background events in mind (number of events before applying any BDT cut).

| Rank | Variable | Rank | Variable |
|---|---|---|---|
| 1 | $M_{\text{Rec}}$ | 10 | MET |
| 2 | $M_{cc}$ | 11 | $\theta_{cc}$ |
| 3 | $N_{\text{cjets}}$ | 12 | $N_{\text{bjets}}$ |
| 4 | $N_{\text{jets}}$ | 13 | $\cos(\theta_{\text{miss}})$ |
| 5 | Acollinearity of Jets | 14 | $p_{\text{T,j,2}}$ |
| 6 | $E_{\text{j,2}}$ | 15 | $\Delta\phi(cc)$ |
| 7 | $\text{H}_T$ | 16 | $p_{\text{T,j,1}}$ |
| 8 | $p_{T,cc}$ | 17 | $\Delta\eta(cc)$ |
| 9 | $E_{\text{j,1}}$ | | |

Table 23: The ranking of the input variables according to their separation power. The highest ranked variable corresponds to the most discriminative variable.

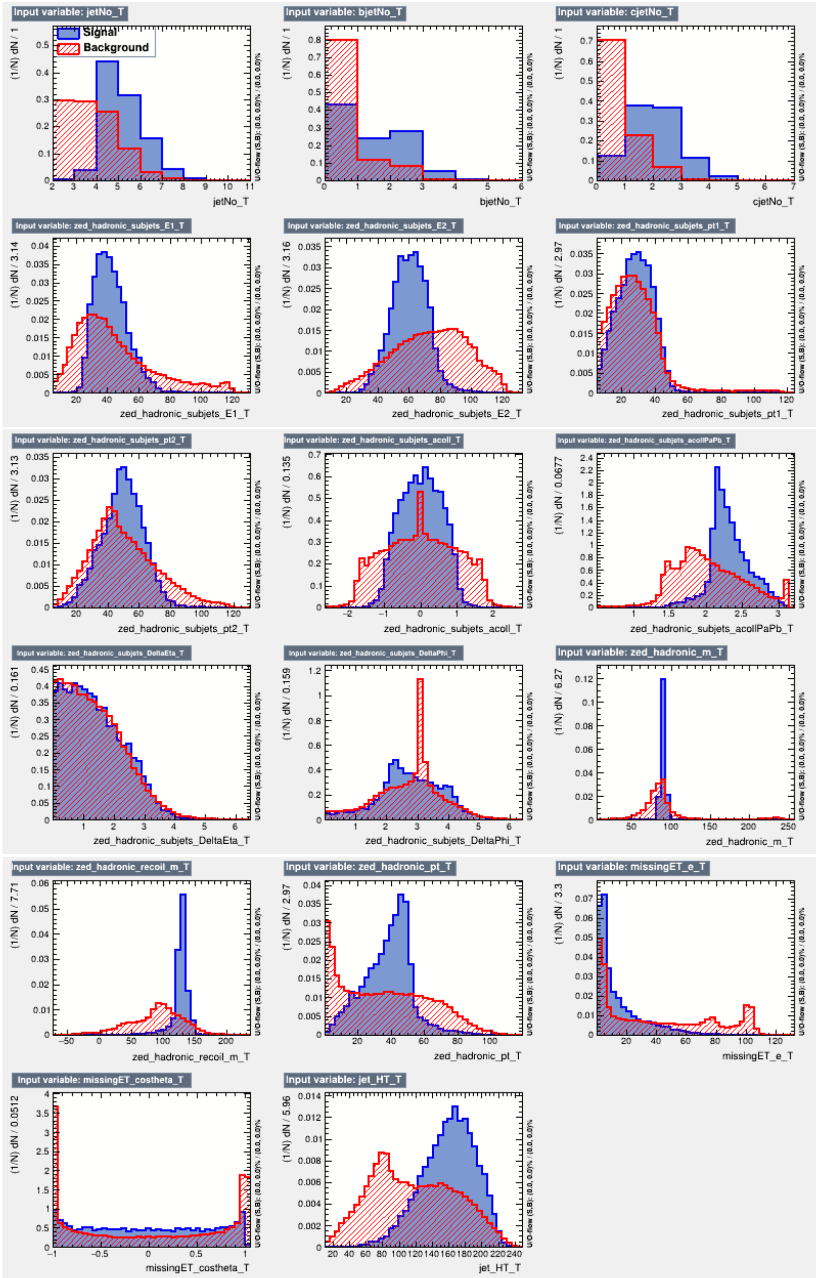


Figure 51: The input variable distributions for the $ccH$-BDT at 240 GeV.

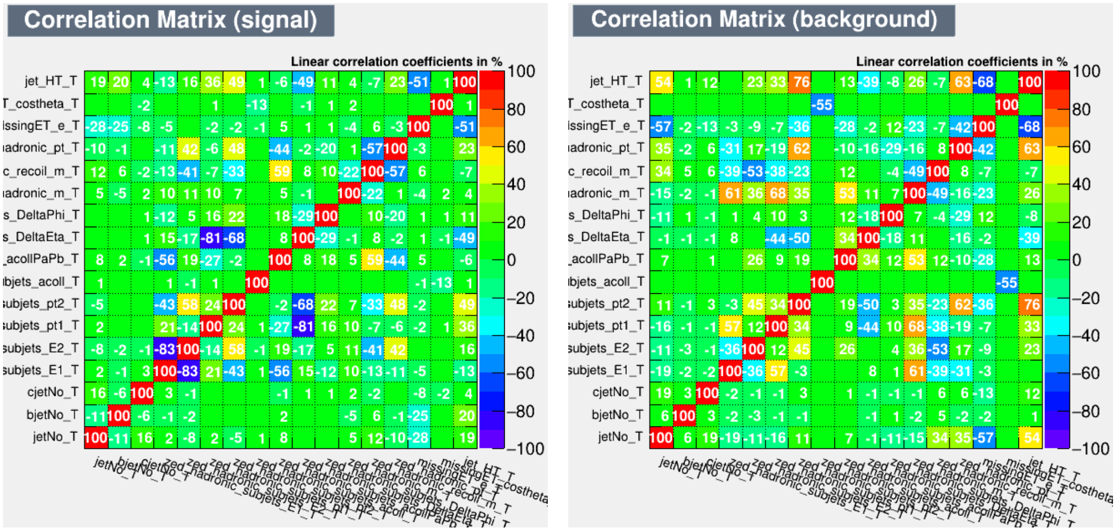


Figure 52: (a): Correlation matrix based on events from the signal sample. (b): Correlation matrix based on events from the background samples.

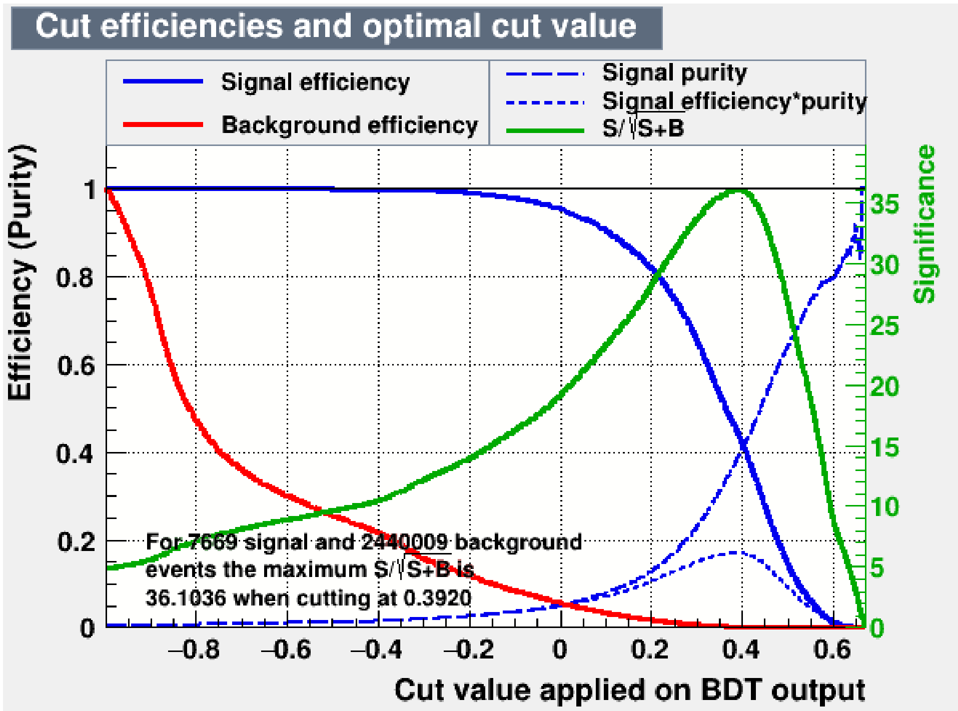


Figure 53: Significance as a function of the final BDT classifier. The significance function is based on 7'669 signal events and 2'440'009 background events.

## $e^+e^- \rightarrow Z(c\bar{j})H$

In total 19 input variables were used to train the BDT which are mostly related to the Z system. The most discriminative variable is the dijet mass (see table 24). We used 20'000 signal events and 120'000 background events for training the BDT. To determine the cut on the final BDT classifier, we used the maximum of the significance distribution ($S/\sqrt{S+B}$, Fig. 56) which is calculated with 28'694 signal events and 9'305'606 background events in mind (number of events before applying any BDT cut).

| Rank | Variable | Rank | Variable |
|---|---|---|---|
| 1 | $M_{cj}$ | 11 | $c$ Jet flag 1 |
| 2 | $N_{\text{jets}}$ | 12 | $p_{T,cj}$ |
| 3 | $M_{\text{Rec}}$ | 13 | $\theta_{cj}$ |
| 4 | $\text{H}_T$ | 14 | $\cos(\theta_{\text{miss}})$ |
| 5 | $E_{\text{j,2}}$ | 15 | $p_{\text{T,j,2}}$ |
| 6 | MET | 16 | $N_{\text{bjets}}$ |
| 7 | $N_{\text{cjets}}$ | 17 | $\Delta\phi(cj)$ |
| 8 | $E_{\text{j,1}}$ | 18 | $p_{\text{T,j,1}}$ |
| 9 | $c$ Jet flag 2 | 19 | $\Delta\eta(cj)$ |
| 10 | Acollinearity of Jets | | |

Table 24: The ranking of the input variables according to their separation power. The highest ranked variable corresponds to the most discriminative variable.

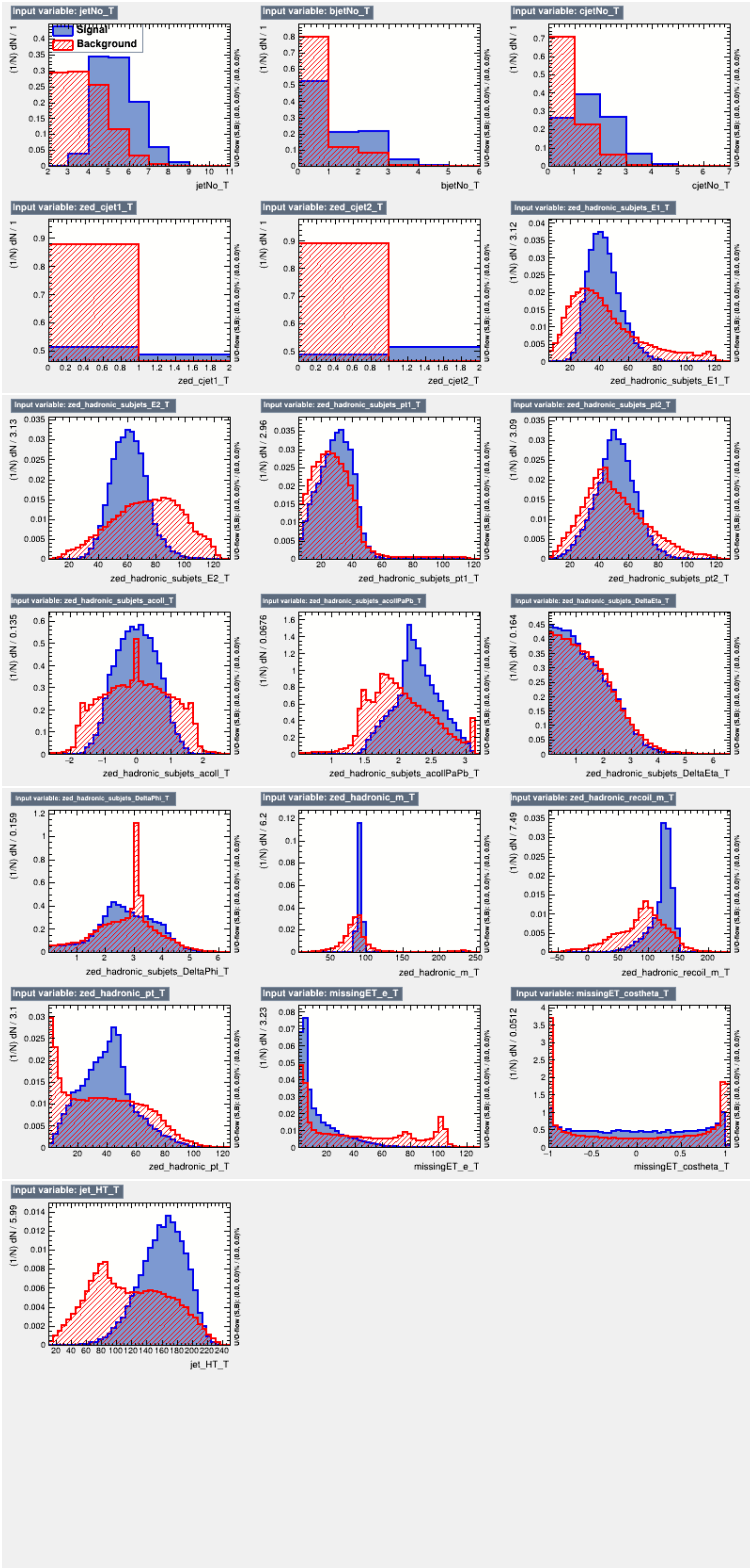

Figure 54: The input variable distributions for the $cjH$-BDT at 240 GeV.

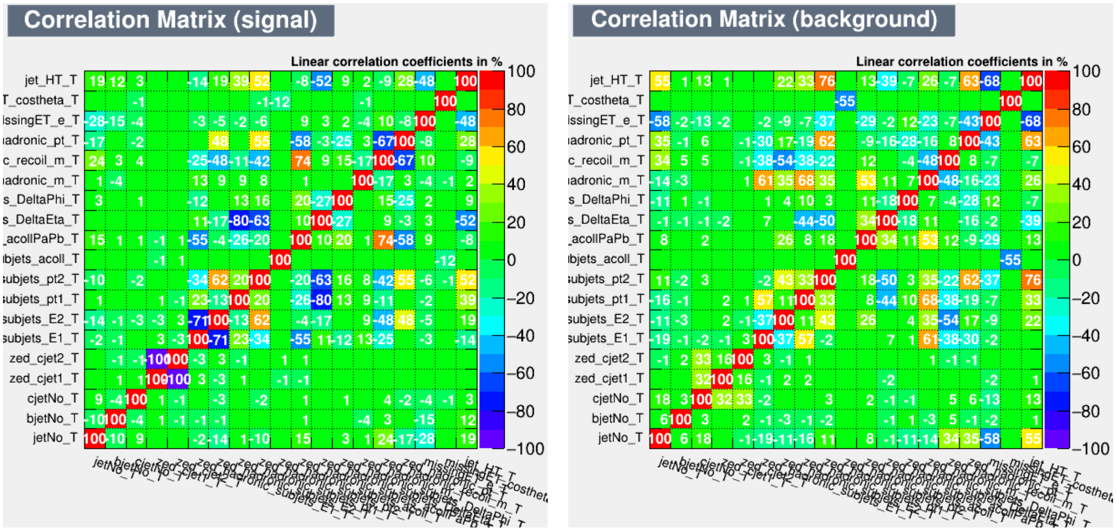


Figure 55: (a): Correlation matrix based on events from the signal sample. (b): Correlation matrix based on events from the background samples.

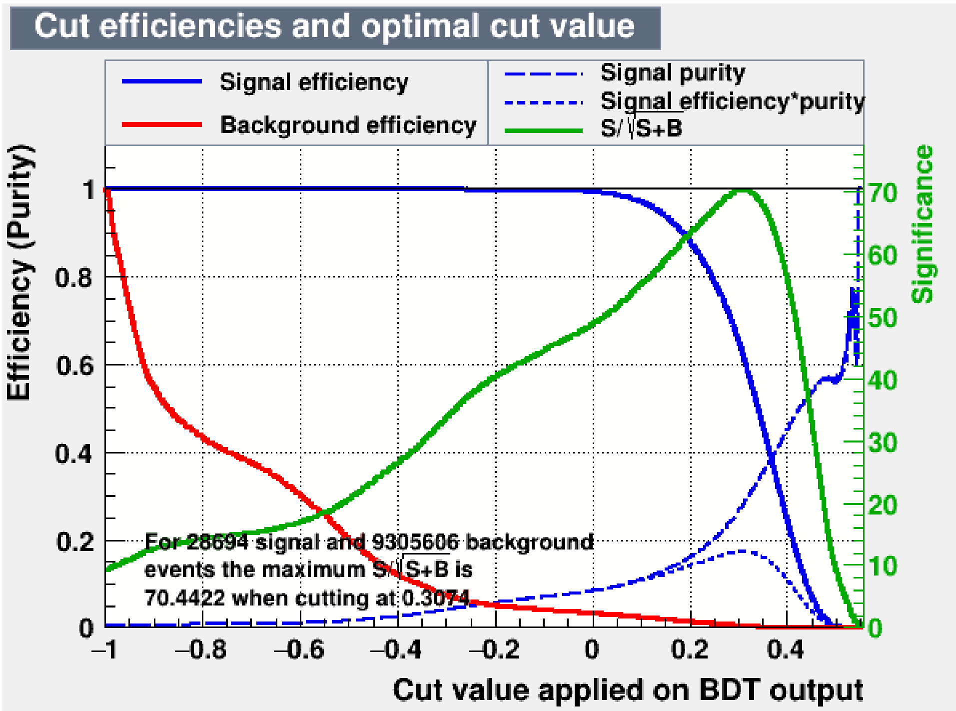


Figure 56: Significance as a function of the final BDT classifier. The significance function is based on 28’694 signal events and 9’305’606 background events.

### $e^+e^- \rightarrow Z(i\bar{j})H$

In total 19 input variables were used to train the BDT which are mostly related to the Z system. The most discriminative variable is the dijet mass (see table 25). We used 20'000 signal events and 120'000 background events for training the BDT. To determine the cut on the final BDT classifier, we used the maximum of the significance distribution ($S/\sqrt{S+B}$, Fig. 59) which is calculated with 152'887 signal events and 59'154'940 background events in mind (number of events before applying any BDT cut).

| Rank | Variable | Rank | Variable |
|---|---|---|---|
| 1 | $M_{ij}$ | 11 | $\cos(\theta_{\rm miss})$ |
| 2 | $M_{\rm Rec}$ | 12 | $N_{\rm bjets}$ |
| 3 | $N_{\rm jets}$ | 13 | $p_{\rm T,j,2}$ |
| 4 | $E_{\rm j,2}$ | 14 | $\Delta\phi(ij)$ |
| 5 | $\mathrm{H}_T$ | 15 | $b$ Jet flag 2 |
| 6 | Acollinearity of Jets | 16 | $b$ Jet flag 1 |
| 7 | $E_{\rm j,1}$ | 17 | $p_{\rm T,j,1}$ |
| 8 | MET | 18 | $\Delta\eta(ij)$ |
| 9 | $p_{T,ij}$ | 19 | $N_{\rm cjets}$ |
| 10 | $\theta_{ij}$ | | |

Table 25: The ranking of the input variables according to their separation power. The highest ranked variable corresponds to the most discriminative variable.

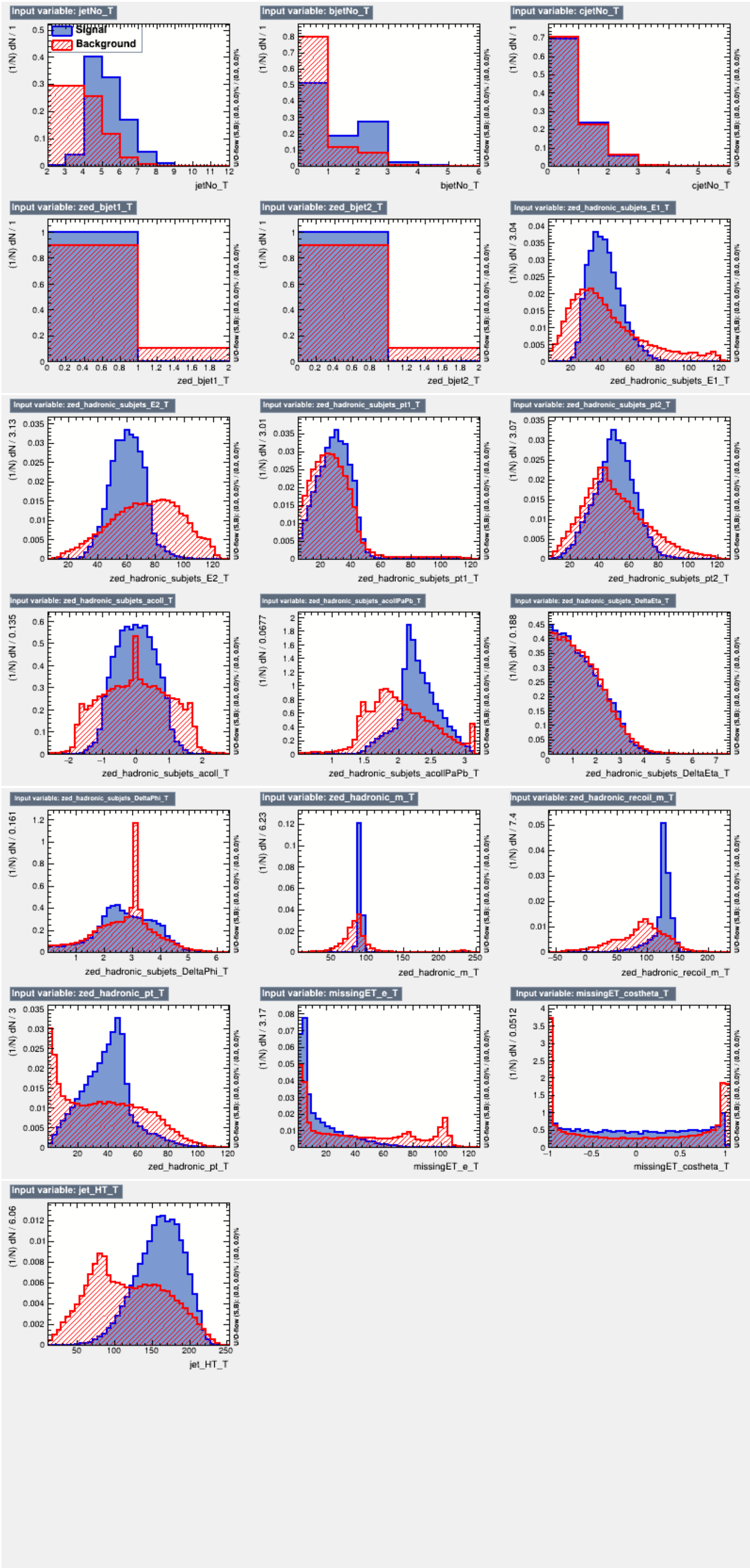

Figure 57: The input variable distributions for the $ijH$-BDT at 240 GeV.

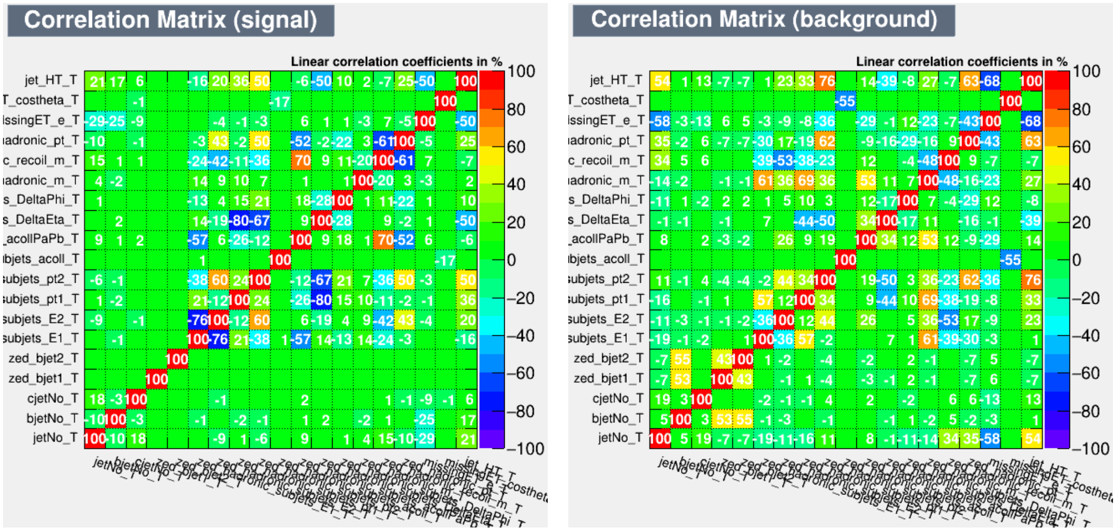


Figure 58: (a): Correlation matrix based on events from the signal sample. (b): Correlation matrix based on events from the background samples.

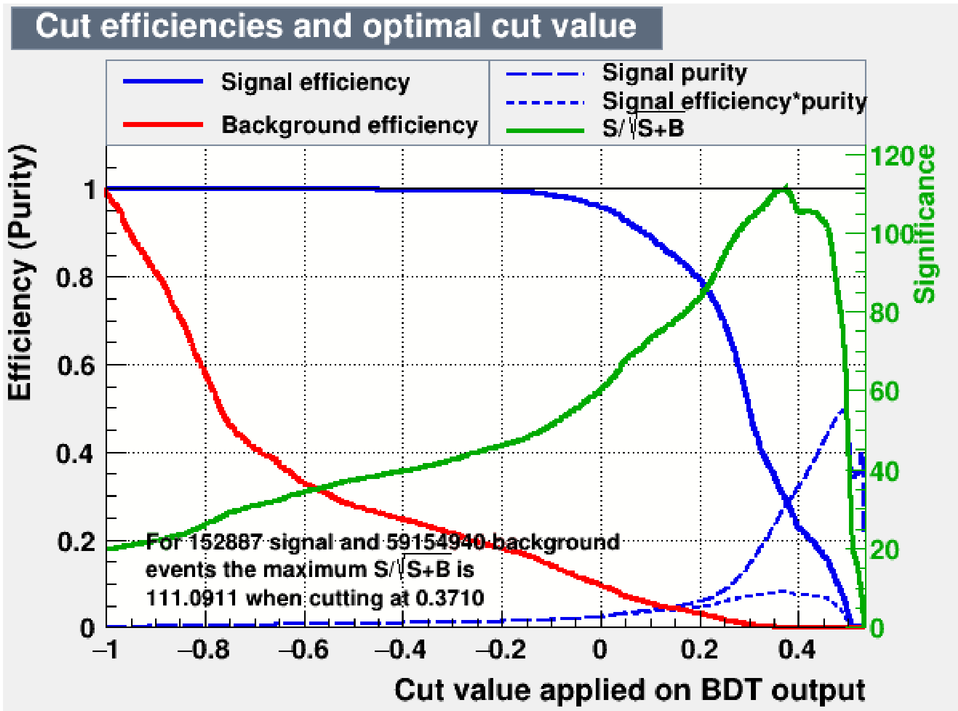


Figure 59: Significance as a function of the final BDT classifier. The significance function is based on 152'887 signal events and 59'154'940 background events.

### F.2 $\sqrt{s} = 365$ GeV

#### $e^+e^- \rightarrow Z(b\bar{b})H$

In total 16 input variables were used to train the BDT which are mostly related to the Z system. The most discriminative variable is the number of jets in the final state (see table 26). We used 20'000 signal events and 120'000 background events for training the BDT. To determine the cut on the final BDT classifier, we used the maximum of the significance distribution ($S/\sqrt{S+B}$, Fig. 62) which is calculated with 6'812 signal events and 436'189 background events in mind (number of events before applying any BDT cut).

| Rank | Variable | Rank | Variable |
|---|---|---|---|
| 1 | $N_{\text{jets}}$ | 9 | MET |
| 2 | $N_{\text{bjets}}$ | 10 | $\theta_{bb}$ |
| 3 | $\text{H}_T$ | 11 | $\cos(\theta_{\text{miss}})$ |
| 4 | $p_{T,bb}$ | 12 | Acollinearity of Jets |
| 5 | $M_{\text{Rec}}$ | 13 | $E_{\text{b},2}$ |
| 6 | $M_{bb}$ | 14 | $E_{\text{b},1}$ |
| 7 | $p_{\text{T,b,2}}$ | 15 | $p_{\text{T,b,1}}$ |
| 8 | $\Delta\phi(bb)$ | 16 | $\Delta\eta(bb)$ |

Table 26: The ranking of the input variables according to their separation power. The highest ranked variable corresponds to the most discriminative variable.

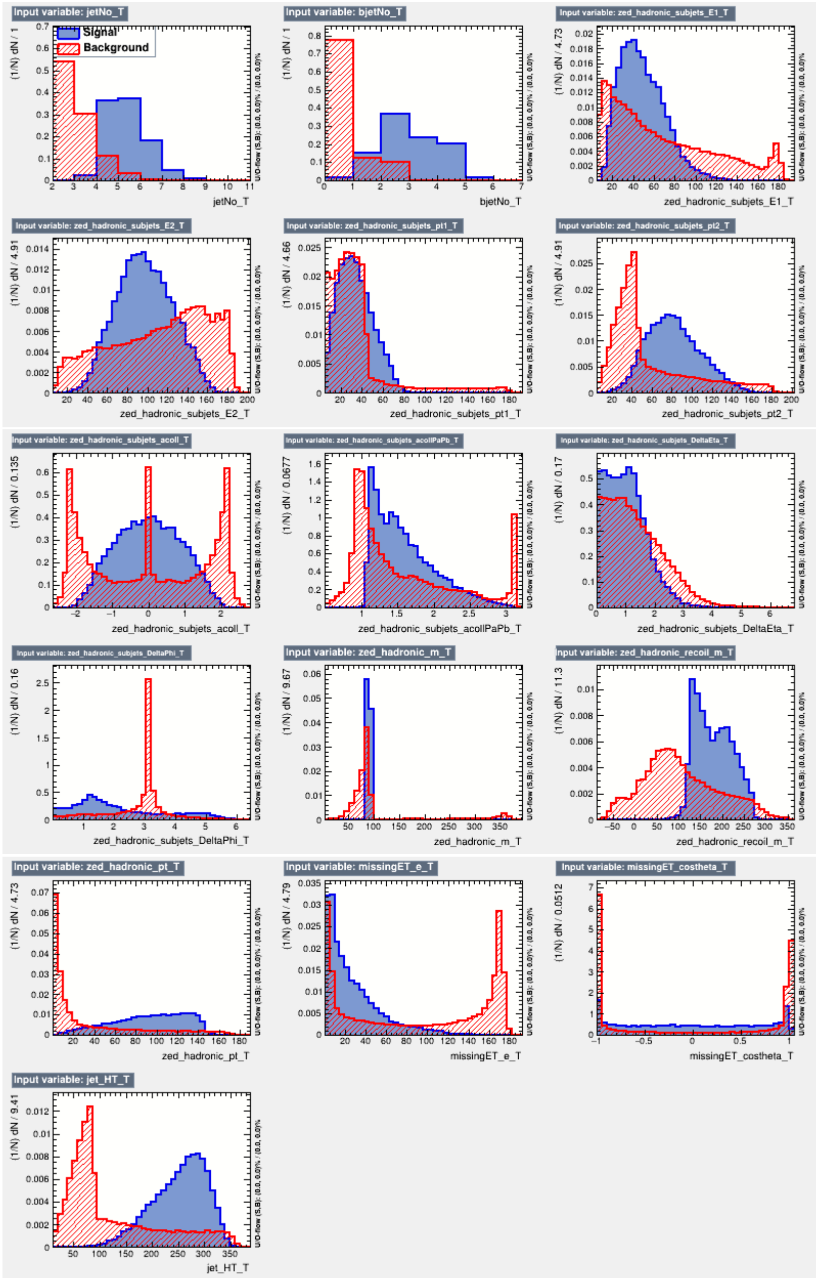

Figure 60: The input variable distributions for the $bbH$-BDT at 365 GeV.

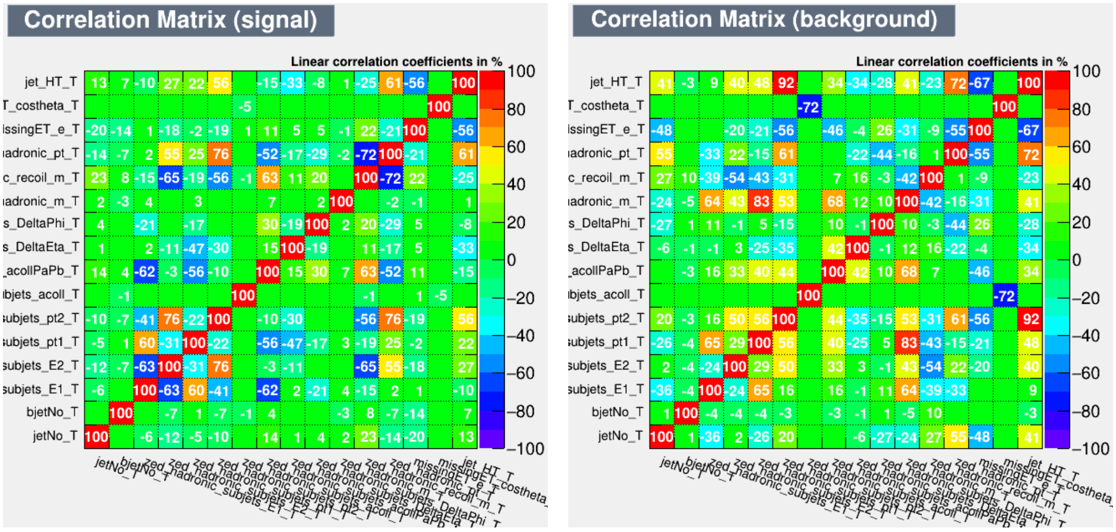


Figure 61: (a): Correlation matrix based on events from the signal sample. (b): Correlation matrix based on events from the background samples.

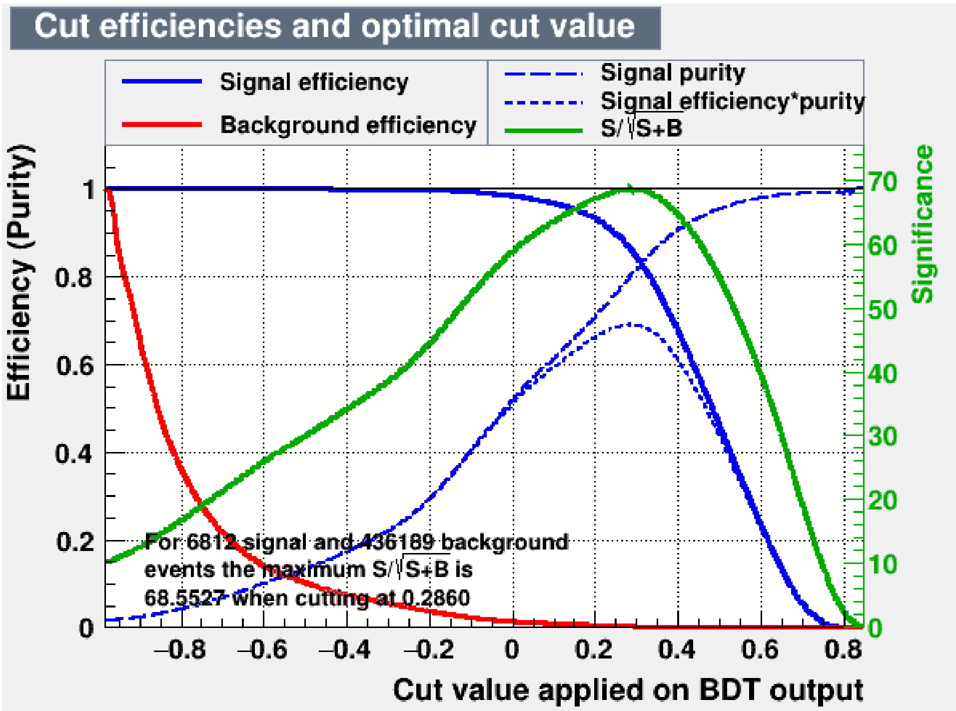


Figure 62: Significance as a function of the final BDT classifier. The significance function is based on 6'812 signal events and 436'189 background events.

### $e^+e^- \rightarrow Z(b\bar{c})H$

In total 18 input variables were used to train the BDT which are mostly related to the Z system. The most discriminative variable is the number of jets in the final state (see table 27). We used 20'000 signal events and 100'000 background events for training the BDT. To determine the cut on the final BDT classifier, we used the maximum of the significance distribution ($S/\sqrt{S+B}$, Fig. 65) which is calculated with 15'973 signal events and 369'666 background events in mind (number of events before applying any BDT cut).

| Rank | Variable | Rank | Variable |
|---|---|---|---|
| 1 | $N_{\text{jets}}$ | 10 | $\Delta\phi(bc)$ |
| 2 | $\text{H}_T$ | 11 | $\cos(\theta_{\text{miss}})$ |
| 3 | $M_{\text{Rec}}$ | 12 | Acollinearity of Jets |
| 4 | $N_{\text{bjets}}$ | 13 | $E_{\text{b},1}$ |
| 5 | $p_{T,bc}$ | 14 | $E_{\text{b},2}$ |
| 6 | $M_{bc}$ | 15 | $b$ Jet flag 2 |
| 7 | $\theta_{bc}$ | 16 | $b$ Jet flag 1 |
| 8 | MET | 17 | $p_{\text{T,j,1}}$ |
| 9 | $p_{\text{T,j,2}}$ | 18 | $\Delta\eta(bc)$ |

Table 27: The ranking of the input variables according to their separation power. The highest ranked variable corresponds to the most discriminative variable.

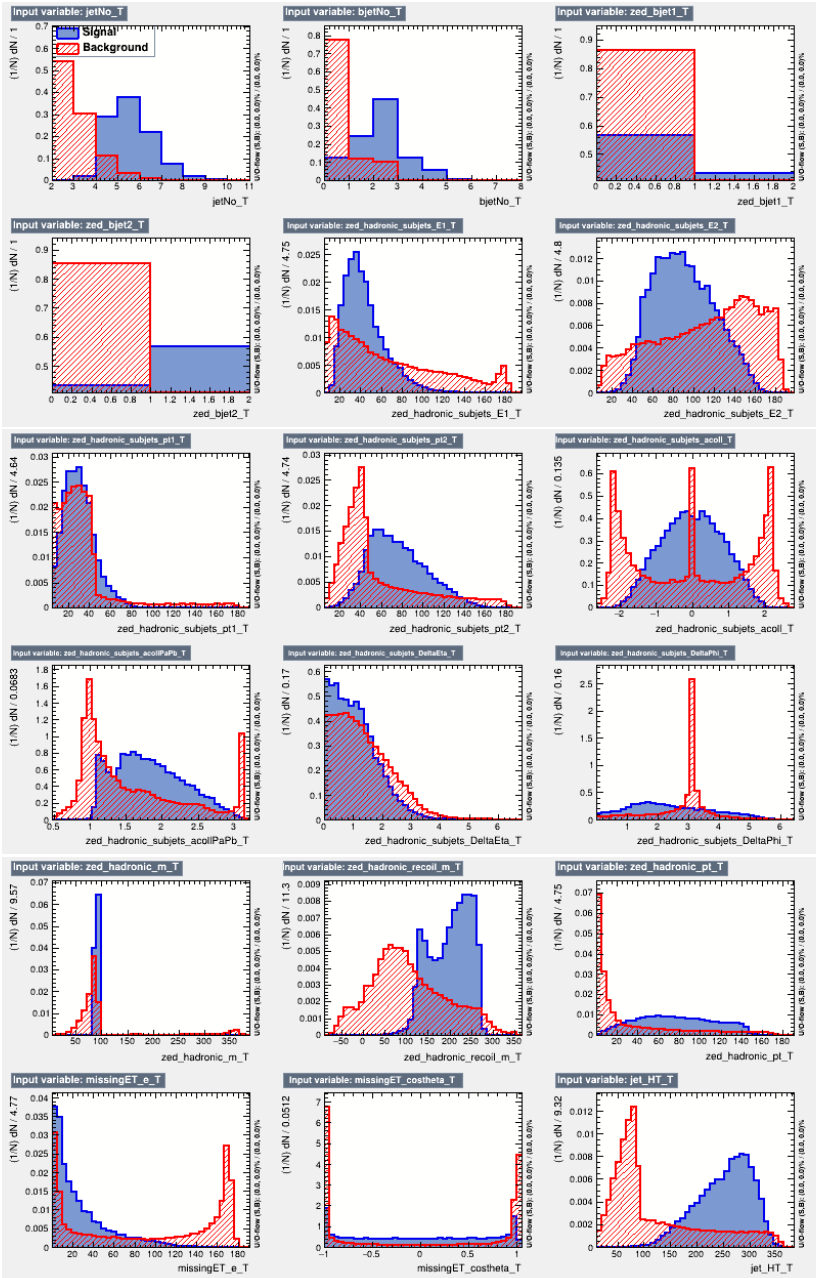

Figure 63: The input variable distributions for the $bcH$-BDT at 365 GeV.

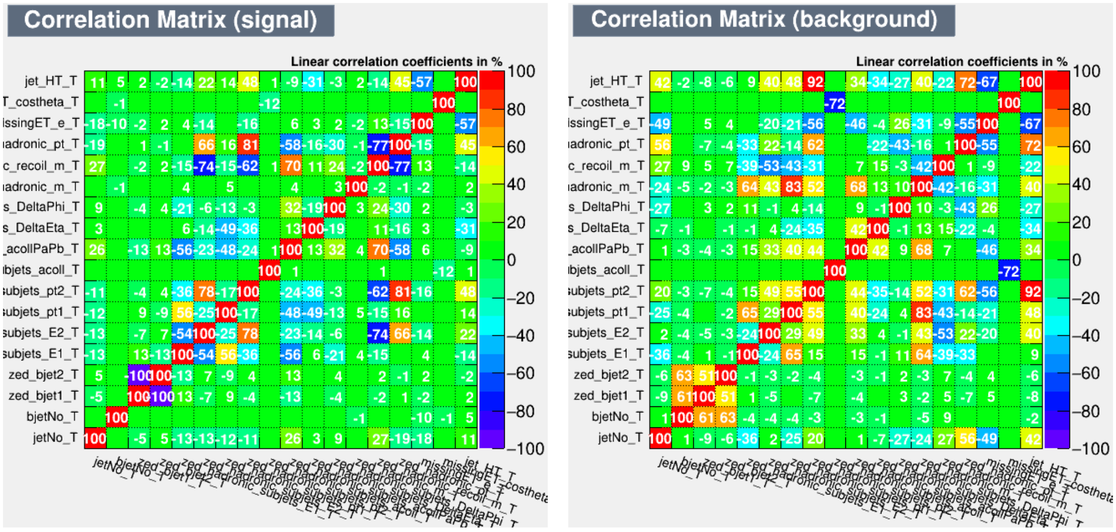


Figure 64: (a): Correlation matrix based on events from the signal sample. (b): Correlation matrix based on events from the background samples.

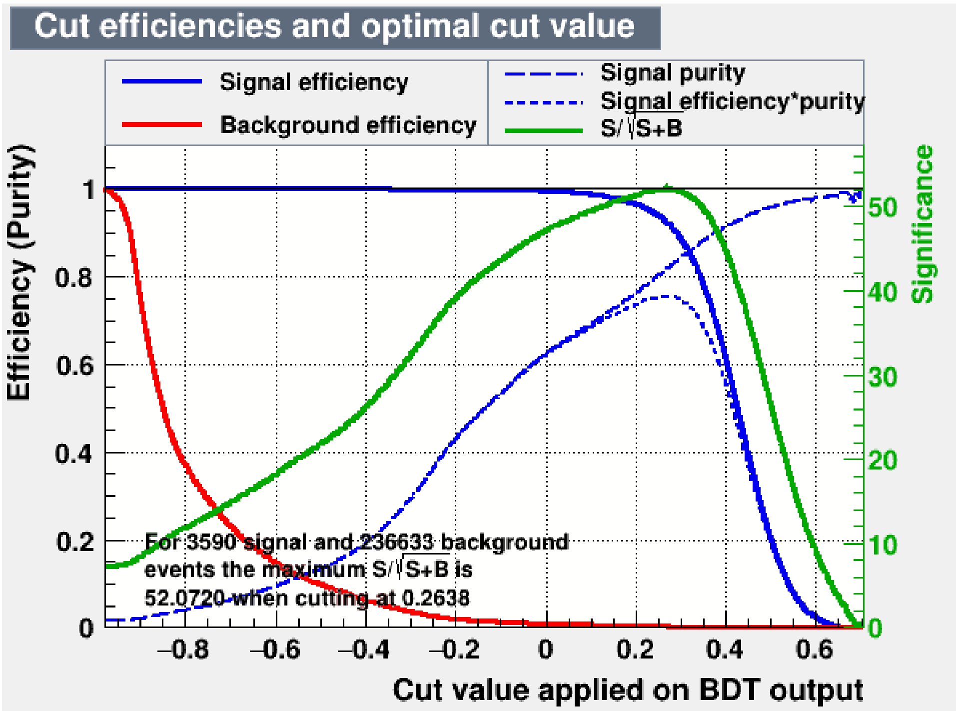


Figure 65: Significance as a function of the final BDT classifier. The significance function is based on 15’973 signal events and 369’666 background events.

### $e^+e^- \to Z(b\bar{j})H$

In total 18 input variables were used to train the BDT which are mostly related to the Z system. The most discriminative variable is the number of jets in the final state (see table 28). We used 20'000 signal events and 100'000 background events for training the BDT. To determine the cut on the final BDT classifier, we used the maximum of the significance distribution ($S/\sqrt{S+B}$, Fig. 68) which is calculated with 13'335 signal events and 635'447 background events in mind (number of events before applying any BDT cut).

| Rank | Variable | Rank | Variable |
|---|---|---|---|
| 1 | $N_{\text{jets}}$ | 10 | Acollinearity of Jets |
| 2 | $N_{\text{bjets}}$ | 11 | $\cos(\theta_{\text{miss}})$ |
| 3 | $\text{H}_T$ | 12 | $\Delta\phi(bj)$ |
| 4 | $M_{\text{Rec}}$ | 13 | $E_{\text{b,1}}$ |
| 5 | $p_{T,bj}$ | 14 | $E_{\text{b,2}}$ |
| 6 | $M_{bj}$ | 15 | $b$ Jet flag 2 |
| 7 | $\theta_{bj}$ | 16 | $b$ Jet flag 1 |
| 8 | MET | 17 | $p_{\text{T,j,1}}$ |
| 9 | $p_{\text{T,j,2}}$ | 18 | $\Delta\eta(bj)$ |

Table 28: The ranking of the input variables according to their separation power. The highest ranked variable corresponds to the most discriminative variable.

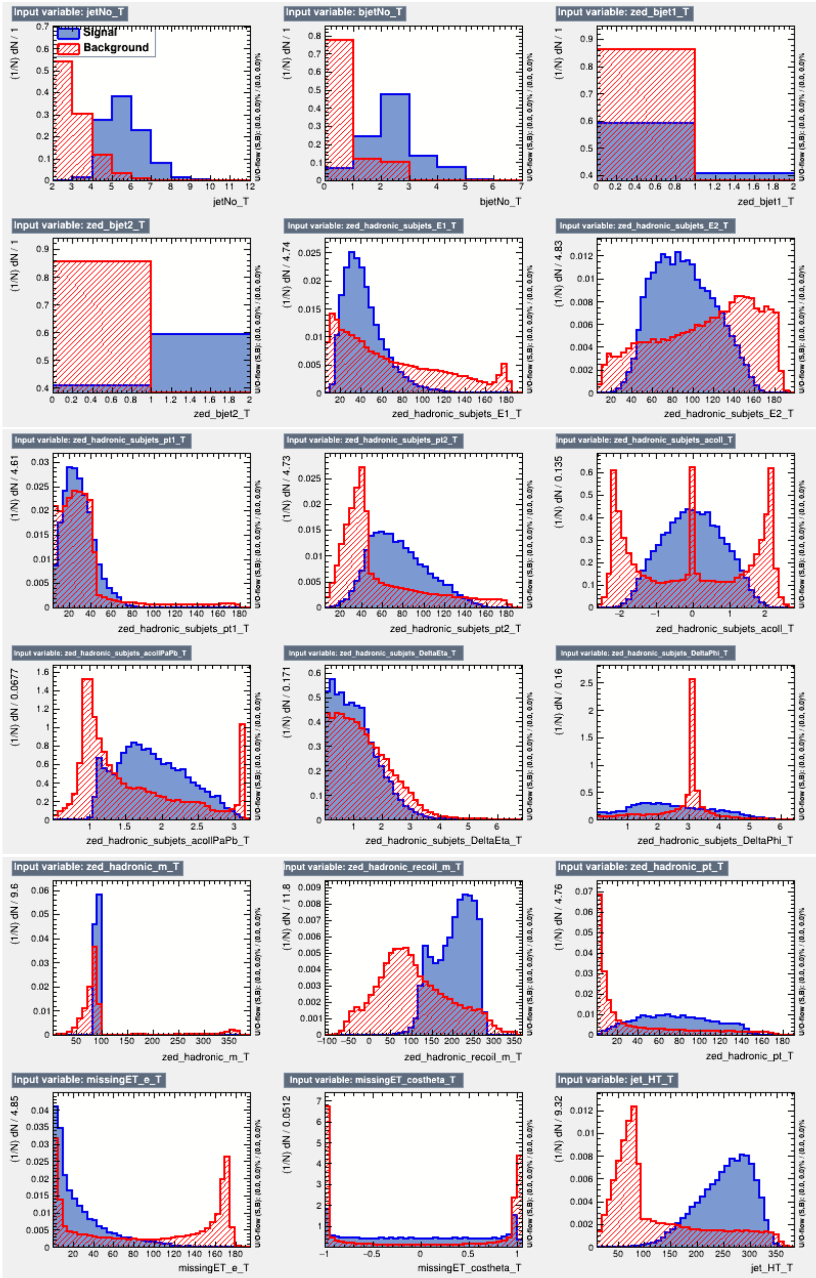

Figure 66: The input variable distributions for the $bjH$-BDT at 365 GeV.

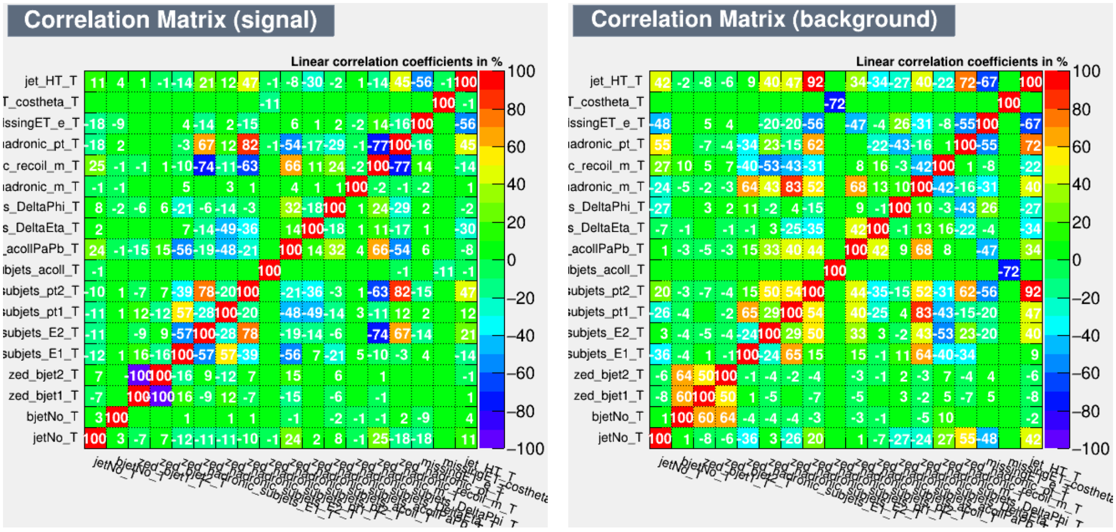


Figure 67: (a): Correlation matrix based on events from the signal sample. (b): Correlation matrix based on events from the background samples.

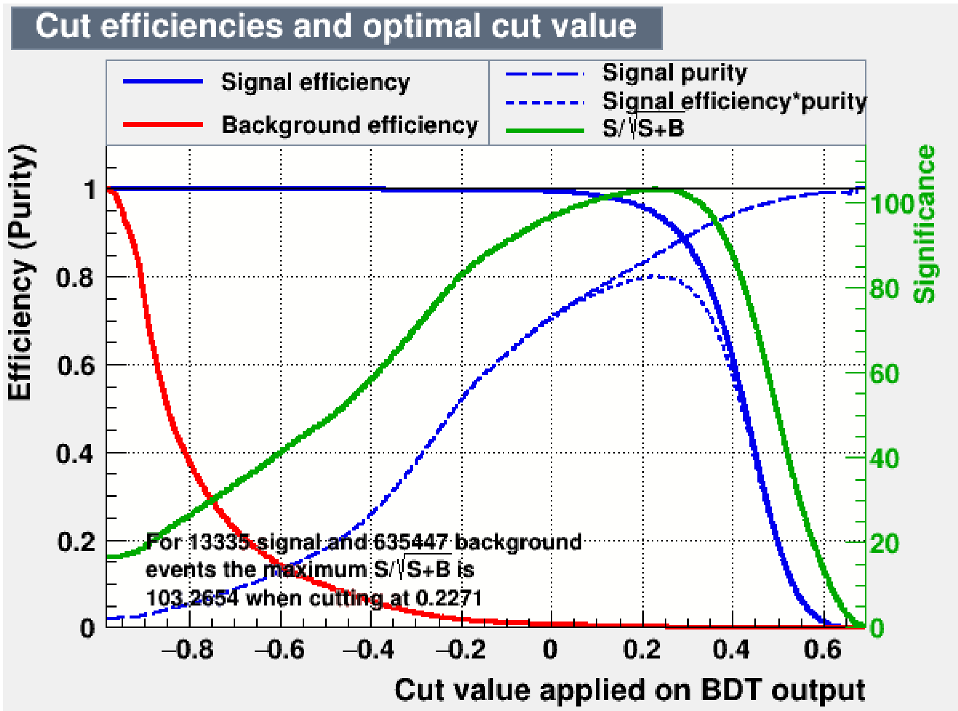


Figure 68: Significance as a function of the final BDT classifier. The significance function is based on 13’335 signal events and 635’447 background events.

### $e^+e^- \to Z(c\bar{c})H$

In total 17 input variables were used to train the BDT which are mostly related to the Z system. The most discriminative variable is the number of jets in the final state (see table 29). We used 5'000 signal events and 100'000 background events for training the BDT. To determine the cut on the final BDT classifier, we used the maximum of the significance distribution ($S/\sqrt{S+B}$, Fig. 71) which is calculated with 2'019 signal events and 356'293 background events in mind (number of events before applying any BDT cut).

| Rank | Variable | Rank | Variable |
|---|---|---|---|
| 1 | $N_{\text{jets}}$ | 10 | MET |
| 2 | $p_{T,cc}$ | 11 | $\cos(\theta_{\text{miss}})$ |
| 3 | $\text{H}_T$ | 12 | Acollinearity of Jets |
| 4 | $M_{\text{Rec}}$ | 13 | $E_{\text{c,2}}$ |
| 5 | $\Delta\phi(cc)$ | 14 | $E_{\text{c,1}}$ |
| 6 | $N_{\text{cjets}}$ | 15 | $p_{\text{T,j,1}}$ |
| 7 | $p_{\text{T,j,2}}$ | 16 | $N_{\text{bjets}}$ |
| 8 | $M_{cc}$ | 17 | $\Delta\eta(cc)$ |
| 9 | $\theta_{cc}$ | | |

Table 29: The ranking of the input variables according to their separation power. The highest ranked variable corresponds to the most discriminative variable.

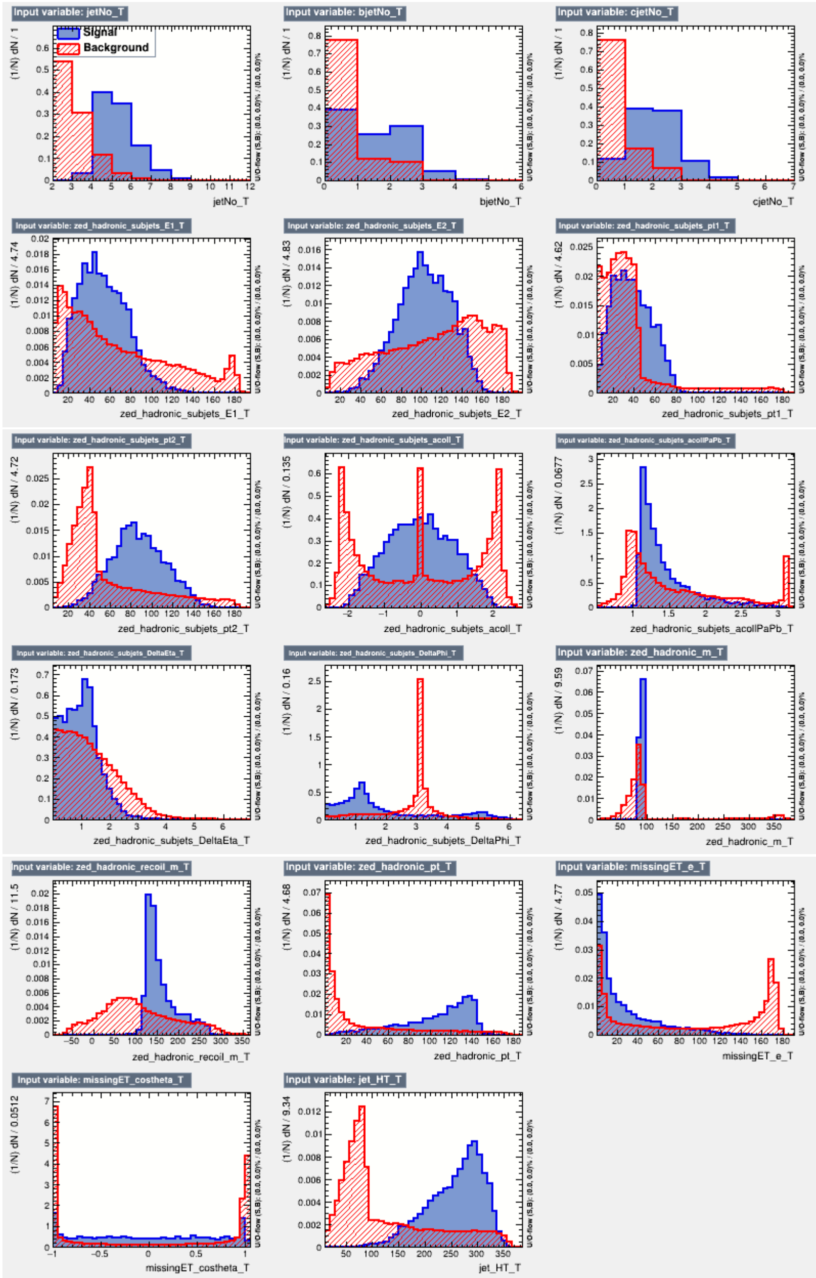

Figure 69: The input variable distributions for the $ccH$-BDT at 365 GeV.

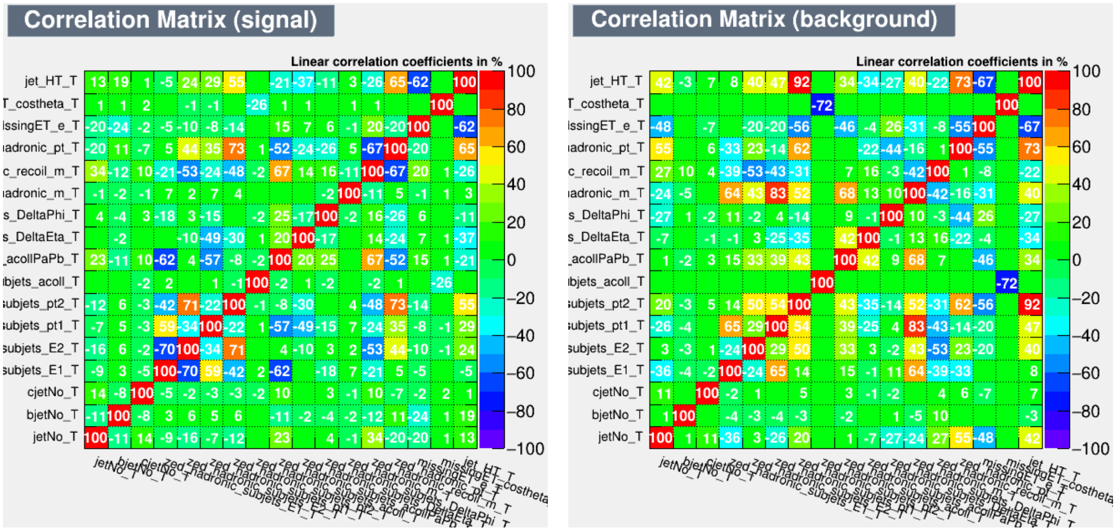


Figure 70: (a): Correlation matrix based on events from the signal sample. (b): Correlation matrix based on events from the background samples.

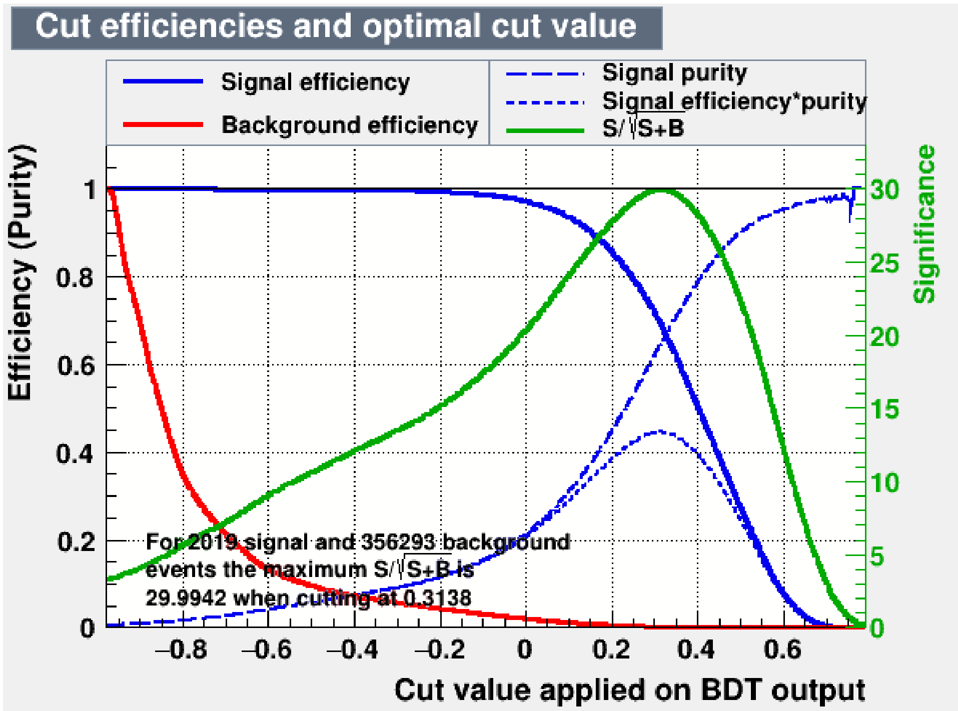


Figure 71: Significance as a function of the final BDT classifier. The significance function is based on 2'019 signal events and 356'293 background events.

$e^+e^- \to Z(c\bar{j})H$

In total 19 input variables were used to train the BDT which are mostly related to the Z system. The most discriminative variable is the number of jets in the final state (see table 30). We used 20'000 signal events and 100'000 background events for training the BDT. To determine the cut on the final BDT classifier, we used the maximum of the significance distribution ($S/\sqrt{S+B}$, Fig. 74) which is calculated with 6'570 signal events and 1'397'702 background events in mind (number of events before applying any BDT cut).

| Rank | Variable | Rank | Variable |
|---|---|---|---|
| 1 | $N_{\text{jets}}$ | 11 | $N_{\text{cjets}}$ |
| 2 | $\text{H}_T$ | 12 | Acollinearity of Jets |
| 3 | $p_{T,cj}$ | 13 | $E_{\text{j},2}$ |
| 4 | $M_{\text{Rec}}$ | 14 | $E_{\text{j},1}$ |
| 5 | $M_{cj}$ | 15 | $c$ Jet flag 2 |
| 6 | $p_{\text{T,j},2}$ | 16 | $c$ Jet flag 1 |
| 7 | $\theta_{cj}$ | 17 | $N_{\text{bjets}}$ |
| 8 | $\Delta\phi(cj)$ | 18 | $p_{\text{T,j},1}$ |
| 9 | MET | 19 | $\Delta\eta(cj)$ |
| 10 | $\cos(\theta_{\text{miss}})$ | | |

Table 30: The ranking of the input variables according to their separation power. The highest ranked variable corresponds to the most discriminative variable.

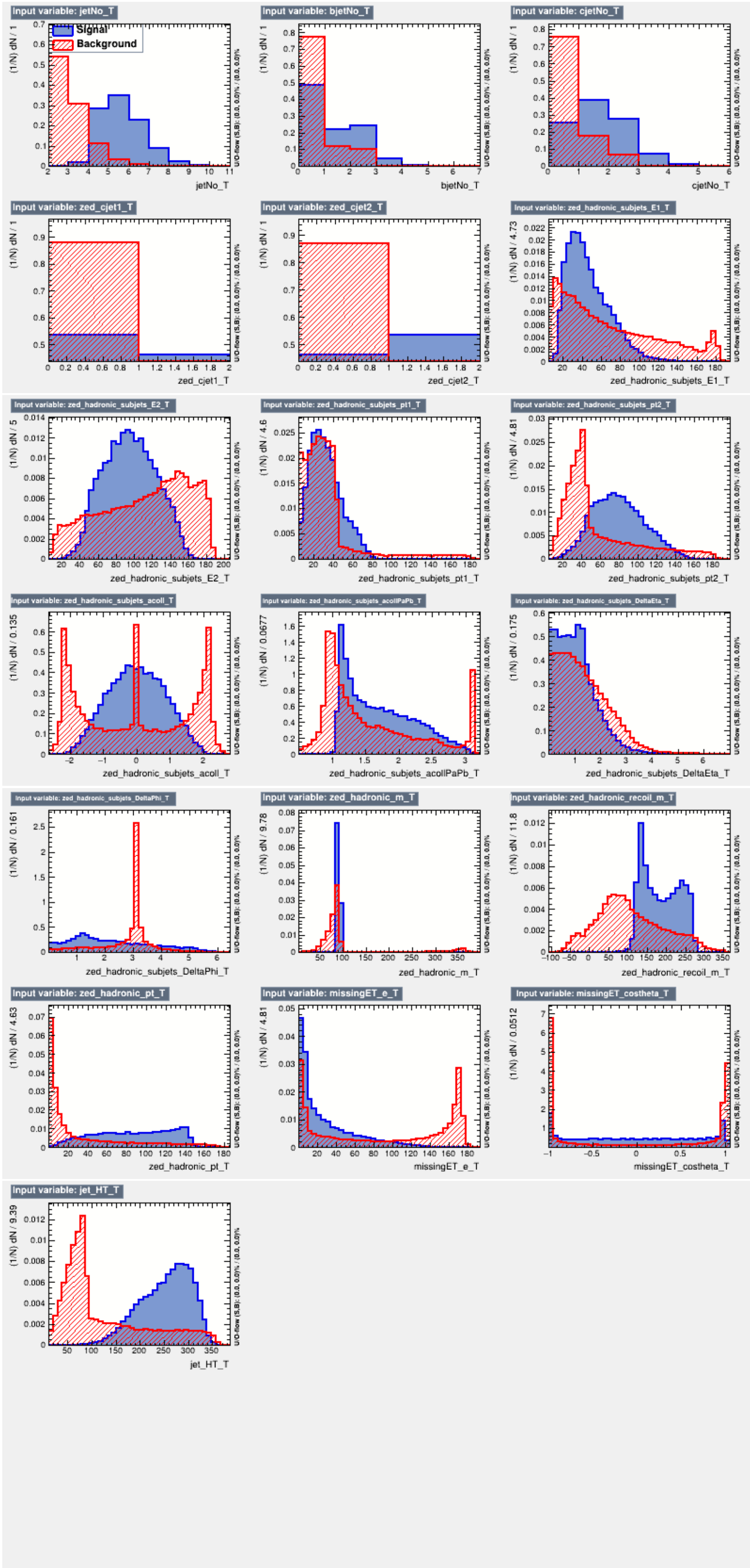


Figure 72: The input variable distributions for the $cjH$-BDT at 365 GeV.

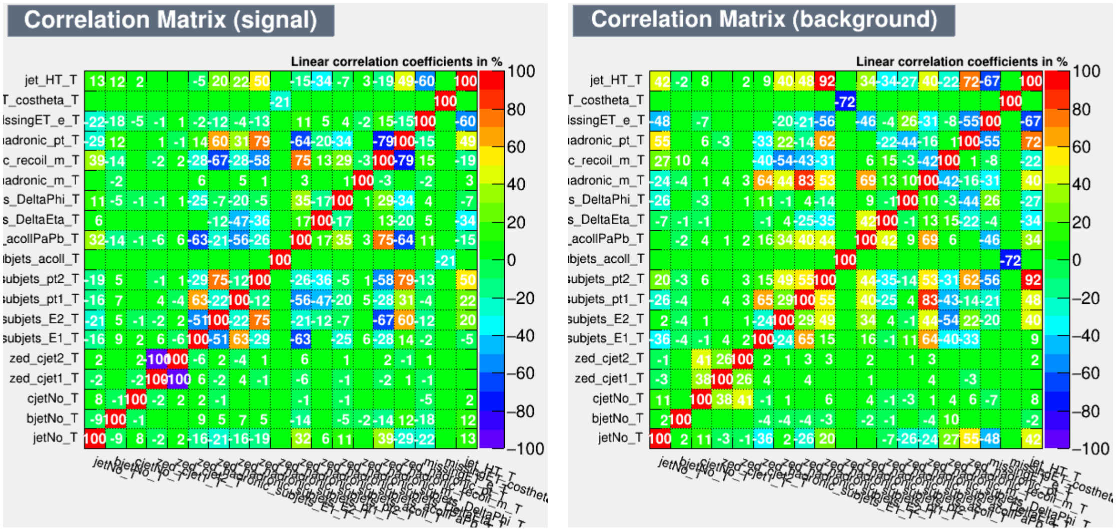


Figure 73: (a): Correlation matrix based on events from the signal sample. (b): Correlation matrix based on events from the background samples.

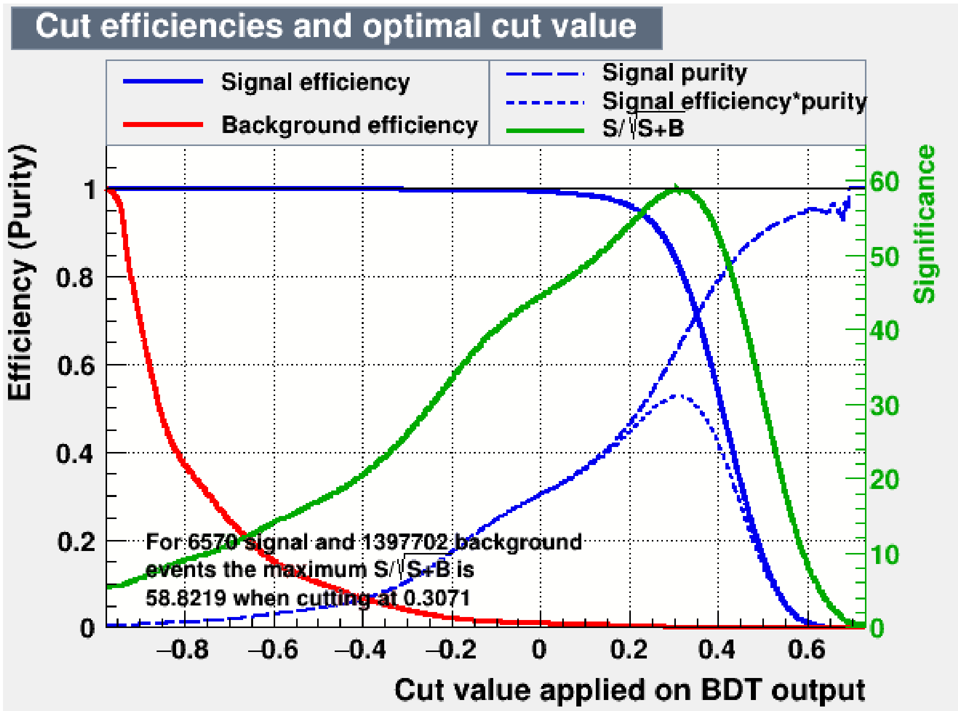


Figure 74: Significance as a function of the final BDT classifier. The significance function is based on 6'570 signal events and 1'397'702 background events.

### $e^+e^- \rightarrow Z(i\bar{j})H$

In total 19 input variables were used to train the BDT which are mostly related to the Z system. The most discriminative variable is the number of jets in the final state (see table 31). We used 20'000 signal events and 100'000 background events for training the BDT. To determine the cut on the final BDT classifier, we used the maximum of the significance distribution ($S/\sqrt{S+B}$, Fig. 77) which is calculated with 38'288 signal events and 8'138'805 background events in mind (number of events before applying any BDT cut).

| Rank | Variable | Rank | Variable |
|---|---|---|---|
| 1 | $N_{\text{jets}}$ | 11 | Acollinearity of Jets |
| 2 | $\text{H}_T$ | 12 | $E_{\text{j},2}$ |
| 3 | $p_{T,ij}$ | 13 | $E_{\text{j},1}$ |
| 4 | $M_{\text{Rec}}$ | 14 | $p_{\text{T,j},1}$ |
| 5 | $M_{ij}$ | 15 | $N_{\text{bjets}}$ |
| 6 | $p_{\text{T,j},2}$ | 16 | $b$ Jet flag 2 |
| 7 | $\Delta\phi(ij)$ | 17 | $b$ Jet flag 1 |
| 8 | $\theta_{ij}$ | 18 | $\Delta\eta(ij)$ |
| 9 | $\cos(\theta_{\text{miss}})$ | 19 | $N_{\text{cjets}}$ |
| 10 | MET | | |

Table 31: The ranking of the input variables according to their separation power. The highest ranked variable corresponds to the most discriminative variable.

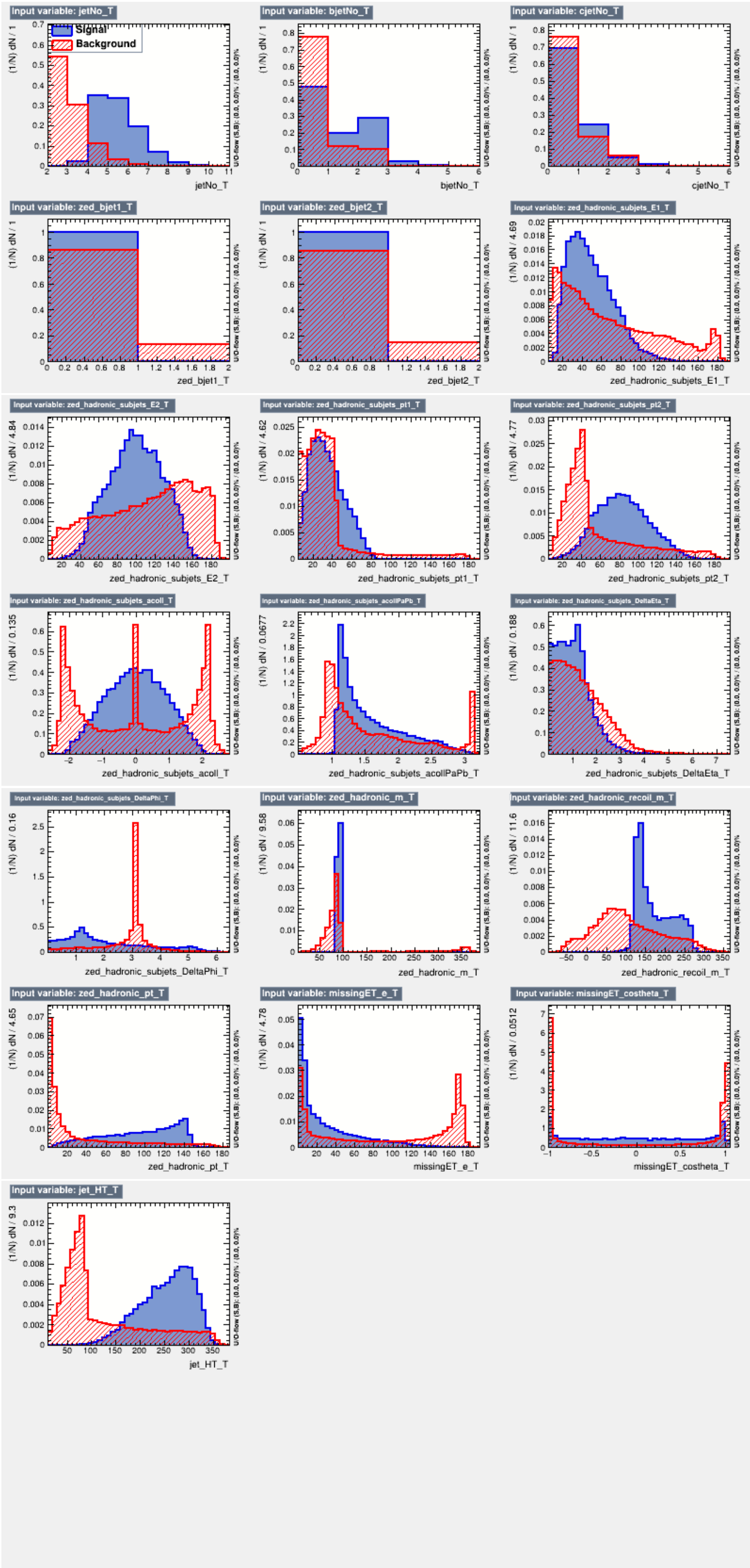

Figure 75: The input variable distributions for the $ijH$-BDT at 365 GeV.

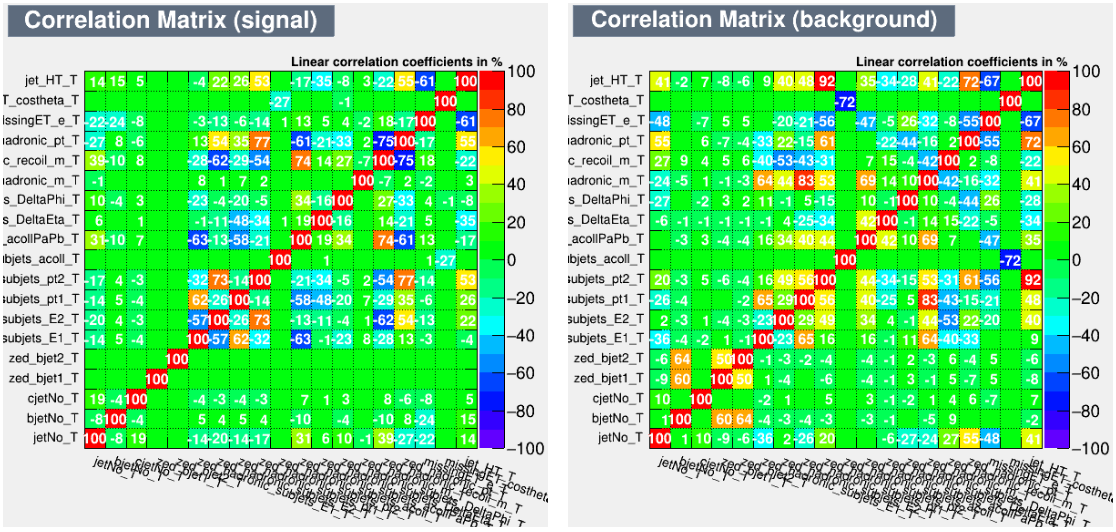


Figure 76: (a): Correlation matrix based on events from the signal sample. (b): Correlation matrix based on events from the background samples.

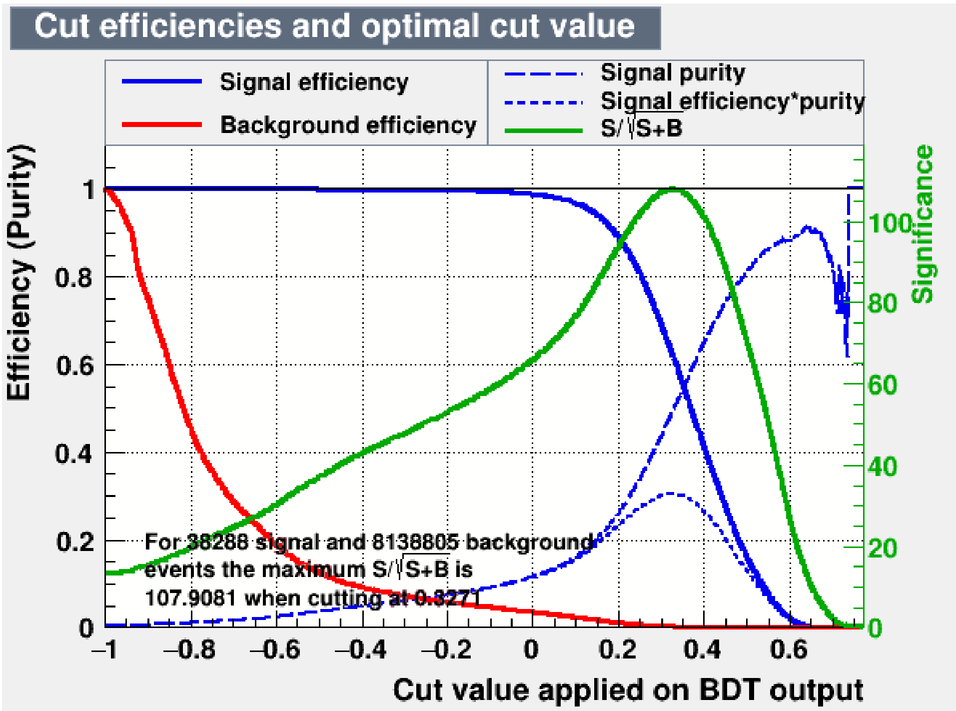


Figure 77: Significance as a function of the final BDT classifier. The significance function is based on 38’288 signal events and 8’138’805 background events.

### $e^+e^- \to \nu_e\bar{\nu}_e H(b\bar{b})$

In total 15 input variables were used to train the BDT which are mostly related to the H system. The most discriminative variable is the number of $b$-jets in the final state (see table 32). We used 7'500 signal events and 50'000 background events for training the BDT. To determine the cut on the final BDT classifier, we used the maximum of the significance distribution ($S/\sqrt{S+B}$, Fig. 80) which is calculated with 690 signal events and 1'028 background events in mind (number of events before applying any BDT cut).

| Rank | Variable | Rank | Variable |
|---|---|---|---|
| 1 | $N_{\text{bjets}}$ | 9 | $p_{T,bb}$ |
| 2 | $H_T$ | 10 | $p_{\text{T,b,2}}$ |
| 3 | $N_{\text{jets}}$ | 11 | $\cos(\theta_{\text{miss}})$ |
| 4 | MET | 12 | $E_{\text{b,1}}$ |
| 5 | $M_{\text{Rec}}$ | 13 | $\theta_{bb}$ |
| 6 | $E_{\text{b,2}}$ | 14 | $p_{\text{T,b,1}}$ |
| 7 | $M_{bb}$ | 15 | $\Delta\eta(bb)$ |
| 8 | Acollinearity of Jets | | |

Table 32: The ranking of the input variables according to their separation power. The highest ranked variable corresponds to the most discriminative variable.

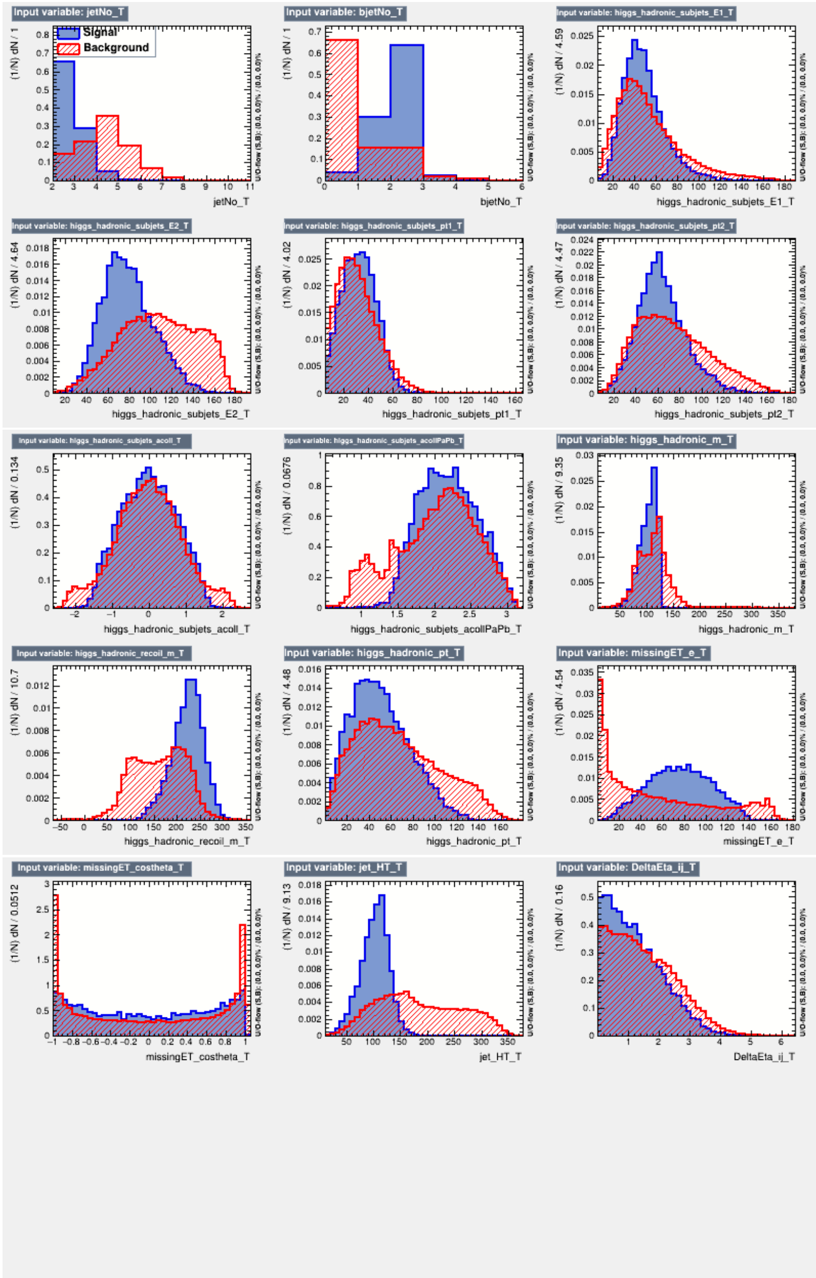


Figure 78: The input variable distributions for the $\nu\nu bb$-BDT at 365 GeV.

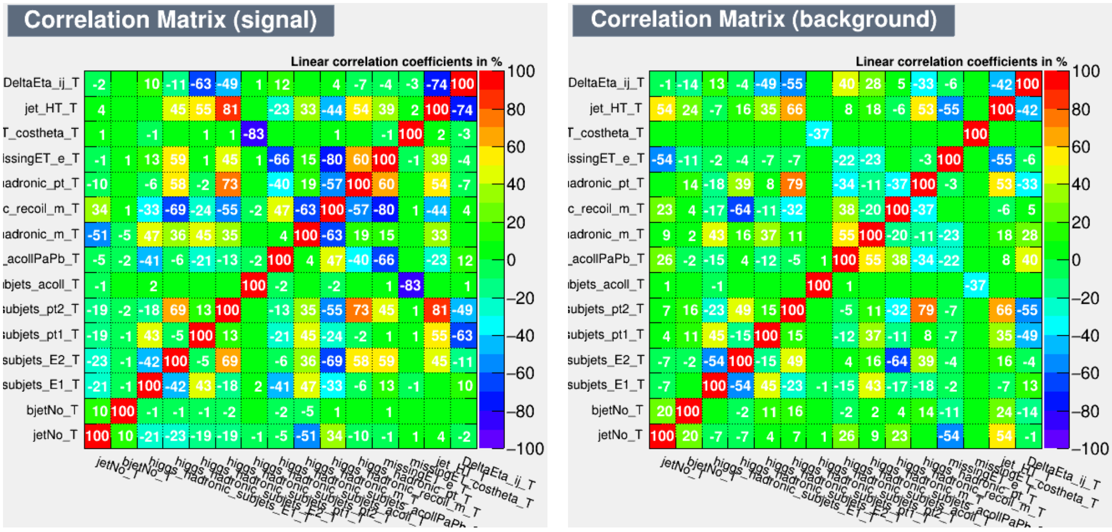


Figure 79: (a): Correlation matrix based on events from the signal sample. (b): Correlation matrix based on events from the background samples.

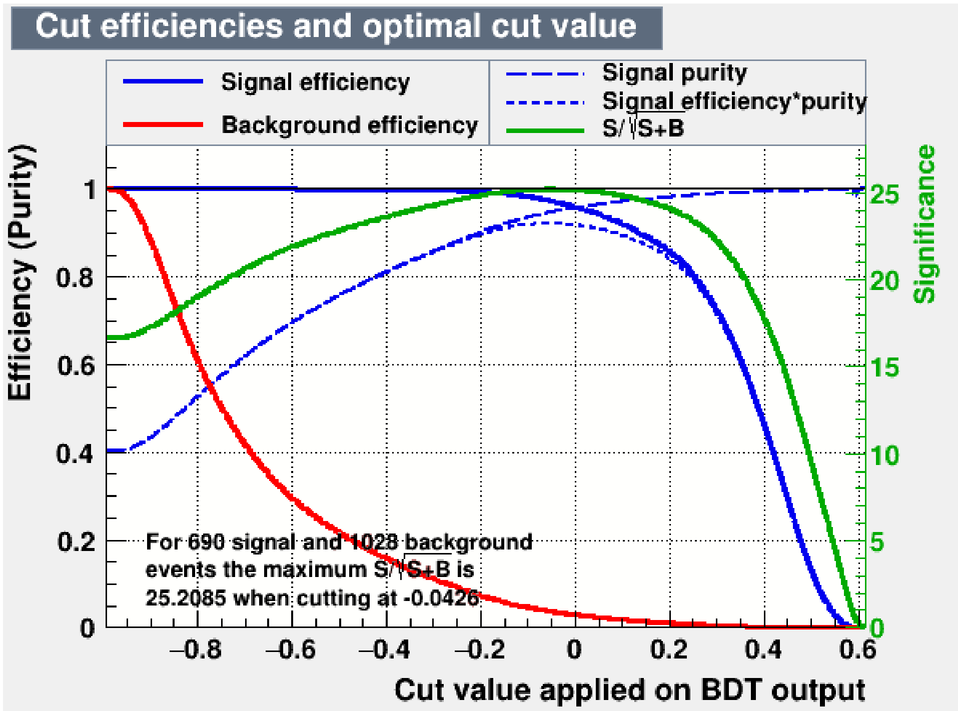


Figure 80: Significance as a function of the final BDT classifier. The significance function is based on 690 signal events and 1'028 background events.

$e^+e^- \to e^+e^- H(b\bar{b})$

In total 18 input variables were used to train the BDT which are mostly related to the H system. The most discriminative variable is the invariant mass of the electron system (see table 33). We used 5'000 signal events and 50'000 background events for training the BDT. To determine the cut on the final BDT classifier, we used the maximum of the significance distribution ($S/\sqrt{S+B}$, Fig. 82) which is calculated with 225 signal events and 177 background events in mind (number of events before applying any BDT cut).

| Rank | Variable | Rank | Variable |
|---|---|---|---|
| 1 | $M_{ee}$ | 10 | $p_{\mathrm{T,j,2}}$ |
| 2 | $N_{\mathrm{bjets}}$ | 11 | $p_{T,bb}$ |
| 3 | MET | 12 | $\theta_{bb}$ |
| 4 | $M_{bb}$ | 13 | $\eta_{b,2}$ |
| 5 | $N_{\mathrm{jets}}$ | 14 | $E_{\mathrm{b,1}}$ |
| 6 | $M_{\mathrm{Rec}}$ | 15 | $\cos(\theta_{\mathrm{miss}})$ |
| 7 | $H_T$ | 16 | $p_{\mathrm{T,j,1}}$ |
| 8 | $E_{\mathrm{b,2}}$ | 17 | $\Delta\eta(bb)$ |
| 9 | Acollinearity of Jets | 18 | $\eta_{b,1}$ |

Table 33: The ranking of the input variables according to their separation power. The highest ranked variable corresponds to the most discriminative variable.

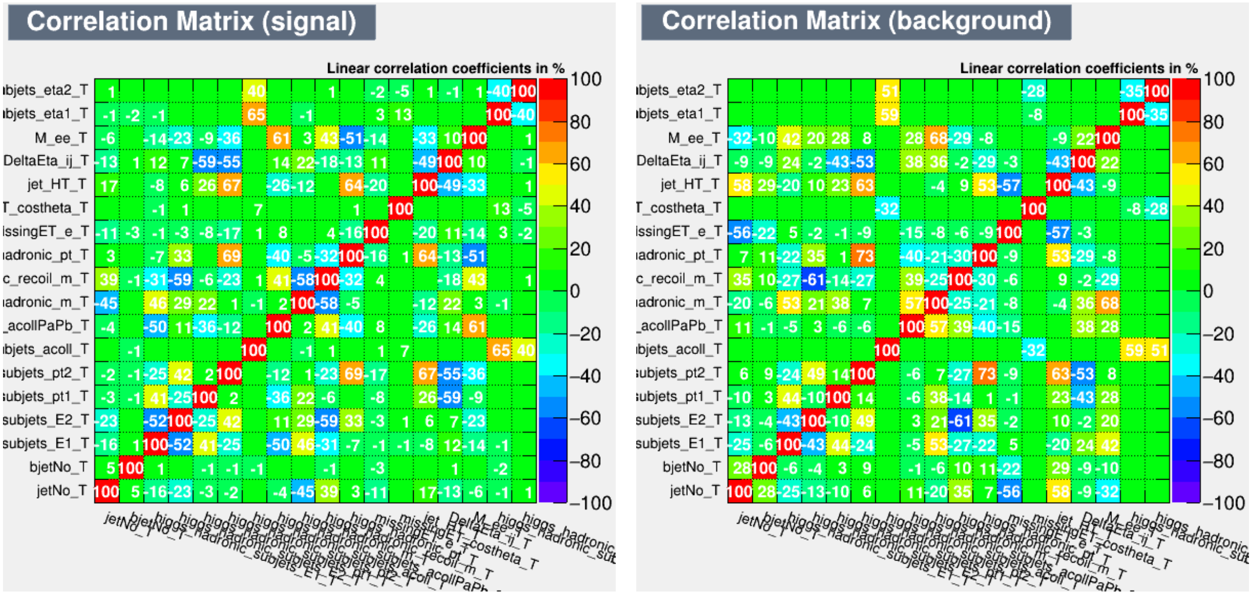


Figure 81: (a): Correlation matrix based on events from the signal sample. (b): Correlation matrix based on events from the background samples.

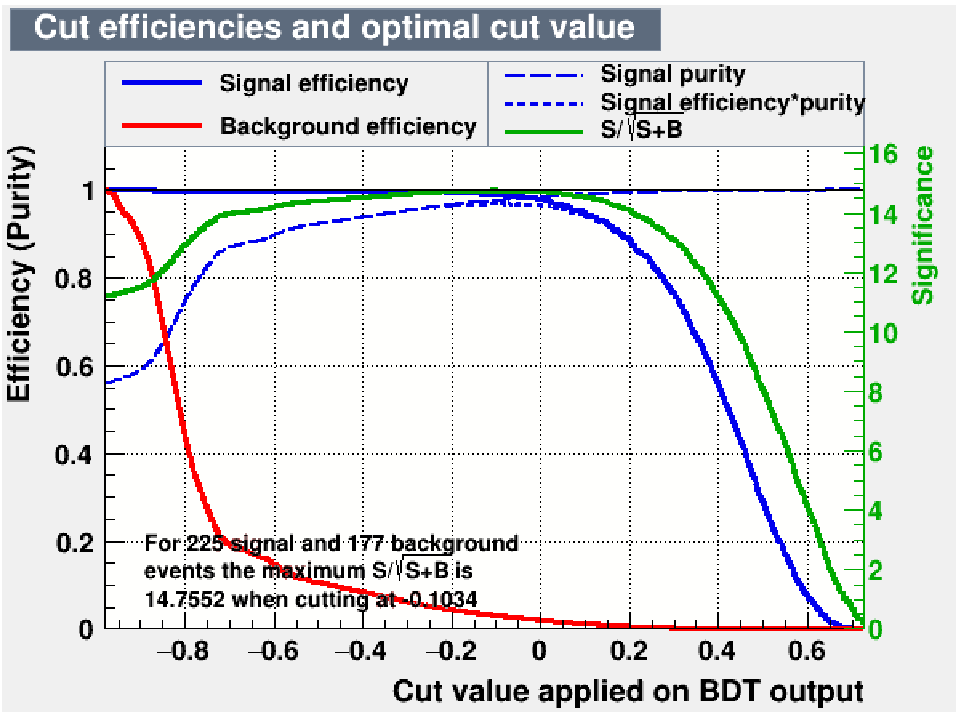


Figure 82: Significance as a function of the final BDT classifier. The significance function is based on 225 signal events and 177 background events.

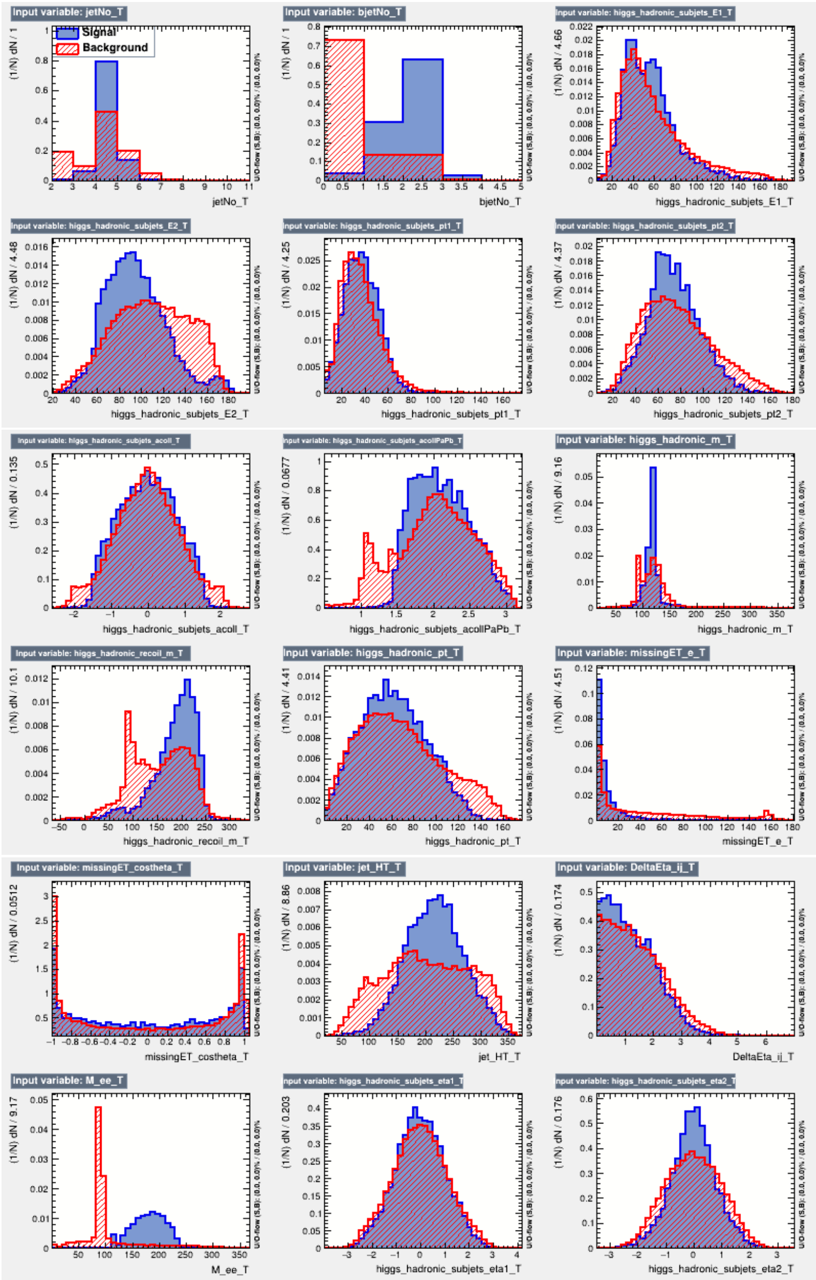

Figure 83: The input variable distributions for the $eebb$-BDT at 365 GeV.

# G Inclusive VBF

## Neutral VBF

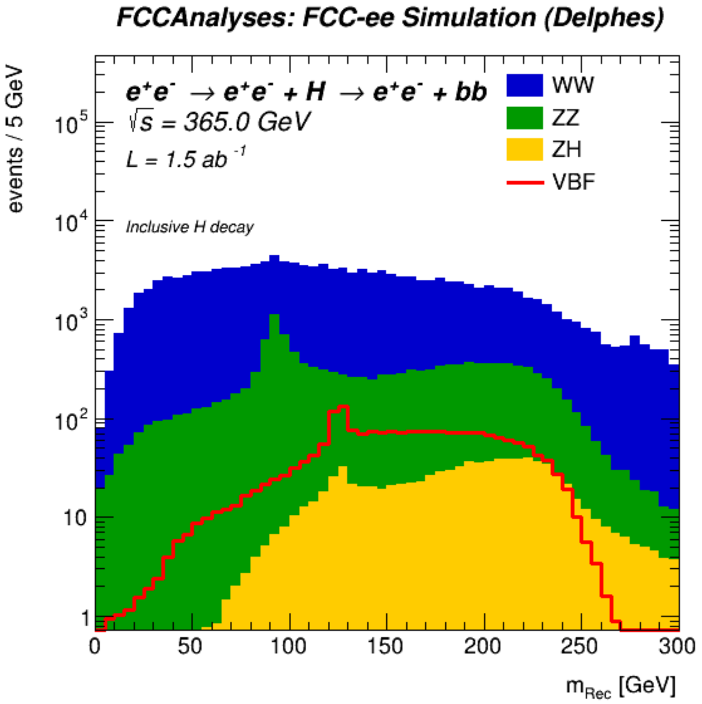


(a)

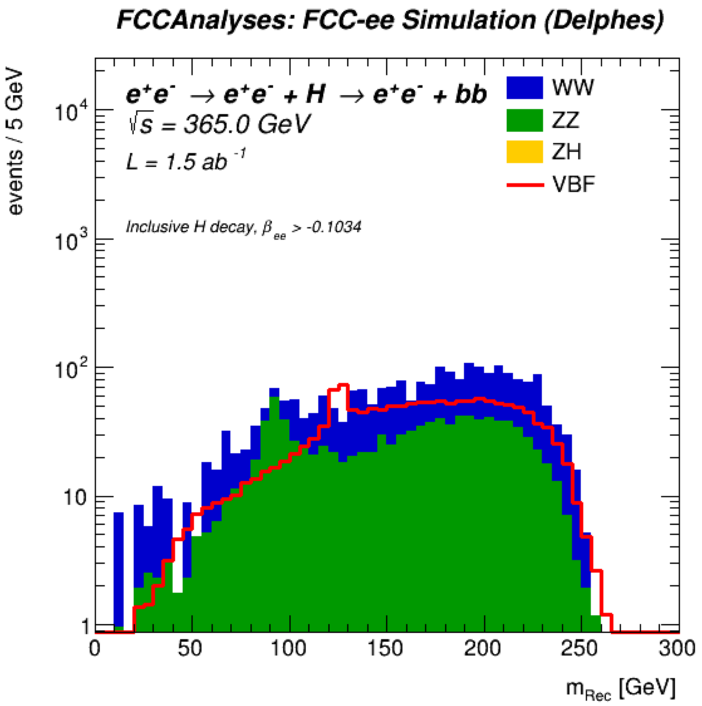


(b)

Figure 84: (a): Mass of the Higgs system in neutral VBF with an inclusive Higgs decay. The background through vector boson production is very pronounced. (b): The same mass distribution after the application of a BDT cut.

## Charged VBF

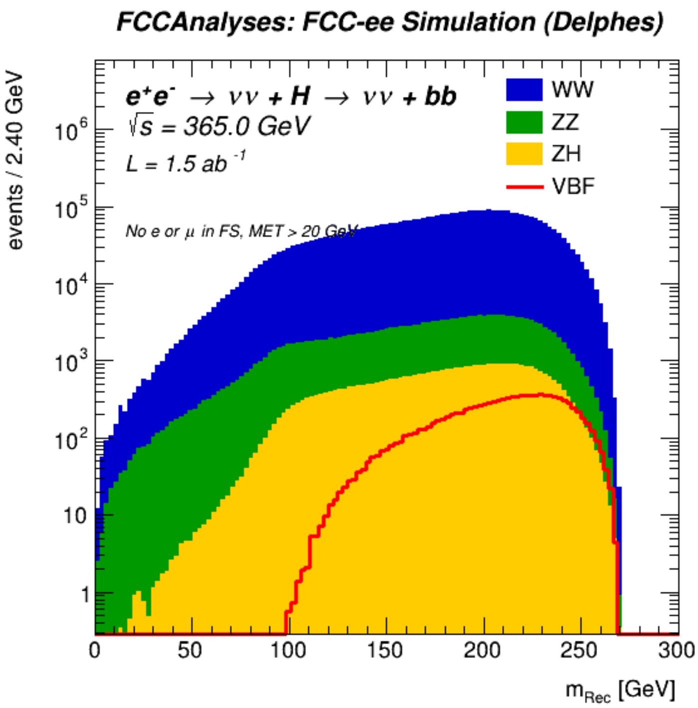


(a)

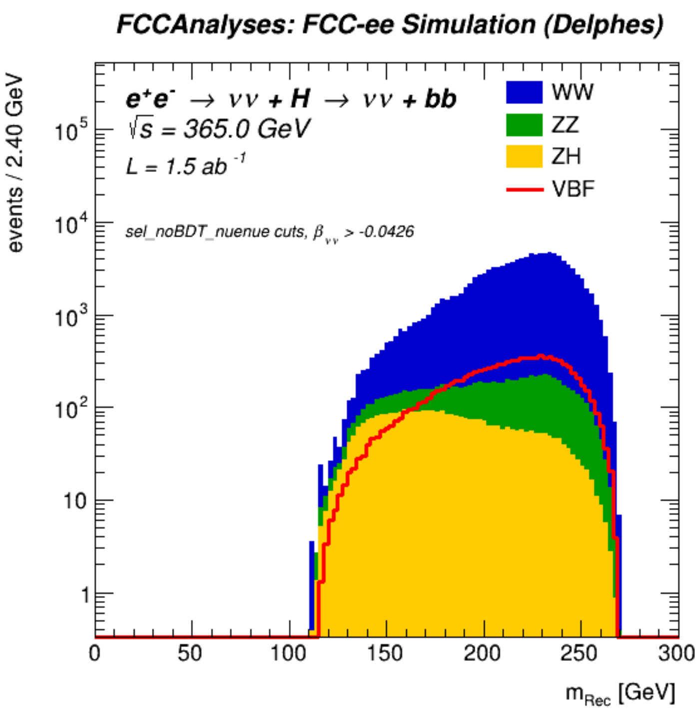


(b)

Figure 85: (a): Mass of the Higgs system in charged VBF with an inclusive Higgs decay. The background through vector boson production is very pronounced. (b): The same mass distribution after the application of a BDT cut.